The Dissertation Committee for James Kevin Mikulak certifies that this is the approved version of the following dissertation

Size effects in out-of-plane bending in elastic honeycombs fabricated using additive manufacturing: modeling and experimental results

Committee:

Desiderio Kovar, Supervisor

Eric M Taleff

Gregory J Rodin

David L Bourell

Michael R Haberman

Size effects in out-of-plane bending in elastic honeycombs fabricated using additive manufacturing: modeling and experimental results

By

James Kevin Mikulak, B.S.M.E., M.S.E.

Dissertation

Presented to the Faculty of the Graduate School of

The University of Texas at Austin

in Partial Fulfillment

of the Requirements

for the Degree of

Doctor of Philosophy

The University of Texas at Austin

December, 2011

Dedication

I dedicate this work to the remembrance of my mother, Betty and my brother, Gregg, both of whom are greatly missed. To my father, James, my son, Eric and all the Mikulak's in Georgia, where ever they may be. To my friend Carl Deckard.. And lastly and lovingly I dedicate this work to my partner, my friend and my wife, Holly Ahern.

Acknowledgements

I would like to thank the following people for their help with this work.

Dr. Bourell and Mark Phillips for their great support in LFF Lab.

Dr. Rodin for his assistance in modeling

Dr. Taleff for his testing insight

Dr. Haberman for his interest in this problem

I especially want to acknowledge my supervisor, Dr. Kovar, who over the years has consistently, professionally and with the best humor provided me with sound guidance and timely support in this effort.

Abstract

Size effects in out-of-plane bending in elastic honeycombs fabricated using additive manufacturing: modeling and experimental results

James Kevin Mikulak, Ph.D.

The University of Texas at Austin, 2011

Supervisor: Desiderio Kovar

Size effects in out-of-plane bending stiffness of honeycomb cellular materials were studied using analytical mechanics of solids modeling, fabrication of samples and mechanical testing. Analysis predicts a positive size-effect relative to continuum model predictions in the flexure stiffness of a honeycombed beam loaded in out-of-plane bending. A method of determining the magnitude of that effect for several different methods of constructing or assembling square-celled and hexagonal-celled materials, using both single-walled and doubled-walled construction methods is presented. Hexagonal and square-celled honeycombs, with varying volume fractions were fabricated in Nylon 12 using Selective Laser Sintering. The samples were mechanically tested in three-point and four point-bending to measure flexure stiffness. The results from standard three-point flexure tests, did not agree with predictions based on a mechanics of solids model for either square or hexagonal-celled samples. Results for four-point bending agreed with the mechanics of solids model for the square-celled geometries but not for the hexagonal-celled geometries. A closed form solution of an elasticity model for the response of the four-point bending configuration was developed, which allows interpretation of recorded displacement data at two points and allows separation the elastic bending from the localized, elastic/plastic deformation that occurs between the loading rollers and the specimen's surface. This localized deformation was significant in the materials tested. With this analysis, the four-point bending data agreed well with the mechanics of solids predictions.

Contents

List of Tables

List of Figures

Chapter 1: Introduction and motivation for research

Introduction

One definition of cellular solids is “an assembly of cells with solid edges or faces packed together to fill space” (Gibson and Ashby 1997). Many examples of cellular solids exist in nature; cork, sponges, and coral are examples of three-dimensional cellular materials, while a beehive is an example of honeycomb cellular material. Man-made cellular materials have been produced from many materials including metals, ceramics, plastics and even composites. Interesting applications of manufactured cellular structures include lightweight space and aerospace construction materials (Labuhn 2005) (Bianchi, Aglietti and Richardson 2010), materials for impact absorption (Banhart 2001) and materials used to provide reaction sites for catalysis (Gruppi and Tronconi 2005).

A defining feature of cellular solids is that they exhibit a high stiffness-to-mass ratio. Conventional theory predicts that this ratio depends on the properties of the solid material used, the volume fraction of solid, and the shape of the cells (Gibson and Ashby 1997). Nature to date has succeeded in constructing cellular materials with far more complex architectures than human-kind; to paraphrase Sir Michael Ashby, nature builds with cells while man builds with solids (Simancik 2002). The point is that, until recently, the ability to tailor the architectural parameters that define a cellular solid such as cell size, cell geometry and volume fraction has been limited by existing materials processing technologies. So unlike what we see in nature, the majority of existing cellular solids and even appropriate tools to analyze the behavior of cellular solids have been limited to materials that have uniform cell size, cell geometries, and relative densities.

The first effective honeycomb manufacturing technique was developed by Heilburn in 1901. As early as 1915, honeycomb cores were patented for aircraft applications. (EconHP Holding GmbH 2011) In these applications, honeycombs are very often used in a core and sandwich arrangement in which the cellular material has walls parallel with the thickness direction and is sandwiched between solid sheets of material. Typically in these configurations, honeycombs have a relatively short thickness compared to the width or length of the sandwich panel. These configurations have been well studied and are generally treated as continuum materials because the number of cells relative to the specimen size is large. In this work, we take a different approach by examining configurations with long z-axis lengths.

Recent advances in additive layered manufacturing (Marcus and Bourell 1993) and other new materials processing routes (Crumm and Halloran 1998) (Van Hoy, et al. 1998) have greatly enhanced the ability to tailor the defining parameters of cellular materials. When building cellular materials with 3D CAD-driven, additive manufacturing processes, the use of multi-scale cells, varying wall thickness, mixed geometries or non-uniform relative densities is as easy as the use of uniform size, geometry, and density.

These parameters can now be varied so that cell topology and scale effects can now be reasonably considered. However, to date there has been no design guidance available to leverage these processing capabilities to build non-uniform cellular materials with properties that are superior to uniform cellular materials.

Of interest in determining the influence of cellular architectures on stiffness is the issue of a size effect that occurs when there is a small specimen-to-cell size ratio. This effect has been known alternatively as an edge effect and its recognition, as an effect seen in honeycombs or foam materials, traces back to attempts to make accurate measurements of Young's modulus of cellular ceramic foams (Brezny and Green 1990) (Anderson and Lakes 1994). Measurements made on small samples "simply didn't make sense" and in practical terms few attempts were made to measure and characterize properties below a certain specimen-to-cell size ratio.

Size effects are known in to exist in the plastic deformation of dense metals. Indentations, conducted by L.M. Brown and reported by N.A. Fleck, showed the inferred hardness of a sample increases with a decreasing indent size for indents in the micron to submicron range (Fleck and Hutchinson 1993). Fleck also reported copper wires in the 12-170 μm diameter range showed the thinner wires exhibiting stronger behavior than the thicker wires in torsion testing. M.I. Idiart reports the effect in micro-bending of thin metallic foils in the 10-150 μm range (Idiart, et al. 2009). Mechanistically this behavior has been explained as strain hardening resulting from the accumulation of statistically stored or geometrically necessary dislocations while from a phenomenological standpoint, conventional continuum theories of plasticity, like those of elasticity possess no material length scale. In the case of plasticity, the generalized continuum theory, has been expanded to account for this size effect (Fleck, et al. 1994) (Fleck and Hutchinson 1997). These modifications of the generalized continuum theory are higher order theories such as strain gradient theories.

In general size effects are considered significant when two characteristic lengths in a material are of the same order. For example, the characteristic length scale in dense metals is of the order of 1 μm while the length scales for commercially available honeycombs can be closer to 1 mm. Assuming typical specimen or feature dimensions are 1 mm and above, then honeycombs are far more likely to experience overlap of the macro-scale specimen or feature lengths with the micro-scale characteristic lengths.

Experiments have demonstrated that in some loading configurations these size effects cannot be ignored when characterizing the elastic response of cellular solids or foam (Lakes 1983) (Andrews, Gioux, et al. 2001) (Anderson and Lakes 1994) (Brezny and Green 1990). Greatly varying, both positive and negative size effects have been documented in different loading conditions such as uniaxial compression, torsion, indentation, bending and around notches and holes. (Andrews & Gibson, 2001) (Mora and Waas 2000) Like in the case of plasticity of dense metals, the elastic continuum analysis of cellular materials as developed by Gibson and Ashby does not include a length scale and does not account for any size effect (Gibson and Ashby 1997).

The possible loading configurations, together with the geometries of cellular solids, honeycombs or foams, their volume fractions, their cell shapes, and whether loading is in-plane or out-of-plane creates a large space to examine. Some reduction in the number of possible configurations is possible by recognizing that foams and cellular honeycomb structures can act as models for each other in some configurations that lend themselves to two dimensional analyses. Foams loaded in compression and honeycombs loaded in in-plane compression are examples. However, other configurations require more complicated two and a half dimensional or three dimensional analyses. **Our interest is in honeycomb-type cellular solids with a focus on out-of-plane bending which requires higher order analyses.**

BACKGROUND AND PREVIOUS WORK

Both analytical and discrete two dimensional models have been proposed (Onck, Andrews and Gibson 2001) (Tekoglu & Onck, 2005) (Dai and Zhang 2009) (Tekoglu & Onck, 2008) to characterize the elastic behavior of honeycombs. These models have been compared to a small set of experiments, most of which were performed on foams. Onck et al. developed an analysis for infinitely long, regular hexagonal honeycombs loaded 1) in-plane uniaxially in compression and 2) in shear (Onck, Andrews and Gibson 2001). They used a combination of analytical analysis and 2D finite element modeling using a commercial FEM code. Their model used a combination of conventional beam bending analysis, rigid body assumptions, and equations of compatibility of deformation to predict an elastic size effect in uniaxial compression and shear. They used their model to predict enhanced compliance in compression and enhanced stiffness relative to the predictions of the continuum model of Gibson and Ashby for cellular materials loaded in shear. Thus, the size effect can be either positive or negative, but the predicted shear stiffening was short lived, being observed only for very small values of specimen-to-cell size ratio. It was also shown that the location of specimen edge relative to the cellular architecture was important. For example, specimens can terminate at a closed cell or an open cell. The weakening effect seen in compression was attributed to decreased constraint from open cells and for cells located near a free surface. The mechanism for the shear stiffening was not explicitly addressed.

Experimental work was done in conjunction with the previously described modeling (Andrews & Gibson, 2001). A seven volume percent, 20 pore per inch, open-cell Al 6101-T6 (trade name Duocel) foam and 8% dense, closed-cell Al foam (trade name Alpora) were tested in compression and in shear at different size ratios of specimen-to-cell size. Their results showed qualitative agreement with the trends in the modeling, but with quantitative differences.

Tekoglu et al. considered extensions to the generalized continuum theories to determine a theory that could best match the results of discrete models (Tekoglu & Onck, 2008). They addressed both higher-order theories, such as micropolar theory, micromorphic theory and microstrech theory and higher-grade theories, such as strain gradient theory, stress couple theory and a variation of the stress couple theory that they call strain divergence theory. Both the higher-order and higher-grade theories require an introduction of additional degrees of freedom into the continuum. The higher order theories do this by introducing a new independent degree of freedom. In the case of micropolar theory, a rotational degree of freedom is introduced. The higher grade theories introduce the new degrees of freedom by tying the deformation measures to additional gradients in the strain. Tekoglu evaluated two potential extensions of generalized continuum theory, the micropolar rotation and strain divergence theory, against numerical modeling. For shear, the two theories converged, i.e. the fit characteristic length was of the same order as the cell size, and they reported excellent agreement in strain fields. However for pure bending, this was not the case, i.e. the analytical solution using micro-polar and strain divergence theories both predicted an increase in stiffness while the discrete analysis predicted a reduction in stiffness.

Dai and Zhang (Dai and Zhang 2009) modeled the elastic behavior of cellular materials using an analytical bending energy method for in-plane bending of four types cellular structures built with different unit cells including rectangular, hexagonal, triangular and Kagome structures, and compared those results to the predictions of two continuum calculations. The two continuum models included a general homogenization method and what the authors described as a meso-mechanics method that was based on Gibson and Ashby's work. Neither continuum method predicted a size effect while their bending energy method did. They reported different responses for the differing cell shapes. The rectangular cells showed an increase in stiffness, while the triangular and kagome cells showed a decrease in stiffness, and the hexagonal cells at low specimen-to-cell size ratios first exhibited a decrease in stiffness then an increase in stiffness before converging with the continuum predictions.

The motivation for this research is to understand of how cell architectural features; specimen-to-cell size ratio, geometry, and volume fraction influence the final stiffness of honeycomb cellular materials loaded in out-of-plane bending. To this end, we have conducted preliminary experiments by fabricating using selective laser sintering, differing sets of honeycomb structures. These honeycombs contain a solid fraction of between 15 and 45 percent, have uniform cell sizes, and have varying shapes and specimen-to-cell size ratios. We then experimentally measured the out-of-plane bending stiffness with the aim of documenting a size effect and determining what models can be used to correctly predict the effect. Ultimately, this information can be used to design and test materials with non-uniform architectures which may out-perform their more conventional counterparts.

Chapter 2: Modeling size effects of honeycombs loaded elastically in tension and bending

MOTIVATION AND SCOPE

From a practical standpoint, the design of honeycomb and foam structures has been limited by available manufacturing routes. When producing honeycomb structures from ceramics, plastics and metals, there are only a limited number of processing routes that exist for each material class. Several recent advances in manufacturing techniques such as additive manufacturing and micro-fabrication by co-extrusion have opened up new and as of yet unexplored methods for creating honeycomb structures with more complex architectures (Marcus and Bourell 1993). These methods allow much greater customization of the defining parameters of a honeycomb than the current methods that include expansion, corrugation, molding or direct extrusion (Banhart 2001) (Wadley 2003).

We start by looking at the parameters that define a honeycomb. Cell size, cell shape, and volume fraction or wall thickness are typically used to define the honeycomb architecture. For most commercially available honeycombs, these parameters are usually constant throughout the specimen. That is, the cell size, shape, wall thickness and thus volume fraction all remain the same throughout the structure, mainly because the manufacturing or processing route makes these parameters difficult or expensive to vary. However newer processing routes do not have these limitations. 3D additive manufacture methods such as selective laser sintering, (Marcus and Bourell 1993) (Deckard 1986) 3D printing (Rosochowski 2000) and fused deposition modeling (Crump 1989) allow the fabrication of structures with varying cell shapes, sizes and volume fractions without a differential production cost.

The combination of manufacturing and measurement constraints has resulted in limitation of the analysis of the elastic properties of honeycombs to configurations that have large specimen-to-cell size ratios. Expanding the use of honeycomb structures beyond the current architectures with uniform cell sizes to use them more effectively leads to designs with a longer z-axis length. This increases the exposure of these types of structures to bending as a limiting loading condition.

As discussed in the preceding chapter, one well established starting point for predicting the elastic response of cellular structures is the work of Gibson and Ashby (Gibson and Ashby 1997). These models are continuum analyses that do not include a length scale in the effective modulus. Instead, the out-of-plane elastic modulus E_3 is predicted to depend only on 1) the relative density of the honeycomb, ρ^*/ρ_s and 2) the Young's modulus of the solid portion of the honeycomb.

As part of this work, we will compare the effective stiffness predicted from Gibson and Ashby's continuum model with the predictions of effective stiffness made using a conventional mechanics of solids technique. To do this we consider multiple sets of sample structures chosen to highlight these effects. The goals of this part of our work are to 1) determine the magnitude of the size effect for specimens with small specimen-to-cell size ratios 2) determine the necessary specimen-to-cell size ratio where a continuum model can be used to predict effective stiffness, 3) examine the influence of relative density on the size effect and 4) examine the effects of cell geometry by varying the cell shape and configuration choices such a single verses double-walled structures.

CALCULATIONS

TENSION

We begin by employing a mechanics of solids analysis and considering honeycombs with small specimen-to-cell size ratios loaded in tension or compression and comparing these materials to a solid material, as shown in Figure 2-1. The top part of Figure 2-1 shows a side view and cross section of a solid. The bottom part of the figure shows the side view and cross section of a square–celled honeycomb consisting of a single cell. The single celled honeycomb is considered here because, if there is a size effect, it is expected that this architecture would show the largest effect. Both beams have the same perimeter and are loaded by an axial force *F*. They have areas *A* and *As*, respectively. We also define the Young's modulus of the solid specimen, *E*, and the effective Young's modulus of the single-celled square honeycomb, *Es*.

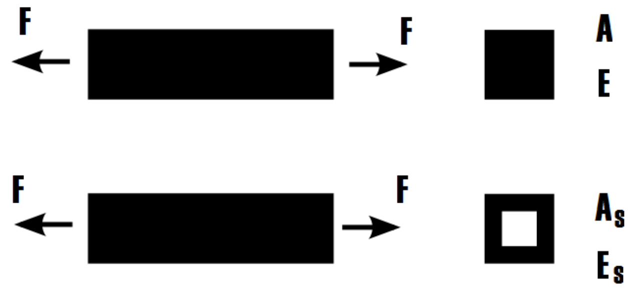

FIGURE 2-1: SINGLE CELL SQUARE HONEYCOMB AND SOLID ROD IN TENSION

The stress on each of these beams is

$$\sigma = \frac{F}{A} \qquad \text{Equation 2.1}$$

$$\sigma_S = \frac{F}{A_S} \qquad \text{Equation 2.2}$$

and assuming linear elasticity

$$\varepsilon = \frac{F}{AE} \qquad \text{Equation 2.3}$$

$$\varepsilon_S = \frac{F}{A_S E_S} \qquad \text{Equation 2.4}$$

Since the areas of the cross sections are the same

$$A_S = \phi A \qquad \text{Equation 2.5}$$

Where, ϕ is the volume fraction of solid in the honeycomb. Comparing the stresses and the strains and we obtain

$$\frac{\sigma}{\sigma_S} = \frac{A_S}{A} = \phi \qquad \text{Equation 2.6}$$

$$\frac{\varepsilon}{\varepsilon_S} = \frac{A_S E_S}{AE} = \frac{\phi A E_S}{AE} = \frac{\phi E_S}{E} \qquad \text{Equation 2.7}$$

Thus, for the axial strains in each specimen to be the same under a load *F*,

$$E = \phi E_s \quad \text{Equation 2.8}$$

and substituting Equation 2.7 into Equation 2.8, we obtain

$$\frac{\varepsilon}{\varepsilon_s} = \frac{\phi E_s}{\phi E_s} = 1 \quad \text{Equation 2.9}$$

This calculation shows that we do not expect to observe a size effect in tension or compression. Thus, we expect that the continuum analysis of Gibson and Ashby should be capable of predicting the elastic response of honeycombs loaded axially in tension and compression, independent of their specimen size-to-cell size ratios.

BENDING

To compare the predictions of the Gibson and Ashby continuum model to those obtained from a mechanics of solids analysis, a method for normalizing the stiffness is required. Recognizing that several normalization schemes are possible and that no one normalization method is intrinsically superior to another, the following method of normalizing bending stiffness and comparing the two methods was selected.

The flexure rigidity is defined as

$$E_s I \quad \text{Equation 2.10}$$

where E_s is a material property and I is the structure-dependent second moment of inertia. A continuum mechanics equivalent of the same flexure rigidity would be

$$E^* I_A = \frac{\rho^*}{\rho_s} E_s I_A \quad \text{Equation 2.11}$$

where I_A is the second moment of inertia of the entire enclosed or filled cross sectional area, and E^* is the continuum effective modulus and ρ^*/ρ_s is the relative density or equivalently, the volume fraction of solid in the honeycomb.

To compare the two results we define a continuum effective second moment of inertia, I_0, such that

$$I_0 = \frac{\rho^*}{\rho_s} I_A \qquad \text{Equation 2.12}$$

The ratio of the two flexure rigidities can then be expressed as

$$\frac{E_s I}{E^* I_A} = \frac{E_s I}{\frac{\rho^*}{\rho_s} E_s I_A} = \frac{E_s I}{E_s I_0} = \frac{I}{I_0} \qquad \text{Equation 2.13}$$

with E_s, the Young's modulus of the solid canceling out.

When normalized in this manner the mechanics of solids analysis converges with the continuum solution when the ratio of I/I_0 is equal to one. Thus, predicting the size effect of the elastic response of these structures is reduced to calculating the ratios I/I_0 as a function of specimen-to-cell size ratio. There were several approaches taken to determining this ratio. First for the single walled sample sets, I was calculated using the output of the *SolidWorks™* 3D CAD system *(Dassault Systemes SolidWorks Corp., Concord MA)* on which the geometries were drawn. These calculations where then checked using analytical calculations. For the double walled structures, each sample set was analyzed by first developing an expression for the second moment of each member in the sample set, then examining those derived relationships to find generalized expressions for the second moment for the entire set as well as defining a relationship for I_0 . This relationships were then evaluated and the ratio of I/I_0 reported.

For the single-walled architectures, I was calculated using *SolidWorks™* 3D CAD system. This software calculates numerically the value of I from the geometry of the cross-section. These numerical solutions where then checked using analytical calculations. For the double-walled structures, each architecture was analytically modeled by first deriving an expression for the second moment of each member in the sample set for values of *R* from one to six. These relationships were then examined to determine generalized expressions for I as a function of *n*. The value of I_0, for each architecture was also determined.

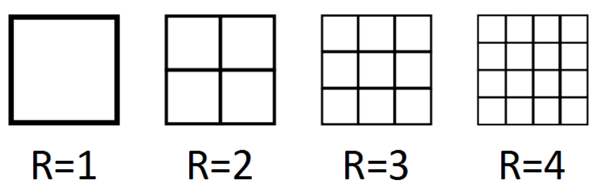

FIGURE 2-2: SINGLE WALLED SQUARE-CELLED MODELED SET

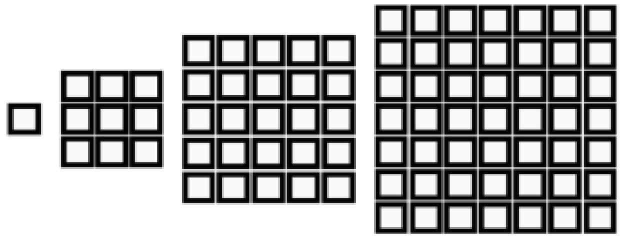

FIGURE 2-3: DOUBLE WALLED SQUARE-CELLED MODELED SET

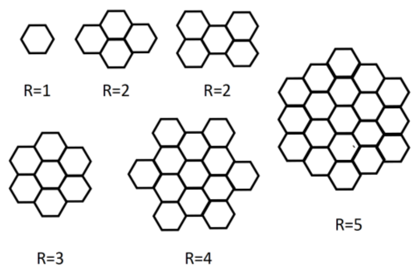

FIGURE 2-4 SINGLE WALLED HEXAGONAL-CELLED MODELED SET

SAMPLE DESIGNS

Two different basic geometries were examined, square-celled honeycombs and regular, hexagonal-celled honeycombs. Within each of these geometries, the cellular architectures were varied systematically to explore their effects on effective stiffness. For example, in Figure 2-2, a set of square-celled samples is shown with a single wall thickness. In this case the sample size is fixed and the cell-size-to-specimen size is varied by reducing the cell size proportionally. Figure 2-3 shows an example of alternative construction rule for square-celled honeycombs. In this case the cell size is fixed and the specimen-to-cell size is varied by adding cells, which results in a double-walled

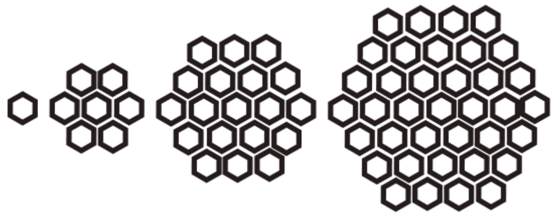

FIGURE 2-5: DOUBLED WALLED HEXAGONAL-CELLED MODELED SET
– CONFIGURATION B

geometry. These construction rules result in a sample set that only has odd values of *R*, i.e. *R* = 1, 3, 5, and 7.

Figure 2-4 shows an example of a set of hexagonal-celled honeycombs with single wall thicknesses for *R* = 1 to 5, with two configurations shown for *R* = 2. And Figure 2-5 shows a sample set of hexagonal double walled architecture that also has odd values of *R* i.e. *R* = 1, 3, 5, and 7. Figure 2-6 and Figure 2-7 are hexagonal-celled honeycombs built using the double wall, constant cell size approach. Figure 2-5 shows an architecture that uses construction rules that also yield only an odd set of specimen-to-cell size ratios. However, Figure 2-6 and Figure 2-7 are constructed in a slightly different way, with the intent of defining an architecture that has both even and odd specimen-to-cell size ratios, yet the second moment of inertia can still be varied. One additional design rule was used for all of the different geometry sets: No half or quarter cells were used, only whole or complete cells were allowed.

FIGURE 2-6 DOUBLED WALLED HEXAGONAL-CELLED MODELED SET – CONFIGURATION C

FIGURE 2-7: DOUBLED WALLED HEXAGONAL -CELLED MODELED SET – CONFIGURATION A

To illustrate the methodology for utilizing a mechanics of solids approach to analyzing the elastic bending response, we present two cases below. First the double-walled, hexagonal celled structures shown in Figure 2-5 are presented. This case is representative of the calculation method used when analyzing architectures where the cell size was held constant and the specimen size was increased to vary the specimen-to-cell size ratio. The second case presented is for single-walled, square honeycombs that were designed to keep the specimen size constant and with decreasing the cell size, as shown in Figure 2-2. A summary of the results of the analyses for the other cases are then presented in Table 2-1.

We start by calculating I for each of the samples using the parallel axis theorem to obtain an expression for I in terms of I_1, the second moment of one unit cell, and

Ay^2, where A is the area of the unit cell and y^2 is the square of the distance from the neutral axis to the second row of cells. Extending this to all the architectures we obtain a series of equations as shown below:

$I(n=0) = I_1$ Equation 2.14

$I(n=1) = 7I_1 + 12Ay^2$ Equation 2.15

$I(n=2) = 19I_1 + 96Ay^2$ Equation 2.16

$I(n=3) = 37I_1 + 372Ay^2$ Equation 2.17

$I(n=4) = 61I_1 + 1020Ay^2$ Equation 2.18

In these expressions it is important to note that *n* is not the specimen-to-cell size ratio but rather a counting variable and that, the specimen-to-cell size, *R*, is given by

R = $(2n+1)$. Equation 2.19

From these equations we can generalize an expression for $I(n)$ such that

$I(n) = (3n^2 + 3n + 1)I_1 + \sum_0^n 2n(5n^2 + 1)\, Ay^2$ Equation 2.20

Equation 2.20 represents the value of I for a cross-section that has the outer perimeter shown in Figure 2-5, but is solid rather than cellular. To obtain the values of $I(n)$ for the cellular architecture, the values of $I(n)$ for the open portions of the cellular structure, I_{holes}, must be subtracted from the $I(n)$ for the solid to obtain I_{net}.

$I_{net,(n)} = I_{solid,(n)} - I_{holes,(n)}$ Equation 2.21

Substituting for I_1 and Ay^2 in terms of S_0 and S_i which are the outer and inner side dimensions of the hexagon as and solving for $I_{solid,(n)}$ and $I_{holes,(n)}$

$$I_{solid,(n)} = (3n^2 + 3n + 1)\left(\frac{5\sqrt{3}}{16}\right)S_o^4 + \sum_0^n 2n(5n^2 + 1)\left(\frac{3\sqrt{3}}{2}\right)S_o^2\left(\frac{3}{4}\right)S_o^2$$

Equation 2.22

$$I_{holes,(n)} = (3n^2 + 3n + 1)\left(\frac{5\sqrt{3}}{16}\right)S_i^4 + \sum_0^n 2n(5n^2 + 1)\left(\frac{3\sqrt{3}}{2}\right)S_i^2\left(\frac{3}{4}\right)S_o^2$$

Equation 2.23

Subtracting the two results in:

$$I_{(n)} = I_{net,(n)} = I_{solid,n} - I_{holes,n}$$

$$= (3n^2 + 3n + 1)\left(\frac{5\sqrt{3}}{16}\right)(S_o^4 - S_i^4) + \sum_0^n 2n(5n^2 + 1)\left(\frac{3\sqrt{3}}{2}\right)\left(\frac{3}{4}\right)S_o^2(S_o^2 - S_i^2)$$

Equation 2.24

$I_{0,(n)}$ and I/I_0 can then be calculated

$$I_{0,(n)} = \frac{\rho^*}{\rho_s} I_{solid,(n)} = (S_o^2 - S_i^2)S_o^2\left[(3n^2 + 3n + 1)\left(\frac{5\sqrt{3}}{16}\right) + \sum_0^n 2n(5n^2 + 1)\left(\frac{3\sqrt{3}}{2}\right)\left(\frac{3}{4}\right)\right]$$

Equation 2.25

$$\frac{I_{(n)}}{I_{0(n)}} = \frac{(S_o^2 + S_i^2)(3n^2 + 3n + 1)\left(\frac{5\sqrt{3}}{16}\right) + S_o^2\sum_0^n 2n(5n^2 + 1)\left(\frac{3\sqrt{3}}{2}\right)\left(\frac{3}{4}\right)}{(S_o^2 - S_i^2)\left[(3n^2 + 3n + 1)\left(\frac{5\sqrt{3}}{16}\right) + \sum_0^n 2n(5n^2 + 1)\left(\frac{3\sqrt{3}}{2}\right)\left(\frac{3}{4}\right)\right]}$$ Equation 2.26

To simplify the expression we define

$$f_1(n) = (3n^2 + 3n + 1)\left(\frac{5\sqrt{3}}{16}\right)$$ Equation 2.27

$$f_2(n) = 2n(5n^2 + 1)\left(\frac{3\sqrt{3}}{2}\right)\left(\frac{3}{4}\right)$$ Equation 2.28

so that I/I_0 can then be expressed as

$$\frac{I_{(n)}}{I_{0(n)}} = \frac{(S_o^2 + S_i^2)f_1(n) + S_o^2\sum_0^n f_2(n)}{S_o^2\left[f_1(n) + \sum_0^n f_2(n)\right]}$$ Equation 2.29

This expression can be further simplified if $S_o = 1$, where S_o is equal to the length of the outer side of and individual cell:

$$\frac{I_{(n)}}{I_{0(n)}} = \frac{(1+S_i^2)f_1(n)+\sum_0^n f_2(n)}{[f_1(n)+\sum_0^n f_2(n)]} \qquad \text{Equation 2.30}$$

Similar calculations were performed for the all the double-walled architectures and the results presented in Table 2-1

TABLE 2-1 EXPRESSIONS FOR DOUBLE-WALLED ARCHITECTURES

Cell Geometry		Fig #	F1(n)	F2(n)
Hex	Double wall	2.5	$(3n^2+3n+1)\left(\frac{5\sqrt{3}}{16}\right)$ **EQUATION 2.31**	$2n(5n^2+1)\left(\frac{3\sqrt{3}}{2}\right)\left(\frac{3}{4}\right)$ **EQUATION 2.32**
Hex 3 wide – odd	Double wall	2.6	$\frac{1}{2}(6n+(-1)^{(n+1)}+3)\left(\frac{5\sqrt{3}}{16}\right)$ **EQUATION 2.33**	$((-1)^{(n-1)} + 3)n^2\left(\frac{3\sqrt{3}}{2}\right)\left(\frac{3}{4}\right)$ **EQUATION 2.34**
Hex 3 wide – even	Double wall	2.7	$\frac{1}{2}(6n-(-1)^{(n+1)} - 3)\left(\frac{5\sqrt{3}}{16}\right)$ **EQUATION 2.35**	$((-1)^{(n)}+3)(n - 1)^2\left(\frac{3\sqrt{3}}{2}\right)\left(\frac{3}{4}\right)$ **EQUATION 2.36**
Square	Double wall	2.3	$\frac{1}{12}(2n+1)^2$ **EQUATION 2.37**	$2(2n+1)\sum_0^n n^2$ **EQUATION 2.38**

The square celled architecture shown in Figure 2-3 has the summation term inside the f_2 function and this slightly changes the final form of I/I_0 so that for this case

$$\frac{I_{(n)}}{I_{0(n)}} = \frac{(1+L_i^2)f_1(n)+f_2(n)}{[f_1(n)+f_2(n)]} \qquad \text{Equation 2.39}$$

Also note that for square-celled architectures, we have replaced S_i with L_i where L_i represents the length of the inside of the square unit cell.

These functions were evaluated by varying the specimen-to-cell size ratios and the volume fractions. A representative set of calculations is presented in Table 2-2.

TABLE 2-2: SHOWING REPRESENTATIVE ANALYSIS FOR HEXAGONAL-CELLED SAMPLES

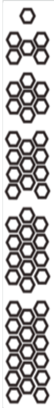

n	Rank	f1			f2				si	Vf	Inet/Io
		f1/C1	C1	f1	f2n/C2	∑fn/C2	C2	∑fn	1>si>0	(1-si^2)	
	(n+1)	1/2(6n+ (-1)^(n+1)+3)	(5*3^.5)/16		((-1)^(n-1)+3)n^2		((3*3^0.5)/2)(3/4)		0.98	0.0396	
n	Rank	f1a	c1	f1	f2a	f2b	c2	f2			a
0	1	1	0.5413	0.541	0	0	1.949	0			1.9604
1	2	5	0.5413	2.706	4	4	1.949	7.794229			1.247526
2	3	7	0.5413	3.789	8	12	1.949	23.38269			1.13392
3	4	11	0.5413	5.954	36	48	1.949	93.53074			1.057478
4	5	13	0.5413	7.036	32	80	1.949	155.8846			1.041479
5	6	17	0.5413	9.202	100	180	1.949	350.7403			1.024552
6	7	19	0.5413	10.284	72	252	1.949	491.0364			1.019702
7	8	23	0.5413	12.449	196	448	1.949	872.9536			1.013504
8	9	25	0.5413	13.532	128	576	1.949	1122.369			1.011441
9	10	29	0.5413	15.697	324	900	1.949	1753.701			1.00852
10	11	31	0.5413	16.779	200	1100	1.949	2143.413			1.00746
11	12	35	0.5413	18.944	484	1584	1.949	3086.515			1.005859
12	13	37	0.5413	20.027	288	1872	1.949	3647.699			1.005244
13	14	41	0.5413	22.192	676	2548	1.949	4964.924			1.004274
14	15	43	0.5413	23.274	392	2940	1.949	5728.758			1.003886
15	16	47	0.5413	25.439	900	3840	1.949	7482.459			1.003254
16	17	49	0.5413	26.522	512	4352	1.949	8480.121			1.002994
17	18	53	0.5413	28.687	1156	5508	1.949	10732.65			1.00256

Next we present the calculations for the architecture where the specimen-to-cell size ratio was varied by decreasing the cell size. The beginning of the sample set analyzed is shown in Figure 2-2. However only the odd values of the specimen-to-cell size ratios, R, were analyzed, i.e. R = 1, 3, 5, 7 and 9 which correspond to n = 0, 1, 2, 3 and 4 . Also, in these calculations we have let the outer size of the specimen, which is constant in this arrangement, arbitrarily set equal one, thus creating a unit-sized cell. We again start by calculating I for each of the architectures using the parallel axis theorem to obtain an expression for I in terms of I_n^*, the second moment of one "hole" in the unit cell, and $A_n {y_n}^2$, where A is the area of the hole and ${y_n}^2$ is the square of the distance from the neutral axis to the second row of cells. Extending this to all the architectures we obtain a series of equations as shown below:

$$I(n=0) = \frac{1}{12} - I_0^* \qquad \text{Equation 2.40}$$

$$I(n=1) = \frac{1}{12} - (9I_1^* + 6A_1y_1^2) \qquad \text{Equation 2.41}$$

$$I(n=2) = \frac{1}{12} - (25I_2^* + 50A_2y_2^2) \qquad \text{Equation 2.42}$$

$$I(n=3) = \frac{1}{12} - (49I_3^* + 196A_3y_3^2) \qquad \text{Equation 2.43}$$

$$I(n=4) = \frac{1}{12} - (81I_4^* + 540A_4y_4^2) \qquad \text{Equation 2.44}$$

$$I(n) = \frac{1}{12} - [(2n+1)^2 I_n^* + 2(2n+1)\sum_0^n n^2\, A_n y_n^2] \qquad \text{Equation 2.45}$$

We can then derive the following relationships (see appendix for details of these calculations)

$$I_n^* = \frac{1}{12}\left(\frac{1-(2n+2)t_n}{(2n+1)}\right)^4 \qquad \text{Equation 2.46}$$

$$A_n = \left(\frac{1-(2n+2)t_n}{(2n+1)}\right)^2) \qquad \text{Equation 2.47}$$

$$y_n{}^2 = \begin{cases} n=0 & 0 \\ n = 1,2,3,\ldots & \left(\frac{1-t_n}{(2n+1)}\right)^2 \end{cases} \qquad \text{Equation 2.48}$$

$$\phi(n) = (1-(2n+1)^2 A_n \qquad \text{Equation 2.49}$$

Where $\phi(n)$ is the relative density of the honeycomb. Setting the relative density for all of the architectures in this set equal, we obtain:

$$\phi(n) = \phi(n-1) \qquad \text{Equation 2.50}$$

$$(2n+1)^2 A_n = (2(n-1)+1)^2 A_{(n-1)} \qquad \text{Equation 2.51}$$

$(2n+1)^2 A_n = (2n-1)^2 A_{(n-1)}$ Equation 2.52

$(2n+1)^2 \left(\frac{1-(2n+2)t_n}{(2n+1)}\right)^2 = (2n-1)^2 \left(\frac{1-(2(n-1)+2)t_{(n-1)}}{(2(n-1)+1)}\right)^2$ Equation 2.53

$(1-(2n+2)t_n)^2 = \left(1-2nt_{(n-1)}\right)^2$ Equation 2.54

$t_n = \frac{2n}{(2n+2)} t_{(n-1)}$ Equation 2.55

$t_n = t_0 \sum_0^n \frac{2n}{(2n+2)}$ Equation 2.56

Substituting Equations 2.45, 2.46, and 2.47 into Equation 2.44 , we obtain

$$I(n) = \frac{1}{12} - [(2n+1)^2 \frac{1}{12}\left(\frac{1-(2n+2)t_n}{(2n+1)}\right)^4$$

$$+2(2n+1)\sum_0^n n^2 \left(\frac{1-(2n+2)t_n}{(2n+1)}\right)^2 \begin{cases} n=0 & 0 \\ n=1,2,3,\ldots & \left(\frac{1-t_n}{(2n+1)}\right)^2 \end{cases}$$ Equation 2.57

And substituting Equation 2.57 into the above equations,

$$I(n) = \frac{1}{12} - [(2n+1)^2 \frac{1}{12}\left(\frac{1-(2n+2)t_0 \sum_0^n \frac{2n}{(2n+2)}}{(2n+1)}\right)^4$$

$$+(2n+1)\sum_0^n n^2 \left(\frac{1-(2n+2)t_0 \sum_0^n \frac{2n}{(2n+2)}}{(2n+1)}\right)^2 \begin{cases} n=0 & 0 \\ n=1,2,3,\ldots & \left(\frac{1-t_0 \sum_0^n \frac{2n}{(2n+2)}}{(2n+1)}\right)^2 \end{cases}$$

Equation 2.58

And we can then find I_0

$I_0 = \frac{\phi}{12}$ Equation 2.59

$I_0 = \left(\frac{1-(2n+2)t_n}{(2n+1)}\right)^2 \frac{1-(2n+1)^2}{12}$ Equation 2.60

Giving us

$$\frac{I(n)}{I_0} =$$

$$\frac{\frac{1}{12}-[(2n+1)^2\frac{1}{12}\left(\frac{1-(2n+2)t_0\sum_0^n\frac{2n}{(2n+2)}}{(2n+1)}\right)^4+2(2n+1)\sum_0^n n^2\left(\frac{1-(2n+2)t_0\sum_0^n\frac{2n}{(2n+2)}}{(2n+1)}\right)^2\begin{bmatrix} n=0 & 0 \\ n=1,2,3,\ldots & \left(\frac{1-t_0\sum_0^n\frac{2n}{(2n+2)}}{(2n+1)}\right)^2 \end{bmatrix}]}{\left(\frac{1-(2n+2)t_n}{(2n+1)}\right)^2\frac{(1-(2n+1)^2}{12}}$$

Equation 2.61

The results of the calculations for this architecture for *n* equal zero to 10 are summarized in Table 2-3.

R	t(0)	t(n)	A(n)	Vf	y(n)^2	I*(n)	I(n)	I(o)	I(n)/i(0)
1	0.0013	0.0013	0.9950	0.005	0.00E+00	8.25E-02	8.30E-04	4.16E-04	2.00
3		0.0006	0.1106	0.005	1.11E-01	1.02E-03	5.54E-04	4.16E-04	1.33
5		0.0004	0.0398	0.005	4.00E-02	1.32E-04	4.99E-04	4.16E-04	1.20
7		0.0003	0.0203	0.005	2.04E-02	3.44E-05	4.75E-04	4.16E-04	1.14
9		0.0003	0.0123	0.005	1.23E-02	1.26E-05	4.62E-04	4.16E-04	1.11
11		0.0002	0.0082	0.005	8.26E-03	5.64E-06	4.54E-04	4.16E-04	1.09
13		0.0002	0.0059	0.005	5.92E-03	2.89E-06	4.48E-04	4.16E-04	1.08
15		0.0002	0.0044	0.005	4.44E-03	1.63E-06	4.44E-04	4.16E-04	1.07
17		0.0001	0.0034	0.005	3.46E-03	9.88E-07	4.41E-04	4.16E-04	1.06
19		0.0001	0.0028	0.005	2.77E-03	6.33E-07	4.38E-04	4.16E-04	1.05
21		0.0001	0.0023	0.005	2.27E-03	4.24E-07	4.36E-04	4.16E-04	1.05

Table 2-3 Representative calculations evaluating Equation 2.61

RESULTS AND DISCUSSION

The results of the calculations for all of the architectures considered are presented below. Figure 2-8 shows the effect of specimen-to-cell size variations of the square-celled, single walled honeycombs with a constant specimen size, where the normalized second moment or flexure stiffness, I/I_0 , is plotted versus the specimen-to-cell size ratio, *R*. From this plot, it is apparent that a significant size effect is predicted at small specimen-to-cell ratios. For example, at a specimen-to-cell size ratio of one (*R*

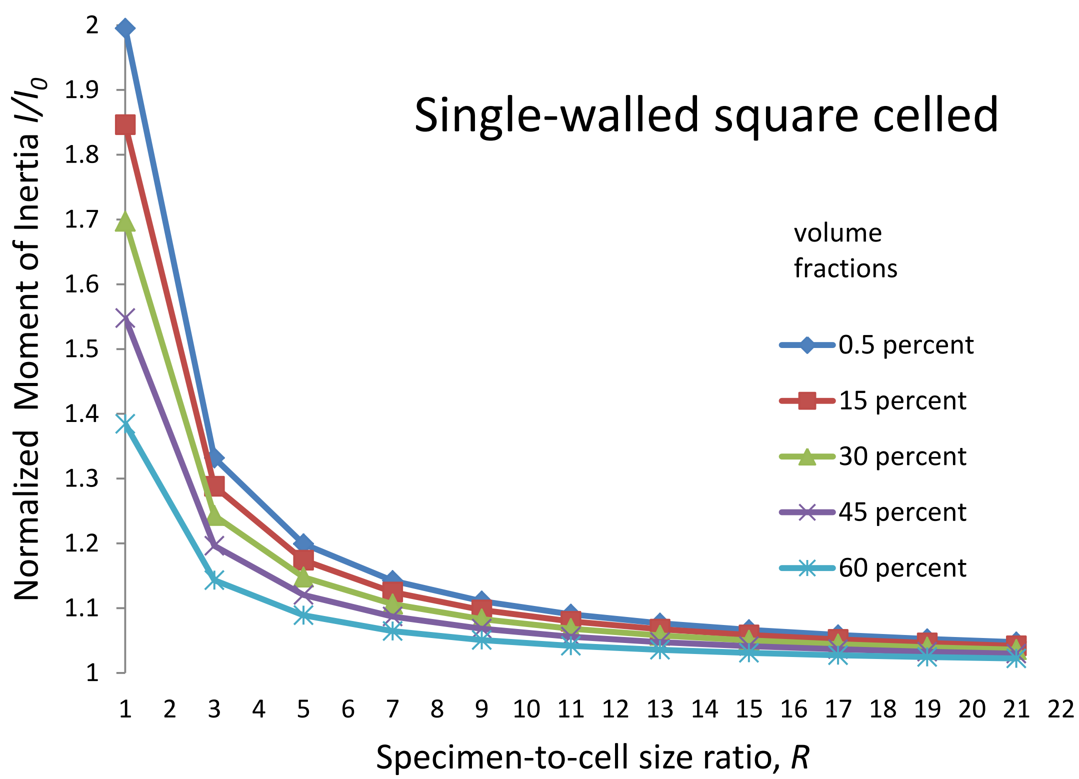

FIGURE 2-8: GRAPH OF SINGLE WALLED SQUARE CELLED HONEYCOMBS SHOWING THE CALCULATED NORMALIZED MOMENT OF INERTIA VERSUS SPECIMEN-TO-CELL RATIO FOR FIVE VOLUME FRACTIONS

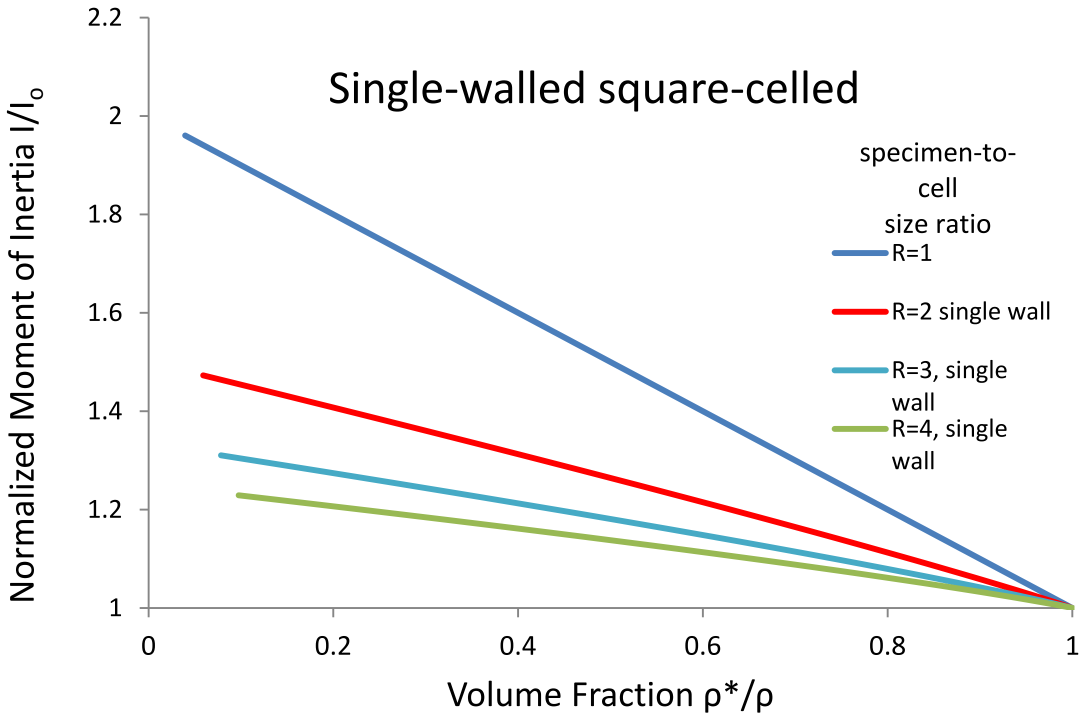

FIGURE 2-9: GRAPH OF SINGLE WALLED SQUARE-CELLED HONEYCOMBS SHOWING THE CALCULATED NORMALIZED MOMENT OF INERTIA VERSUS VOLUME FRACTION OF SOLID FOR FOUR SAMPLES WITH SPECIMEN-TO-CELL SIZE RATIOS OF ONE TO FOUR

equal one), the structures with a small volume fraction of solid have an I/I_0 approaching two, which represents a hundred percent increase in flexural stiffness over the continuum model. At sixty percent volume fraction of solid, which would represent a thick-walled honeycomb, I/I_0 = 1.4 which is a forty percent increase over the continuum predictions. This drops off as the specimen-to-cell ratio increases, until at a specimen-to-cell size ratio of ten to one, it is reduced to only a ten percent increase over continuum estimates even at low volume fractions. One range of interest is for volume fractions of less than thirty percent (thin-walled honeycombs). For these architectures we predict a significant size effect persisting until at least *R* equals ten. Full agreement with the continuum calculations ($I/I_0 \rightarrow 1$) occurs at *R*s greater than twenty, although the size effect between *R* equal ten and *R* equal twenty is minor.

Figure 2-9 shows the results of the calculations for the same square-celled honeycombs, but here the relative stiffness is plotted versus volume fraction for *R* equal one to *R* equal four. For *R* equal one -- I/I_0 is approximately two and this value drops as volume fraction increases until it reaches one, as expected at a hundred percent volume fraction. In a similar manner we can see that for *R* equal two, I/I_0 equal to one

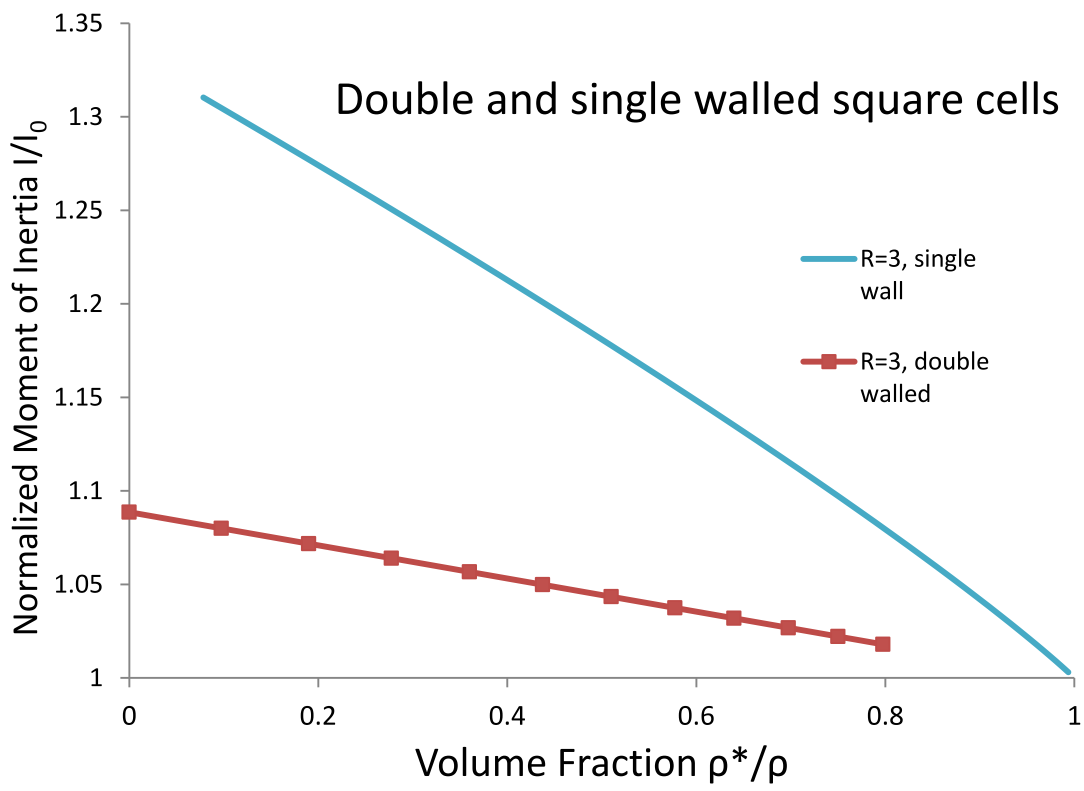

FIGURE 2-10: GRAPH OF DOUBLE AND SINGLE WALLED SQUARE CELLED HONEYCOMBS SHOWING NORMALIZED MOMENT OF INERTIA AS A FUNCTION OF THE VOLUME FRACTION

and a half, dropping to I/I_0 is equal to one and quarter for R equal four.

Figure 2-10 shows that the size effect is much larger for the single-walled architecture than for the double-walled architecture. This results from differences in how the solid material is distributed across the cross section of beams, i.e. there is more mass further from the neutral axis at a given volume fraction for the single-walled architectures than for the double-walled architectures.

The other cases we considered are the hexagonal-celled honeycombs which are presented in Figure 2-11 and Figure 2-12. From Figure 2-11, we see that response of the hexagonal cells is similar to the response of the square celled honeycombs. For

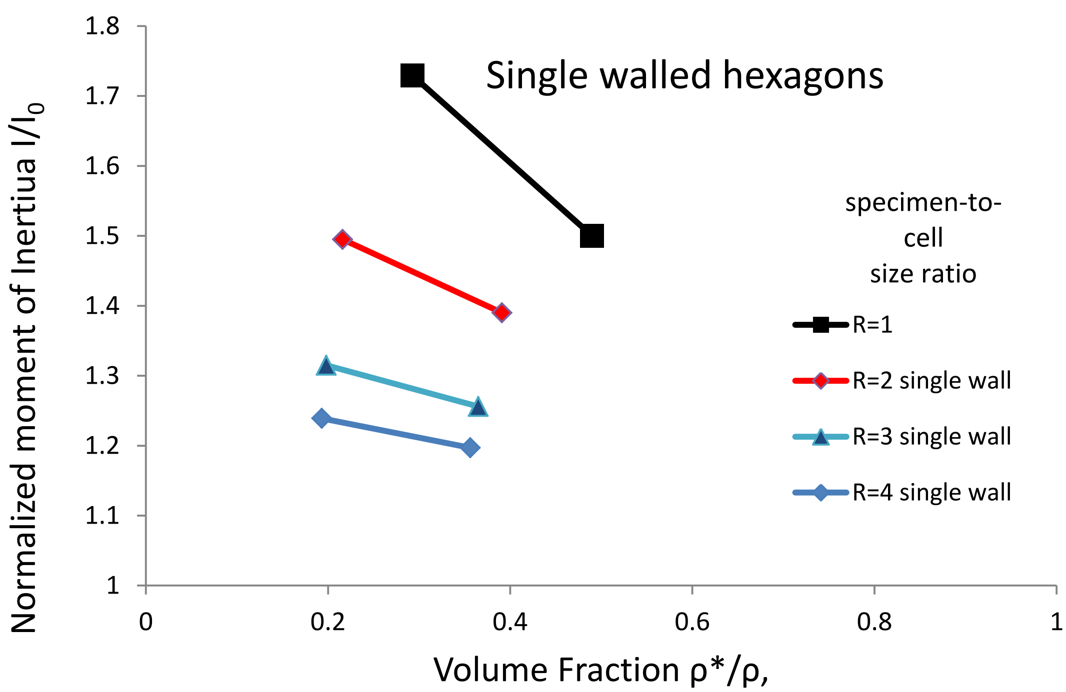

FIGURE 2-11: GRAPH FOR SINGLE-WALLED HEXAGONAL-CELLED HONEYCOMBS SHOWING THE CALCULATED NORMALIZED MOMENT OF INERTIA VERSUS VOLUME FRACTION FOR FOUR SAMPLES WITH SPECIMEN-TO-CELL SIZE RATIOS OF ONE TO FOUR

example, for *R* equal one, I/I_0 approaches two at low volume fractions, decreasing with both specimen-to-cell size ratio and volume fraction. In Figure 2-11, the relative stiffness is plotted for single walled hexagonal-celled architectures for *R* = 1 to *R* = 4. Figure 2-12 the relative stiffness of the double walled is plotted for *R* = 1 to *R* = 3. These figures again show that the size effect is greatest for single-walled architectures and decreases with both wall thickness and volume fraction.

CONCLUSIONS

As we mentioned earlier, the goals of this part of our work are to 1) determine the magnitude of the size effect for specimens with small specimen-to-cell size ratios 2) determine the necessary specimen-to-cell size ratio where a continuum model can be used to predict effective stiffness, 3) examine the influence of relative density on the size effect and 4) examine the effects of cell geometry by varying the cell shape and

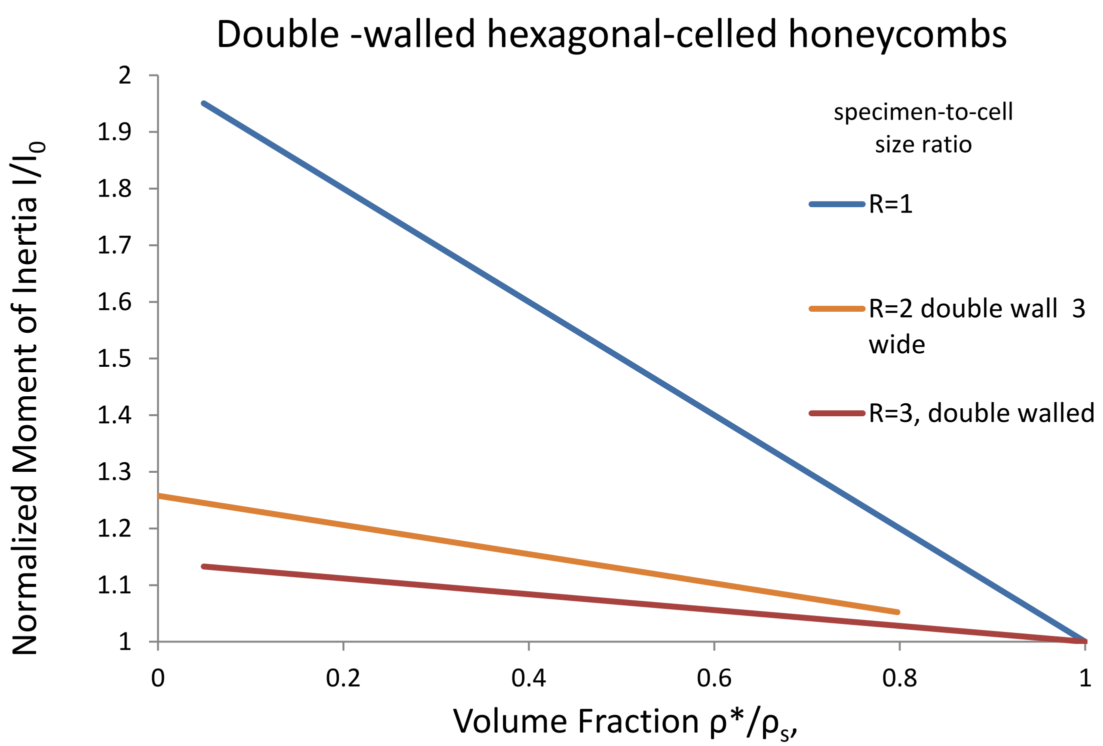

2-12: GRAPH OF DOUBLE WALLED HEXAGONAL-CELLED HONEYCOMBS SHOWING THE CALCULATED NORMALIZED MOMENT OF INERTIA VERSUS VOLUME FRACTION FOR FOUR SAMPLES WITH SPECIMEN-TO-CELL SIZE RATIOS OF ONE TO THREE configuration choices such as single versus double-walled structures. We predicted an increase in stiffness of up to a hundred percent for both the square and hexagonal samples at   equal one and decreasing with both specimen-to-cell size ratio and volume fraction. For volume fractions of less than the thirty percent (thin-walled honeycombs) with single wall architectures, we predict a significant size effect persisting until at least *R* equal ten. Full agreement with the continuum calculations (I/I_0 approaches one) occurs at *R* is greater than twenty, although the size effect between *R* equal ten and *R* equal twenty is minor. The effect of choosing between double walled or single-walled construction is significant and shows that the size effect is much larger for the single-walled architecture than for the double-walled architecture. Again this results from differences in how the solid material is distributed across the cross section of beams, with more mass further from the neutral axis at a given volume fraction for the single-walled architectures than for the double-walled architectures.

Chapter 3: Characterization of the size effect in the elastic response of honeycomb beams in bending.

MOTIVATION AND SCOPE

Measurement of the Young's modulus of foam and honeycomb structures has been recognized as a difficult task when the size of the sample being tested becomes too small in relation to the size of the cells in the foam or honeycomb. (Brezny and Green 1990) Previous measurements made on small samples "simply didn't make sense" and in practical terms, few attempts were made to measure and characterize the elastic properties of samples below a certain specimen size. This effect which is also known as an edge effect has not been studied in detail previously.

We have designed, built and tested polyamide honeycombs to characterize the effect of specimen-to-cell size ratio variation on the Young's modulus of a honeycomb in out-of-plane bending. The test sample sets were designed using a 3D CAD program, converted to digital files, and then transferred to and built using a free form fabrication process from a polyamide powder. The samples were tested on a mechanical test frame in three-point bending and four-point bending. Results of experiments are compared to the predicted behavior using three models, an elastic continuum model as described by Gibson and Ashby (Gibson and Ashby 1997), a conventional mechanics of solid analysis, and a full elastic analysis. Finally, additional issues associated with the difficulty in measuring the Young's modulus of honeycomb structures are addressed and discussed.

DESIGN AND FABRICATION OF SAMPLES

Honeycombs with two different cellular geometries, square and hexagonal, each with two different volume fractions, were designed using *SolidWorks™.* The geometries of honeycombs with square unit cross section cells are shown in Figure 3-1 and the geometries of honeycombs with regular hexagonal cross section unit cells are shown in Figure 3-2. The lengths of the samples, out of the plane of the page, were standardized at a length of 200 mm. The square-celled samples had cross-sectional dimensions of twenty mm by twenty mm while the dimensions of the hexagonal-celled samples varied,

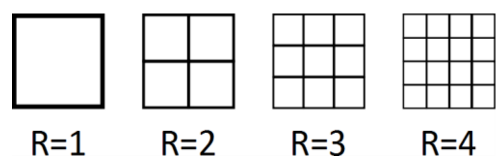

FIGURE 3-1: CROSS-SECTION GEOMETRY OF SQUARE-CELLED HONEYCOMB SAMPLE SET, SINGLE-WALLED WITH *R* = 1-4

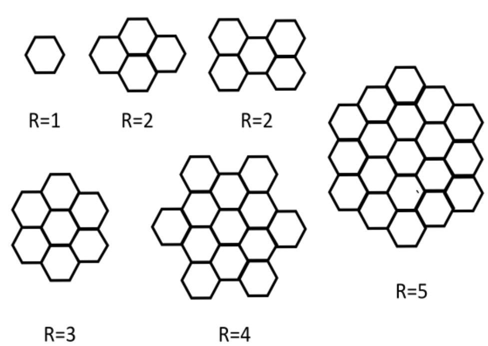

FIGURE 3-2: CROSS SECTION GEOMETRY OF HEXAGONAL-CELLED HONEYCOMB SAMPLE SET, WITH SINGLE WALL CONSTRUCTION AND CONSTANT CELL SIZE, *R*= 1-5

as described below.

Two differing approaches were taken in designing the square and hexagonal-celled honeycombs. The square-celled samples had a constant specimen size and the variation in the specimen-to-cell size ratio was accomplished by varying the size of the cell. This required varying the wall thickness for each sample set to maintain a constant volume fraction for all values of *R*. However, the geometry of a hexagon does not allow construction of an analogous sample set. Thus, for the hexagons, the samples were built using a constant cell size of eight millimeters and the variation in the specimen-to-cell size ratio was accomplished by increasing the height and width of the specimens. A summary of the sample set construction rules is provided in Table 3-1.

The samples were built using a Hi-Q Selective Laser Sintering System (*3D Systems, Rockhill SC).* Selective Laser Sintering (SLS) is a powder-based, layer-based, additive manufacturing process shown schematically below in Figure 3-3. SLS is one of several competitive additive manufacturing processes that have been invented and commercialized during the past twenty years. In the SLS process a part is constructed one layer at a time inside a thermally controlled process chamber which is held a temperature slightly below the melting point of the polymer being used. A laser beam is raster scanned across the surface of a layer of powder, turning on and off to selectively sinter or fuse the polymer powder particles into a shape defined by a computer which has converted a three dimensional CAD image into profile slices equal in thickness to the powder layer thickness. The powder is deposited in thin layers, in the range of 0.15 to

0.25 mm deep, uniformly across a piston. After a given layer has been fused, the piston is lowered and a new layer of powder is added on top of the just completed layer. The new layer is then fused, based on the defined shaped, and in this manner a three-dimensional object can be fabricated from multiple layers. (Beaman 1997)

Table 3-1: Honeycomb sample set design rules

Cell Shape	Specimen-to-cell size ratio (R)	Fabrication Method	Volume fraction of solid
Square	1 to 4	Constant Specimen Size, Variable Cell Size	Constant = 0.15
Square	1 to 4	Constant Specimen Size, Variable Cell Size	Constant= 0.25
Regular Hexagon	1 to 6	Constant Cell Size Variable Specimen Size	Varying = 0.30 to 0.19
Regular Hexagon	1 to 6	Constant Cell Size Variable Specimen Size	Varying = 0.49 to 0.35

Two grades of polyamide 12 were used in building the parts. The first is 3D *Systems Corporation,* Duraform® PA and the second is an equivalent PA 12 made by *Advanced Laser Materials LLC, (Belton, Texas).* The published mechanical data for both polymers is presented in Appendices B and C.

Table 3-2: Selective Laser Sintering Processing Parameters

	Units	Quantity
Part Bed Temperature	(^{o}C)	170
Feed Bed Temperature	(^{o}C)	140
Laser Power	Watts	40
Powder Layer Level	(mm)	7

While the two polymers appear nearly identical and they are from the same primary polymer supplier, all data was analyzed separately for each. Only virgin, non-recycled powder was used.

Prior to beginning to build the samples used for this project, the thermal distribution characteristics and the laser power levels of the SLS system were calibrated and adjusted to bring the platform into operating specifications. This required replacement of the part piston seal and refocusing of the laser. The build and part processing parameters were held constant between all runs and are presented in Table 3-2. The samples were built with a 2.5 cm (one inch) powder warm up layer and utilized

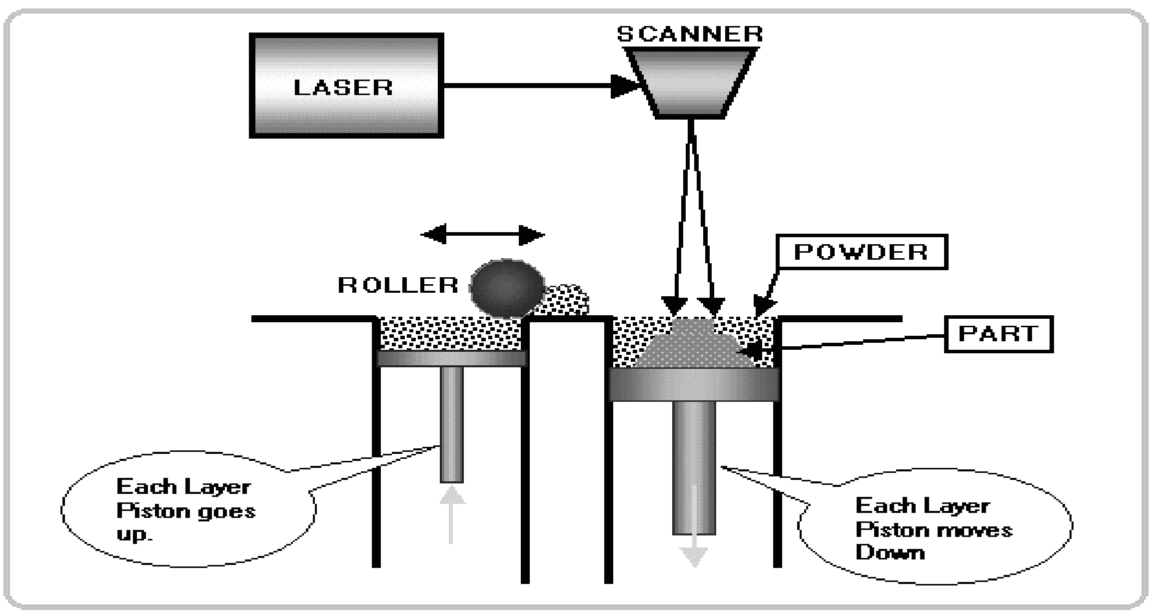

FIGURE 3-3: SCHEMATIC OF SELECTIVE LASER SINTERING PROCESS

a heat shield which was used to create a uniform temperature distribution before building the first layer. Fabrication of the samples was started 0.625 cm (0.25 inches)

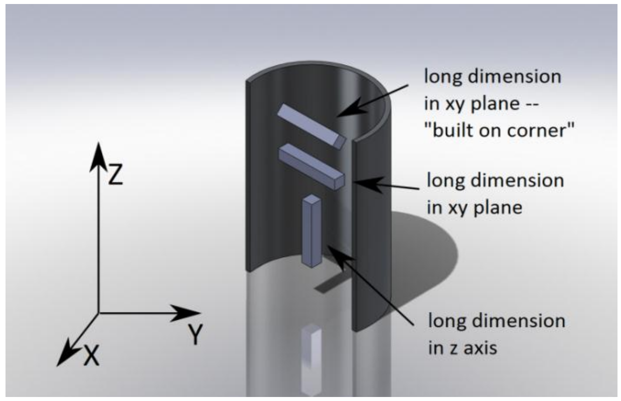

FIGURE 3-4: ORIENTATIONS OF PARTS RELATIVE TO THE BUILD DIRECTION (Z-AXIS)

above the heat shield. A slow, fully controlled cool down process was used to increase the uniformity of temperature and thus increase the uniformity of the resulting mechanical properties of the finished part.

Initially, several solid test parts were built to evaluate the influence of the build orientation on the elastic properties of the polymer. The test parts were built in three

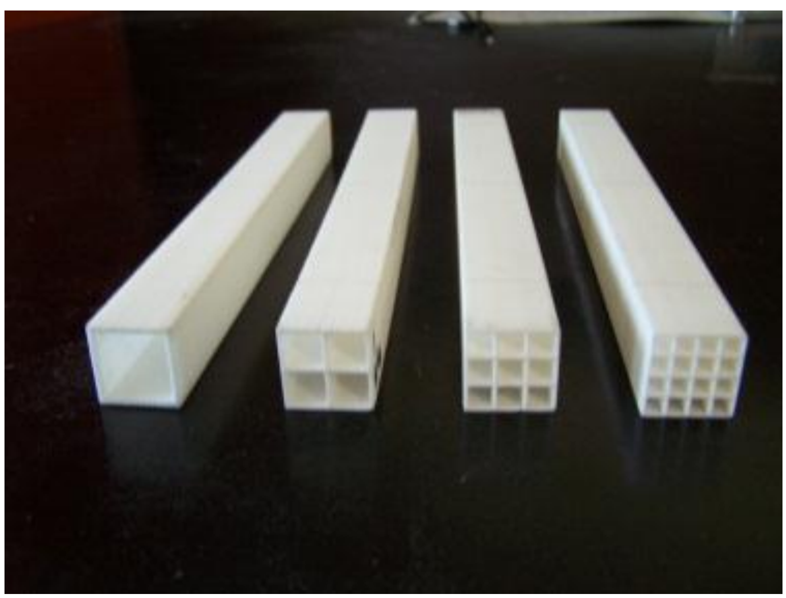
FIGURE 3-5: A SQUARE-CELLED HONEYCOMB SAMPLE SET FABRICATED USING SLS

orientations as shown in Figure 3-4. Two of these samples were built with the long axis of the specimen parallel to the *x*-*y* plane. In one case the largest face of the specimen was parallel to the *x*-*y* plane. In the other case the specimen was rotated forty-five degrees so that it was “built on a corner.” The third sample was built so that the long axis was parallel to the *z*-axis.

A photograph of a representative set of square samples, built using SLS is shown In Figure 3-5 and a photograph of a representative set of hexagonal samples is shown in Figure 3-6. An item to note is that two of the square-celled samples with specimen-to-cell sizes of three and four and with solid fractions of fifteen percent had wall thicknesses that were too thin to be successfully built using the SLS system. Thus, these samples could not be tested and these data points do not appear in the presented results.

FIGURE 3-6: A HEXAGONAL-CELLED HONEYCOMB SAMPLE SET FABRICATED USING SLS

Testing of samples

Three-point bending and four-point bending tests were performed to determine

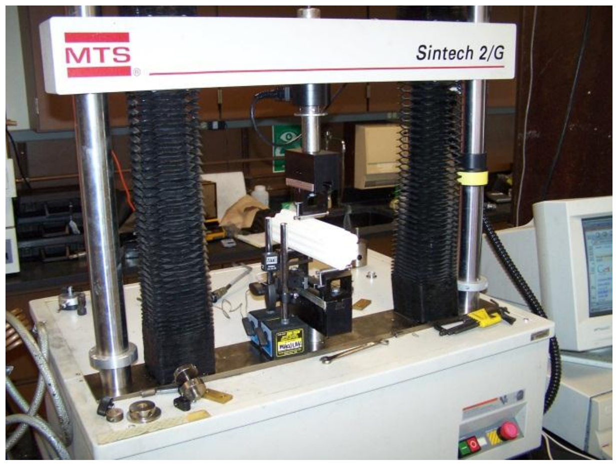

FIGURE 3-7: PHOTOGRAPH OF TEST FRAME SHOWING SAMPLE UNDERGOING FOUR- POINT BENDING

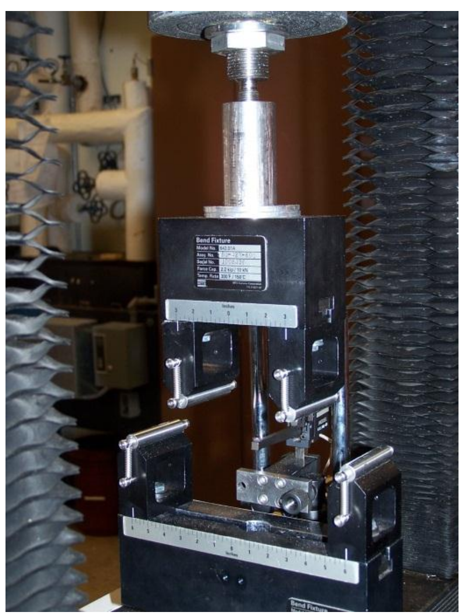

FIGURE 3-8:BENDING TEST FIXTURE, USED FOR BOTH 3PT. AND 4PT. TESTING, SHOWN CONFIGURED FOR 4 PT TESTING

the elastic response of the samples. Testing of the samples was performed on a MTS Sintech 2/G test frame shown in Figure 3-7 equipped with a 10,000N load cell and an MTS Model 642.01A bend bending jig shown in Figure 3-8. The bending jig was outfitted with 2.5 mm diameter, spring-retained, steel rollers and a MTS Model 632.06H-20 deflectometer. Testing methods generally followed ASTM standards for measuring flexural properties in plastics (D790 n.d.) (D6272 n.d.), although there were some modifications to account for the differences required for testing on honeycomb structures rather than solid samples and differences in the sample sizes.

THREE-POINT BENDING TESTS

The three-point bending setup is shown schematically in Figure 3-9. The sample rests on two supports and is loaded by means of a roller located midway between the supports. The span between the supports, L, is 150 mm and steel rollers with a diameter of 2.5 mm are used to both support and load the sample. The deflectometer is placed at the center-point of the sample on the bottom face of the sample and

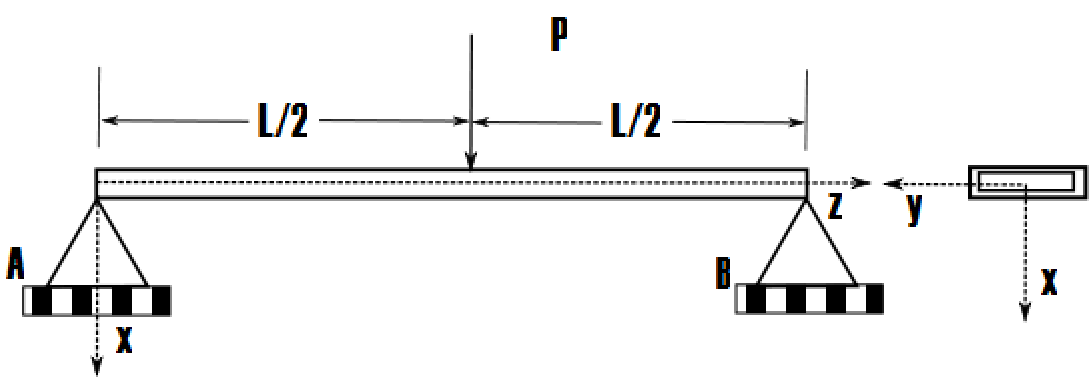

FIGURE 3-9: GEOMETRY USED FOR THREE-POINT BENDING TESTS

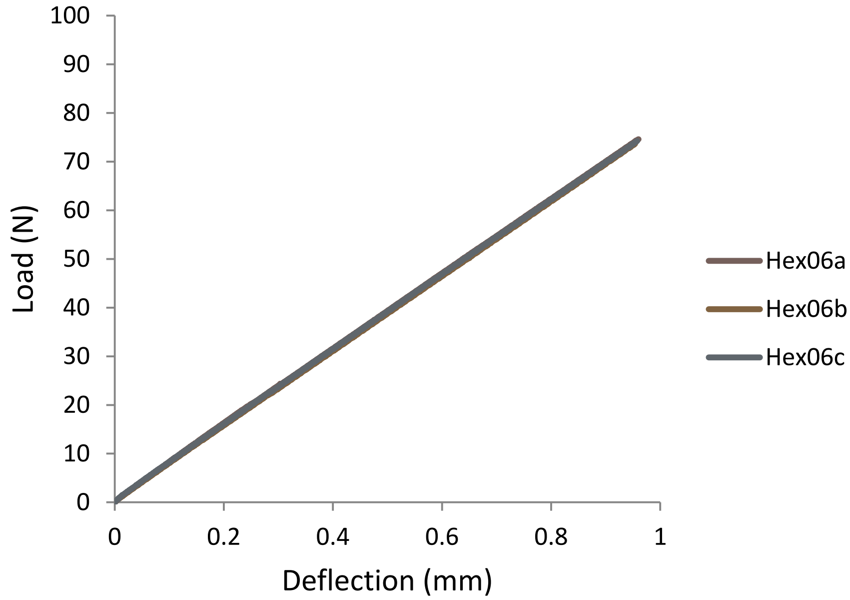

FIGURE 3-10 THREE-POINT BENDING OF A HONEYCOMB WITH REGULAR HEXAGONAL CELLS

directly beneath the load point. All samples were tested at a constant displacement rate of 1 mm/min. The load cell and deflectometer were calibrated prior to testing. Since the strains were small enough that no measurable plastic deformation took place, each sample was tested multiple times. Data from the load cell, the deflectometer and the cross head position was collected for each test. To verify that the system was operating correctly, the Young's modulus for a mild steel sample was measured and evaluated. The measured modulus for the mild steel test sample was 198 GPa which agrees well with the expected values of approximately 200 GPa.

In Figure 3-10 a representative graph shows the load versus center-point deflection from a three-point test on a hexagonal-celled honeycomb. This data is from the loading curve only, and we see generally that the response is linear. In this figure the sample designations *a*, *b* and *c* in the legend represents the three sides, 120 degrees apart, that each hexagonal sample was tested on. The variation in this data was then used to bracket the error or uncertainty in the measurements. It is interesting to note that the unloading data for the three-point testing showed hysteresis, where at the beginning of the unloading curve, the slope was greater than the slope for the loading line. This variation in slope upon unloading occurs for only a small displacement before returning to the slope measured during loading. This apparent “stiffening” upon reversing of the loading, is thought to be a result of sticking of the rollers and is not addressed further.

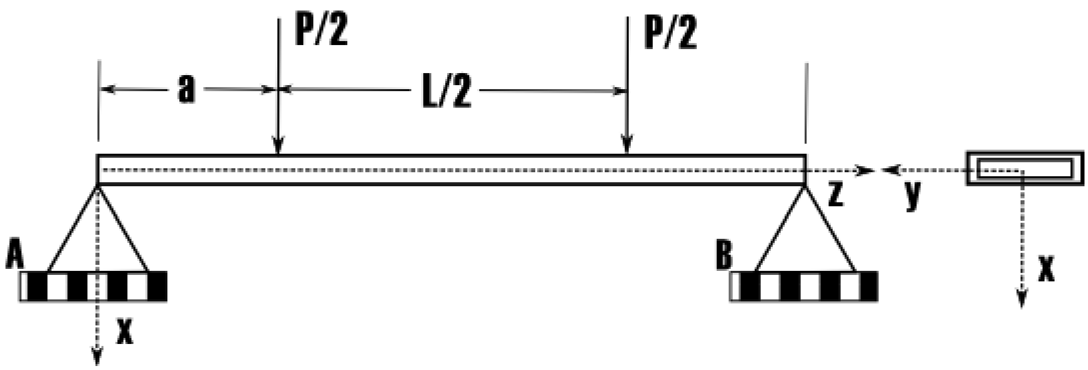

FIGURE 3-11 GEOMETRY USED FOR FOUR-POINT BENDING TESTS

Four-point bending tests

The four-point bending was conducted on the same test frame and bend fixture as used for the three-point bending described previously. The four-point bending configuration is shown in Figure 3-11. The sample is supported by two lower support rollers with a diameter of 2.5 mm positioned on the outside of the bend fixture and separated by a distance of 150 mm. The sample is then loaded from the top by two additional 2.5 mm diameter rollers, which are separated from each other by 75 mm ($L/2$) and are inset from the bottom support roller by 37.5 mm. A deflectometer is used to measure the center-point deflection while the displacement of the upper rollers is captured using the cross head displacement. Like for the three-point tests, all samples were tested at a constant displacement rate of 1 mm/min.

The load cell and deflectometer were calibrated prior to beginning the testing. Each sample again was tested in multiple orientations and each sample was tested multiple times. Data from the load cell, the deflectometer and the cross head position were collected for each test. In Figure 3-12 representative data collected from a four-point test from a hexagonal solid sample is presented. Both center-point data taken with the deflectometer and crosshead displacement are shown. These points are labeled U_a and U_b, respectively, as shown in Figure 3-13. The *a*, *b* and *c* designations represent three successive tests on each of the three sides of the hexagonal beam. The nearly linear data in Figure 3-12 are from the deflectometer while the crosshead displacement data appears as two piece-wise linear curve sections. The first section of the cross head response results from a "settling-in" of the steel rollers in the sample caused by localized deformation. Additional discussion about localized deformation follows in Chapter 4.

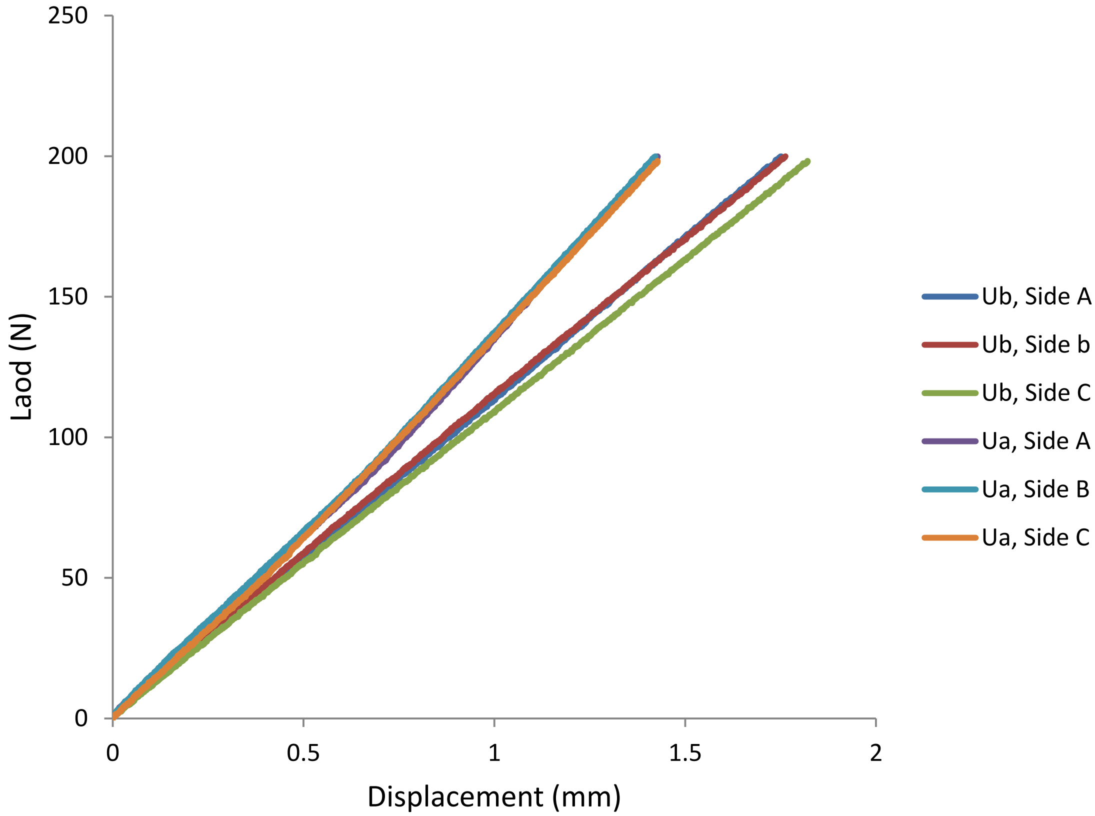

FIGURE 3-12: LOAD DISPLACEMENT FOR REGULAR HEXAGONAL-CELLED HONEYCOMBS TESTED IN FOUR-POINT BENDING TEST RESULTS

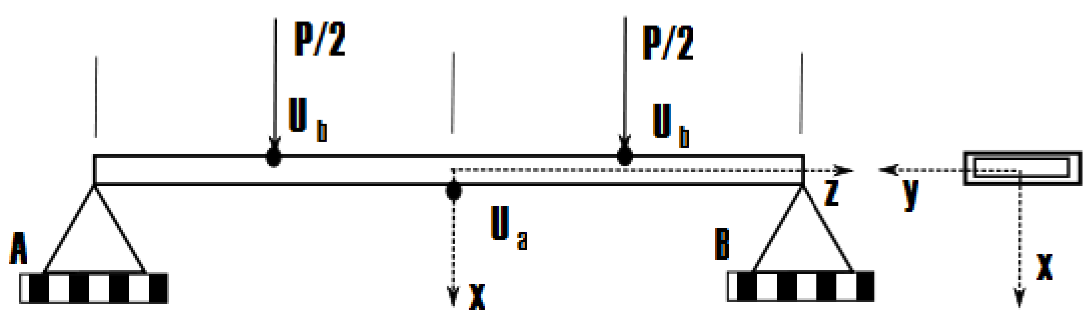

FIGURE 3-13: GEOMETRY USED FOR FOUR-POINT BENDING TESTS SHOWING U(A) AND U(B)

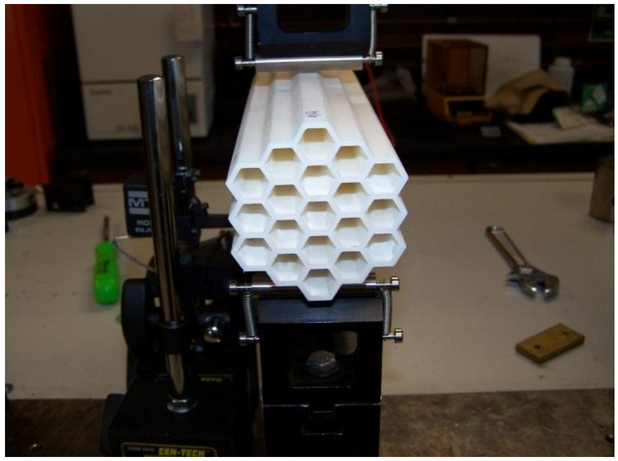

FIGURE 3-14: PHOTOGRAPH OF HEXAGONAL HONEYCOMB SAMPLE BEING TESTED IN THREE-POINT BENDING

ANALYSIS OF DATA

As mentioned previously, one of the aims of this work was to compare the results of experiments to the predicted behavior using three models – an elastic continuum model as described by Gibson and Ashby, a conventional mechanics of solid analysis, and a full elastic analysis. These models increase in complexity from the continuum model to mechanics of solids model to the full elastic analysis.

CONTINUUM MODEL

Classical continuum mechanics views bodies as homogenous and continuous and is used in engineering analysis of deformable objects under small strains. When applied to honeycombs, which are loaded in out-plane bending, it predicts the flexure stiffness is only a function of the solid volume fraction of material and the Young's modulus of the solid, thus the continuum model does not predict a scale dependence. Predictions using the continuum model can be made without load displacement data if an accurate value for the Young's modulus is known.

MECHANICS OF SOLIDS MODEL

The well-known expression used for evaluating the three-point bending data is shown in Equation 3.1 where $u(z)$is the displacement in the *x* direction as a function of the length *z* as shown in Figure 3-9, and L is the length between the two supports on the bending jig, also as shown in Figure 3-9. Equation 3.2 shows this expression evaluated at $z = L/2$, the mid-point of the sample and the location of the deflectometer during testing.

$$u(z) = \begin{Bmatrix} \frac{Pz(4z^2-3L^2)}{48EI} & for\ 0 \leq z \leq \frac{L}{2} \\ \frac{P(z-L)(L^2-8Lz+4z^2)}{48EI} & for\ \frac{L}{2} < z \leq L \end{Bmatrix} \quad \text{Equation 3.1}$$

$$u(z = L/2) = \frac{PL^3}{48EI} \quad \text{Equation 3.2}$$

The conventional mechanics of solids equation used to evaluate the four-point bending results is Equation 3.3, where $u(z = L/2)$ is the displacement in the x direction as a function of the length *z* along the beam, evaluated at $z = L/2$ or the mid-point of the beam, with *L* being the length between the two supports on the bending jig as shown in Figure 3-11 and *a* being determined by the location of the load as shown in the same figure.

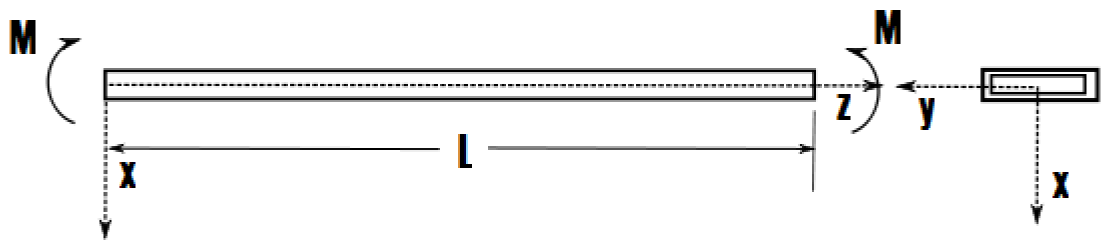

FIGURE 3-15: BEAM IN PURE BENDING

$$u(z = L/2) = \frac{Pa}{24EI}(3L^2 - 4a^2) \qquad \text{Equation 3.3}$$

In both three-point and four-point bending we can rearrange the equations and use the deflectometer and the load data, to solve for EI, the beam flexural rigidity, which we have defined in the previous chapter.

Analysis of bending data

We have previously described a method for analyzing load and displacement data to determine flexural modulus. This is traditionally done using a mechanics of solids approach. The analysis presented here is an alternative method that utilizes elasticity theory to determine the relative displacement between two arbitrary points on the beam U_a and U_b as shown in Figure 3-13.

Given a beam in pure bending, as shown in Figure 3-15, we can derive the following relationships

$$\sigma_z = \frac{E\,x}{R} \qquad \text{Equation 3.4}$$

Where, σ_z is the component of stress in the z direction,
E is the Young's modulus,

R is the **r**adius of curvature of the beam,
X is the position on the beam in the x-direction

$$\sigma_x = \sigma_y = \tau_{xy} = \tau_{xz} = \tau_{yz} = 0 \qquad \text{Equation 3.5}$$

Where ,σ_x is the normal component of stress parallel to *x*-axis,
σ_y is the normal component of stress parallel to *y*-axis,
τ_{xy} is the shearing-stress component in the *xy*-plane,
τ_{xz} is the shearing-stress component in the *xz*-plane, and
τ_{yz} is the shearing-stress component in the *yz*-plane

$$M = \int \sigma_x \, x \, dA = \frac{E}{R} \int x^2 dA = \frac{EI_y}{R} \qquad \text{Equation 3.6}$$

Where,M is the bending moment,
A is the cross-sectional area,
E is the Young's modulus,
I_y is the moment of inertia of a cross section with respect to the *y* axis, and
x is displacement in the *x* direction

From this equation we find

$$\frac{1}{R} = \frac{M}{EI_y} \qquad \text{Equation 3.7}$$

The strains can be expressed as follows

$$\epsilon_z = \frac{\partial w}{\partial z} \qquad \text{Equation 3.8}$$

$$\epsilon_x = \frac{\partial u}{\partial x} \qquad \text{Equation 3.9}$$

$$\epsilon_y = \frac{\partial v}{\partial y} \qquad \text{Equation 3.10}$$

Where, ϵ_z is the unit elongation parallel to *z* axis,

ϵ_x is the unit elongation parallel to *x* axis,

ϵ_y is the unit elongation parallel to *y* axis,

w is the component of displacement parallel to *z* axis,

u is the component of displacement parallel to *x* axis, and

v is the component of displacement parallel to *y* axis

Thus,

$$\frac{\partial w}{\partial z} = \frac{x}{R} \quad \text{Equation 3.11}$$

$$\frac{\partial u}{\partial x} = -\upsilon \frac{x}{R} \quad \text{Equation 3.12}$$

$$\frac{\partial v}{\partial y} = -\upsilon \frac{x}{R} \quad \text{Equation 3.13}$$

Where, υ is Poisson's ratio

From the shear stresses we have

$$\frac{\partial u}{\partial y} + \frac{\partial v}{\partial x} = 0 \quad \text{Equation 3.14}$$

$$\frac{\partial u}{\partial z} + \frac{\partial w}{\partial x} = 0 \quad \text{Equation 3.15}$$

$$\frac{\partial v}{\partial z} + \frac{\partial w}{\partial y} = 0 \quad \text{Equation 3.16}$$

Rearranging Equation 3.11 and then integrating

$$\partial w = \frac{x}{R}\, \partial z \quad \text{Equation 3.17}$$

$$w = \frac{xz}{R} + w_0 \quad \text{Equation 3.18}$$

Where w_0 is a function of *x* and *y* only.

We can then rearrange Equation 3.15 and Equation 3.16 and substitute Equation 3.18 into both

$$\frac{\partial u}{\partial z} = -\frac{\partial w}{\partial x} = -\frac{\partial\left(\frac{xz}{R} + w_0\right)}{\partial x} = -\frac{xz}{R} - \frac{\partial w_0}{\partial x} \qquad \text{Equation 3.19}$$

$$\frac{\partial v}{\partial z} = -\frac{\partial w}{\partial y} = -\frac{\partial\left(\frac{xz}{R} + w_0\right)}{\partial y} = -\frac{\partial w_0}{\partial y} \qquad \text{Equation 3.20}$$

Then integrating these two expressions we get

$$u = -\frac{z^2}{2r} - \frac{z\partial w_0}{\partial x} + u_0 \qquad \text{Equation 3.21}$$

$$v = -\frac{z\partial w_0}{\partial y} + v_0 \qquad \text{Equation 3.22}$$

Where u_0 and v_0 are functions of x and y only. Plugging these back into Equations 3.12 and 3.13

$$\frac{\partial u}{\partial x} = \frac{\partial\left(-\frac{z^2}{2r} - \frac{z\partial w_0}{\partial x} + u_0\right)}{\partial x} = -\frac{z\partial^2 w_0}{\partial x^2} + \frac{\partial u_0}{\partial x} = -\upsilon\frac{x}{R} \qquad \text{Equation 3.23}$$

$$\frac{\partial v}{\partial y} = \frac{\partial\left(-\frac{z\partial w_0}{\partial y} + v_0\right)}{\partial y} = -\frac{z\partial^2 w_0}{\partial y^2} + \frac{\partial v_0}{\partial y} = -\upsilon\frac{x}{R} \qquad \text{Equation 3.24}$$

And recognizing

$$\frac{\partial^2 w_0}{\partial y^2} = \frac{\partial^2 w_0}{\partial x^2} = 0 \qquad \text{Equation 3.25}$$

Reducing the two expressions and rearranging

$$\partial u_0 = -\upsilon \frac{x}{R} \partial x \qquad \text{Equation 3.26}$$

$$\partial v_0 = -\upsilon \frac{x}{R} \partial y \qquad \text{Equation 3.27}$$

Integrating the two functions we obtain

$$u_0 = -\upsilon \frac{x^2}{2R} + f_1 \qquad \text{Equation 3.28}$$

$$v_0 = -\upsilon \frac{xy}{R} + f_2 \qquad \text{Equation 3.29}$$

Where f_1 is a function of *y* only and f_2 is a function of *x* only. Then substituting these back into Equation 3.21 and Equation 3.22

$$u = -\frac{z^2}{2r} - \frac{z\partial w_0}{\partial x} - \upsilon \frac{x^2}{2R} + f_1 \qquad \text{Equation 3.30}$$

$$v = -\frac{z\partial w_0}{\partial y} - \upsilon \frac{xy}{R} + f_2 \qquad \text{Equation 3.31}$$

Recalling Equation 3.14, we can take the derivative of Equation 3.30 and Equation 3.31 and substituting them into Equation 3.14

$$\frac{\partial f_1}{\partial y} - \frac{z\partial^2 w_0}{\partial x \partial y} + \frac{\partial f_2}{\partial x} - \frac{z\partial^2 w_0}{\partial x \partial y} - \frac{\upsilon y}{R} = 0 \qquad \text{Equation 3.32}$$

Recognizing

$$\frac{\partial^2 w_0}{\partial x \partial y} = 0 \qquad \text{Equation 3.33}$$

We can reduce Equation 3.32 to

$$\frac{\partial f_1}{\partial y} + \frac{\partial f_2}{\partial x} - \frac{\upsilon y}{R} = 0 \qquad \text{Equation 3.34}$$

Returning to w_0 we can write it in the form

$$w_0 = C_1x + C_2y + C_3 \qquad \text{Equation 3.35}$$

And separating and integrating Equation 3.34 we find

$$f_1 = \frac{vy^2}{2R} + C_4y + C_5 \qquad \text{Equation 3.36}$$

$$f_2 = -C_4x + C_6 \qquad \text{Equation 3.37}$$

Substituting back

$$u = -\frac{z^2}{2r} - C_1z - \frac{vx^2}{2R} + \frac{vy^2}{2R} + C_4y + C_5 \qquad \text{Equation 3.38}$$

$$v = -C_2z - v\frac{xy}{R} - C_4x + C_6 \qquad \text{Equation 3.39}$$

$$w = \frac{xz}{R} + C_1x + C_2y + C_3 \qquad \text{Equation 3.40}$$

We now need to develop a set of boundary conditions so we can eliminate or determine the above constants. From Figure 3-13, we chose an origin as shown with the distance *l,* in the *z*-direction between U_a and U_b and we can evaluate u at (0,0,*l*) and at (0,0,-*l)* which by symmetry are equal.

$$u(0,0,l) = u(0,0,-l) \qquad \text{Equation 3.41}$$

$$-\frac{l^2}{2r} - C_1l + C_5 = -\frac{l^2}{2r} + C_1l + C_5 \qquad \text{Equation 3.42}$$

This can only be possible if

$$C_1 = 0 \qquad \text{Equation 3.43}$$

Appling further boundary conditions

$$v(0,0,0) = 0 \qquad \text{Equation 3.44}$$

And since all other terms cancel out

$$C_6 = 0$$ Equation 3.45

In a similar manner, we can obtain C_3

$$w\ (0,0,0)=0$$ Equation 3.46

$$C_3 = 0$$ Equation 3.47

We see that

$$\frac{\partial v}{\partial z} = 0$$ Equation 3.48

$$\frac{\partial v}{\partial x} = 0$$ Equation 3.49

Leading to

$$C_2 = 0$$ Equation 3.50

$$C_4 = 0$$ Equation 3.51

leaving only C_5 to resolve. To do this we choose two points U_a and U_b as shown in Figure 3-13 with a Cartesian coordinate system (*x,y,z*) with its origin set at the center of the beam cross section.

$$U_b \Rightarrow u\left(-\frac{h}{2}, 0,0\right)$$ Equation 3.52

$$U_a \Rightarrow u\left(\frac{h}{2}, 0, -l\right)$$ Equation 3.53

Plugging back in and further reducing we obtain the difference between U_a and U_b and eliminate C_5

$$(u_b - u_a) = \frac{l^2}{2R} = \frac{Ml^2}{2EI} \qquad \text{Equation 3.54}$$

Rearranging, we have a relationship that can be used to determine the flexure stiffness based on the relative displacement of u_a and u_b

$$EI = \frac{ML^2}{2(u_b - u_a)} \qquad \text{Equation 3.55}$$

This relationship can now be used to evaluate the data taken from the four-point bending tests.

NORMALIZATION OF THE FLEXURE STIFFNESS

As discussed in Chapter Two, it is necessary to normalize the flexural stiffness to compare the predictions of the Gibson and Ashby continuum model to those obtained from a mechanics of solids analysis and to experimental results. Although the choice of normalization methods is somewhat arbitrary and does not influence the findings, we have chosen to normalize the data to the continuum flexure stiffness as discussed in Chapter Two.

RESULTS

We start by presenting results and observations from the SLS build process itself. Then we present the results of the testing from both the three-point and four-point testing of both the square-celled and hexagonal-celled samples. First, we address the square cell sample sets at low volume fractions, then the higher volume fraction samples. We label the four cases presented as square-thin, square-thick, hexagonal-thin, and hexagonal-thick. For each case we present first our predictions using the continuum model and from the mechanics of solids analysis, and then we present the experimental results of the three-point and four-point bending tests. The experimental results for the both the three-point and four-point bending tests were analyzed using 1) conventional beam calculations using the normalized flexure stiffness versus specimen-to-cell size ratio and 2)using the elasticity solution presented in the previous section.

GENERAL RESULTS REGARDING SAMPLES PRODUCED USING SELECTIVE LASER SINTERING

The dimensional tolerances of sample parts built with the SLS system was good-to-excellent. In Table 3-3 we present the data from the measurement of cross sectional area of the square samples. The target dimension was 20.00 mm x 20.00 mm and all of the samples exhibited about a two percent RMS error or less in the target dimensions.

Recalling that a set of solid parts were built in three orientations (in the *x-y* plane, built "on a corner" in the *x-y* plane and built in the *z*-axis plane) these samples were tested to determine their flexural stiffness. From the results of these tests we saw less than a two percent variation in flexural stiffness and thus we concluded that the stiffness of parts built using the SLS fabrication process is not dependent of build orientation.

Table 3-3: Square-celled honeycomb samples, the dimensional tolerance that were obtained, and the associated errors in the cross-sectional areas

Sample Number	Cross Section Size (target 20.00 x20.00 (mm x mm))	RMS error
Square #1	20.06 x 20.32	1.63%
Square #2	20.04 x 20.39	1.96%
Square #3	20.13 x 20.22	1.28%
Square #4	20.19 x 20.07	1.01%
Square #5	20.07 x 20.11	0.65%
Square #6	20.10 x 20.06	0.58%
Square #7	20.40 x 19.94	2.02%
Square #8	20.25 x 19.93	1.30%
Square #9	20.37 x 20.06	1.87%
Square #10	20.07 x 20.21	1.11%
Square #11	19.86 x 20.39	2.07%
Square #12	20.07 x 20.16	0.87%

THREE-POINT AND FOUR-POINT BENDING RESULTS FOR SQUARE-CELLED HONEYCOMBS: FIFTEEN PERCENT SOLID FRACTION

We start by presenting the normalized flexure stiffness as predicted by the Gibson and Ashby continuum model. This is shown in Figure 3-16 for the first set of samples, the square-cross section samples with the thinnest wall sections. Here we see the continuum model predicts no size effects and the normalized flexure stiffness is simply one for all values of *R*. Next, we present in Figure 3-17 the predictions results from the mechanics of solids model. Here we see that the normalized flexure stiffness is predicted to vary as a function of the specimen-to-cell size ratio with the flexure stiffness increasing to around 180% of the continuum value when the specimen-to-cell size ratio is one and dropping to a 120% of continuum stiffness at *R* equal four.

Figure 3-18 shows the first of the experimental data and compares the

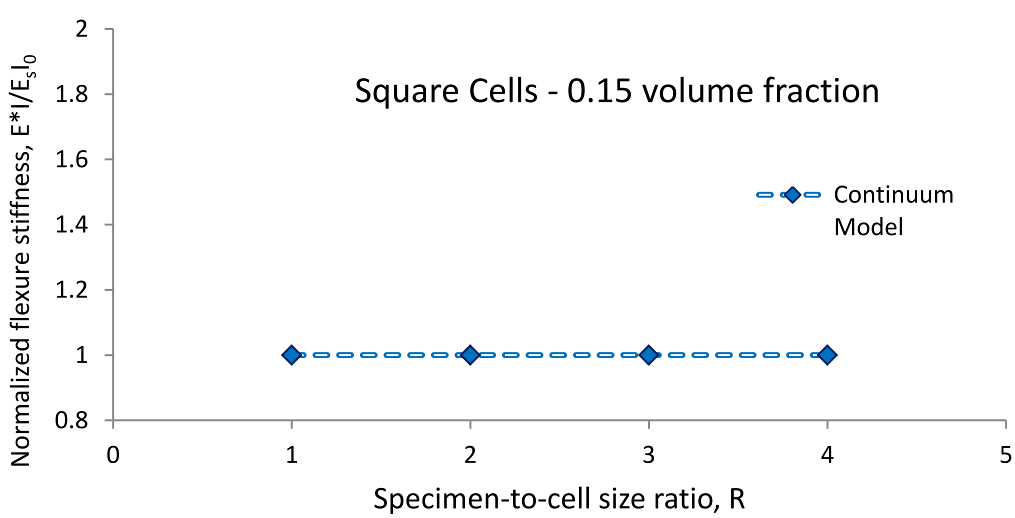

FIGURE 3-16: NORMALIZED FLEXURE STIFFNESS VERSUS SPECIMEN-TO-CELL SIZE RATIO: SQUARE-CELLS, 0.15 VOLUME FRACTION, AND CONTINUUM MODEL PREDICTIONS

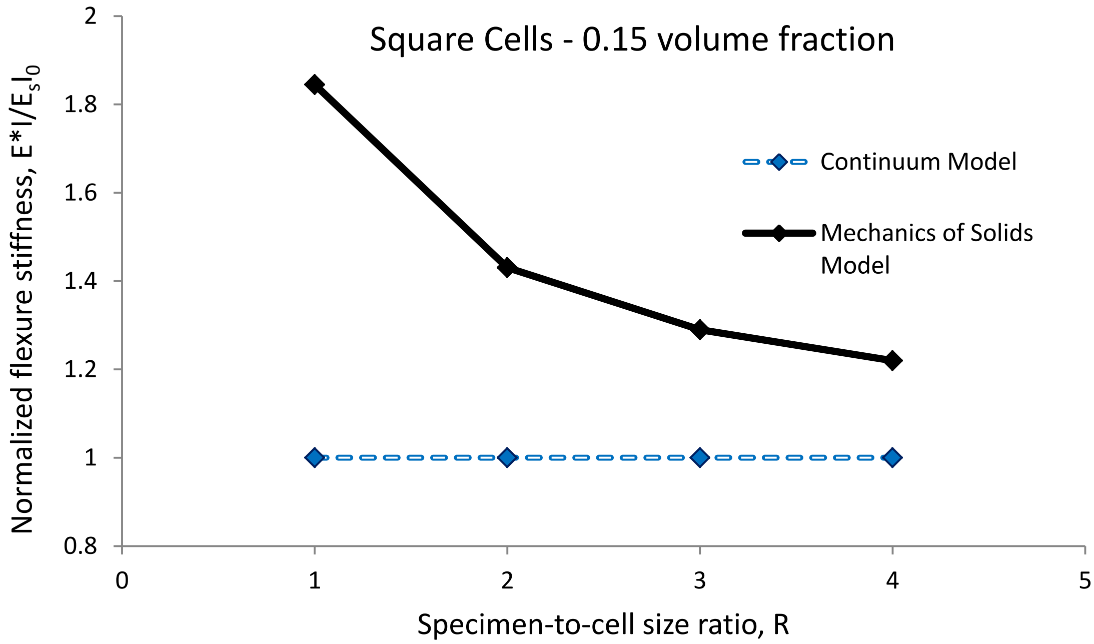

FIGURE 3-17: NORMALIZED FLEXURE STIFFNESS VERSUS SPECIMEN-TO-CELL SIZE RATIO: SQUARE-CELLS, 0.15 VOLUME FRACTION CONTINUUM MODEL AND MECHANICS OF SOLIDS PREDICTIONS

experiments to the models. The results reported on this graph only include two values of *R*, *R* = 1 and *R* =2. This is because of limitations of the SLS process because the wall thickness of the samples with specimen-to-cell size ratios of three and above where too thin to build on the system available. While only samples with specimen-to-cell size ratios of *R*=1 and *R*=2 were successfully built for these experiments, it worth noting that multiple samples of the *R*=1 and the *R*=2 samples were built and tested. We see that both of the data points for the samples tested in three-point loading lie below the predictions of the mechanics of solids model, and one of the points also does not agree with the continuum model .

Figure 3-19 and Figure 3-20 respectively present results of experimental four point bending tests, but with the same results analyzed using both the mechanics of solids approach (Equation 3.3) and the elasticity approach (Equation 3.55). The elasticity approach is based on the difference in the relative positions of two points on the beam when in four point bending. Those points are U_b and U_a as defined in Figure 3-13. From Figures 3-19 and 3-20 we see that the data for four-point bending agree equally well with the mechanics of solids model, whichever analysis method is used. Note that the four-point bending measurements analyzed using the elasticity solution resulted in a large error bar; this data can be considered equivalent. We will discuss our interpretation of these results a little later after the remainder of the results are presented, but at this point we note that by obtaining a valid elastic measurement, we are in effect verifying that the beam is bending to the curved shaped predicted by elasticity. Finally in Figure 3-21 we present all the modeled and experimentally data for the square sample set with fifteen volume percent solids.

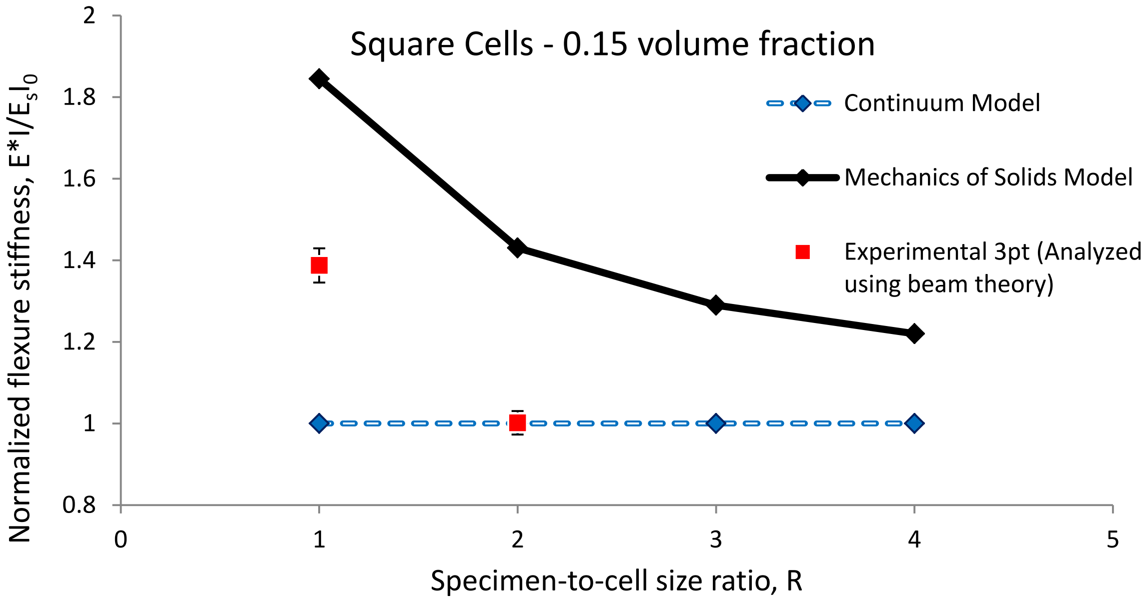

FIGURE 3-18: NORMALIZED FLEXURE STIFFNESS VERSUS SPECIMEN-TO-CELL SIZE RATIO: SQUARE-CELLED HONEYCOMBS, FIFTEEN VOLUME PERCENTAGE CONTINUUM MODEL PREDICTIONS, MECHANICS OF SOLIDS MODEL AND EXPERIMENTAL 3PT BEAM MEASUREMENTS ANALYZED USING BEAM THEORY

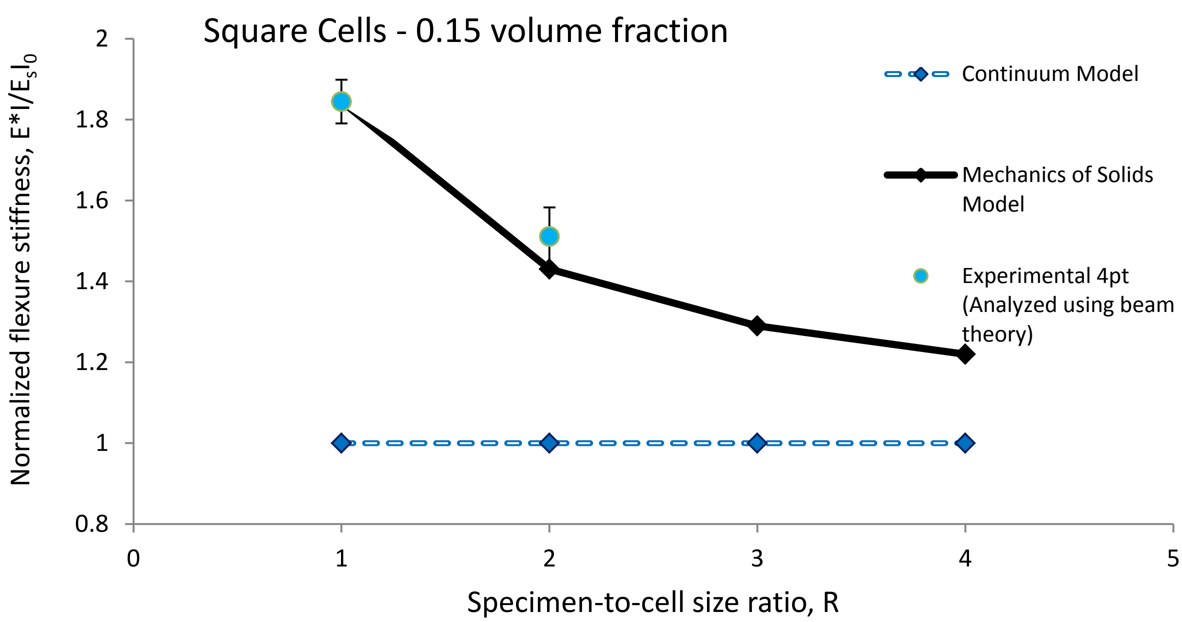

FIGURE 3-19: NORMALIZED FLEXURE STIFFNESS VERSUS SPECIMEN-TO-CELL SIZE RATIO: SQUARE-CELLED HONEYCOMBS, FIFTEEN VOLUME PERCENTAGE CONTINUUM MODEL PREDICTIONS, MECHANICS OF SOLIDS MODEL AND EXPERIMENTAL DATA TESTED IN 4PT BENDING AND ANLAYZED USING BEAM THEORY

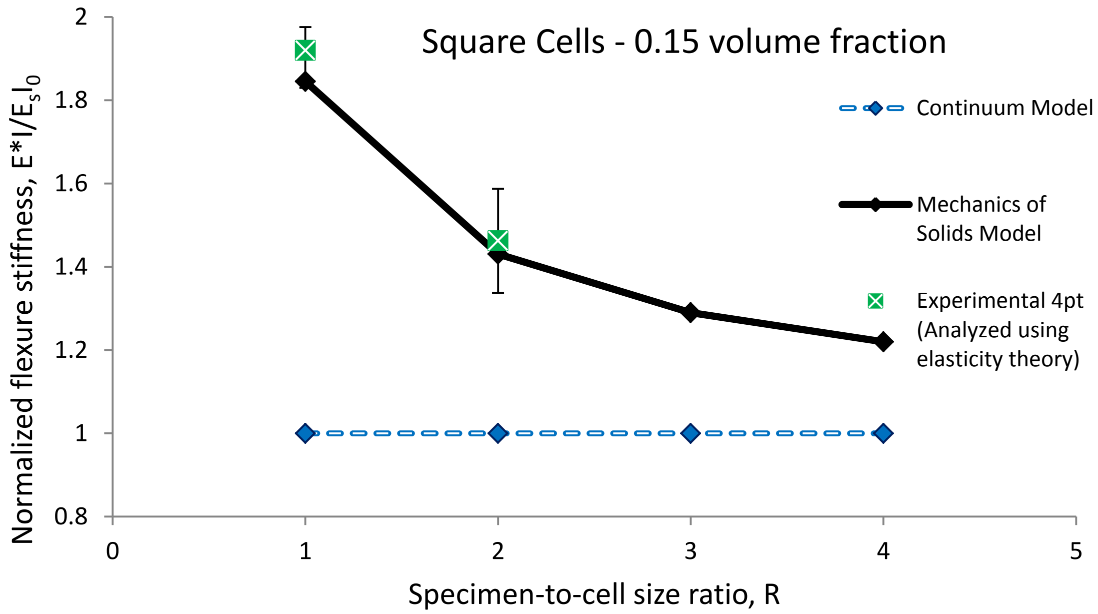

FIGURE 3-20 NORMALIZED FLEXURE STIFFNESS VERSUS SPECIMEN-TO-CELL SIZE RATIO: SQUARE-CELLED HONEYCOMBS, FIFTEEN VOLUME PERCENTAGE CONTINUUM MODEL PREDICTIONS, MECHANICS OF SOLIDS MODEL AND EXPERIMENTAL DATA TESTED IN 4PT BENDING AND ANLYZED USING ELASTICITY THEORY

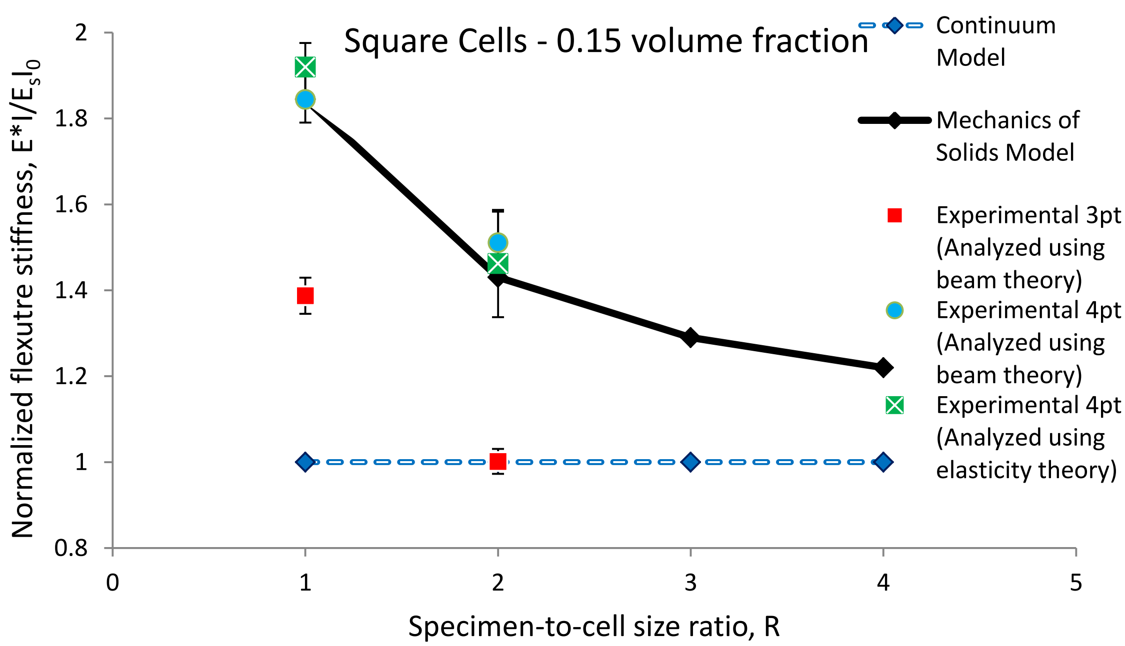

FIGURE 3-21 NORMALIZED FLEXURE STIFFNESS VERSES SPECIMEN-TO-CELL SIZE RATIO: SQUARE-CELLED HONEYCOMBS, FIFTEEN VOLUME PERCENTAGE ALL EXPERIMENTAL DATA AND MODEL PREDICTIONS

THREE-POINT AND FOUR-POINT BENDING RESULTS FOR SQUARE-CELLED HONEYCOMBS: TWENTY FIVE PERCENT VOLUME FRACTION

Starting in Figure 3-22 and continuing to Figure 3-27 we present experimental and predicted results for the square-celled thick-walled sample set. We start with the predictions from the Gibson and Ashby continuum model in Figure 3-22 and the predictions of the mechanics of solids model in Figure 3-23. Both models predict a result similar to what we described for the 0.15 volume fraction samples. As noted previously, the continuum model predicts that there is no size effect and the normalized flexure stiffness is again unity. Additionally the normalized flexure stiffness from the mechanics of solids model is predicted to vary as a function of the specimen-to-cell size ratio, with the flexure stiffness increasing to slightly less than the 180% of the continuum value when the specimen-to-cell size ratio is one and falling to about a 120% of continuum stiffness at a specimen-to-cell ratio of four.

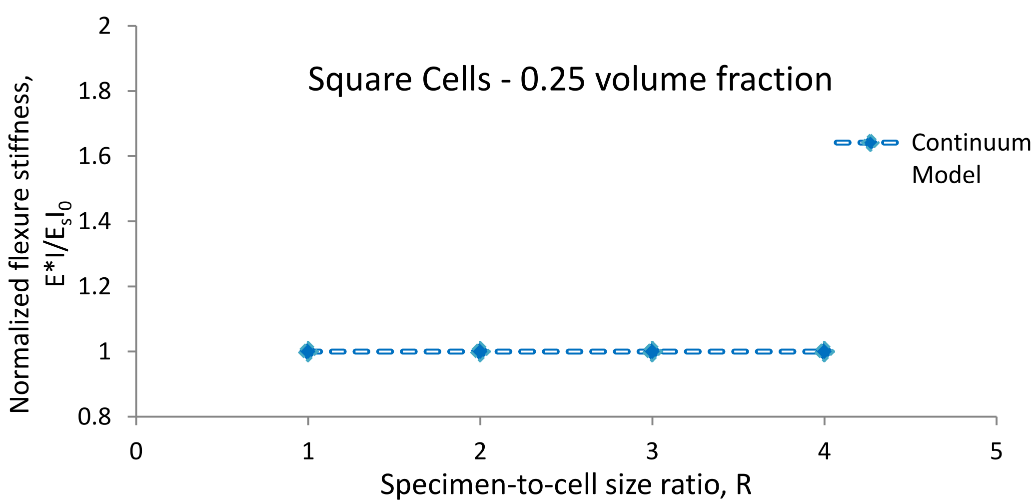

FIGURE 3-22: NORMALIZED FLEXURE STIFFNESS VERSUS SPECIMEN-TO-CELL SIZE RATIO: SQUARE-CELLED HONEYCOMBS, TWENTY FIVE PERCENT VOLUME FRACTION, CONTINUUM MODEL PREDICTIONS

Figure 3-24 shows the results of the three-point testing for the thicker walled square specimen set. This set of data, in contrast to the square celled 0.15 volume

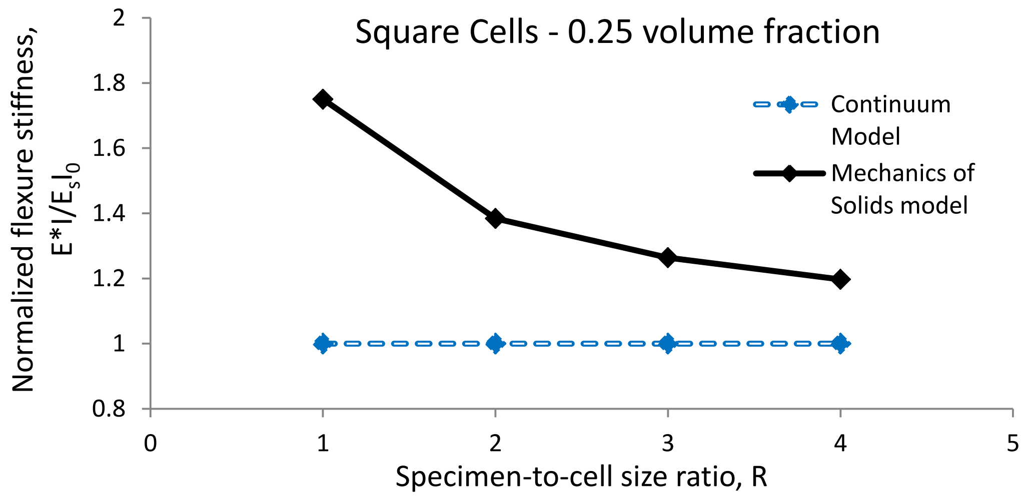

FIGURE 3-23 NORMALIZED FLEXURE STIFFNESS VERSUS SPECIMEN-TO-CELL SIZE RATIO: SQUARE-CELLED HONEYCOMBS, TWENTY FIVE VOLUME FRACTION, CONTINUUM MODEL AND MECHANICS OF SOLIDS PREDICTIONS

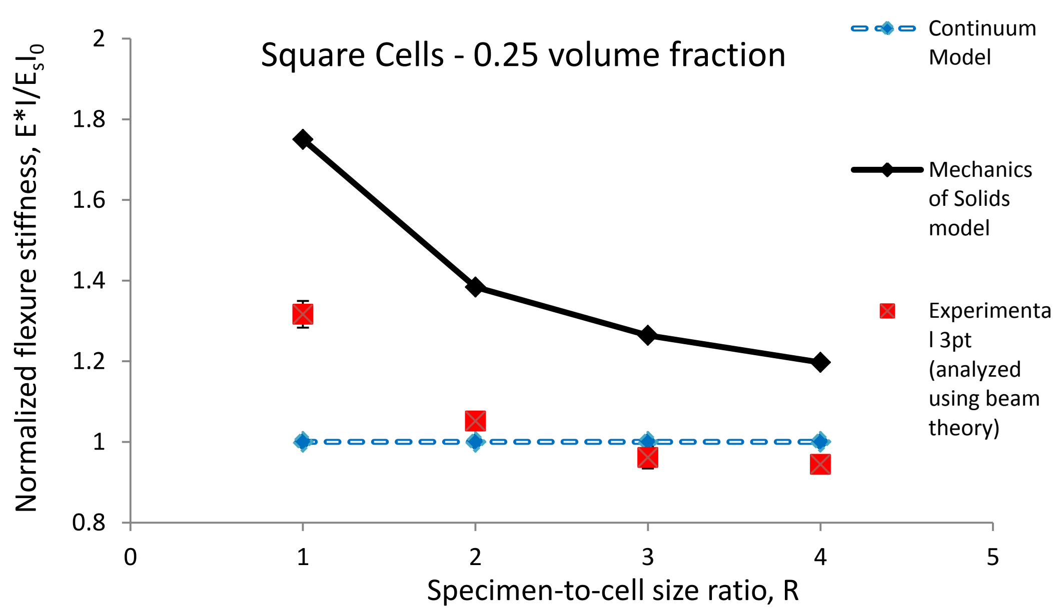

FIGURE 3-24 NORMALIZED FLEXURE STIFFNESS VERSUS SPECIMEN-TO-CELL SIZE RATIO: SQUARE-CELLED HONEYCOMBS, TWENTY FIVE VOLUME PERCENTAGE CONTINUUM MODEL PREDICTIONS, MECHANICS OF SOLIDS MODEL PREDICTIONS AND EXPERIMENTAL 3PT BEAM MEASUREMENTS ANALYZED USING BEAM THEORY

fraction samples included specimens with *R*= 1 to 4, thus giving us a more complete set of results. From the data in Figure 3-24 we see the measured flexure stiffness is less than predicted by the mechanics of solids model but has the same trend as the mechanics of solid predictions. Comparing the three-point bending data with the continuum model we see the measured flexure stiffness at *R*=1 is greater than the continuum prediction and decreases as the specimen-to-cell ratio increases. At *R*=3 and *R*=4 the measured flexure stiffness is less than the Gibson and Ashby continuum model prediction.

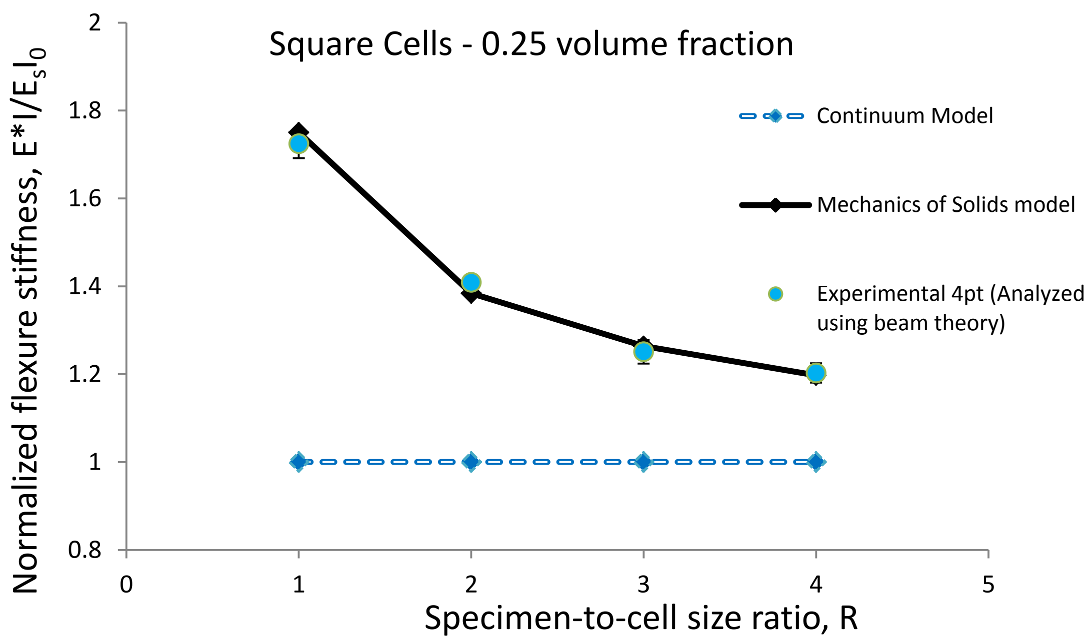

FIGURE 3-25 NORMALIZED FLEXURE STIFFNESS VERSUS SPECIMEN-TO-CELL SIZE RATIO: SQUARE-CELLED HONEYCOMBS, TWENTY FIVE VOLUME PERCENTAGE CONTINUUM MODEL PREDICTIONS, MECHANICS OF SOLIDS MODEL AND EXPERIMENTAL DATA TESTED IN 4PT BENDING AND ANALYZED USING ELASTICITY THEORY

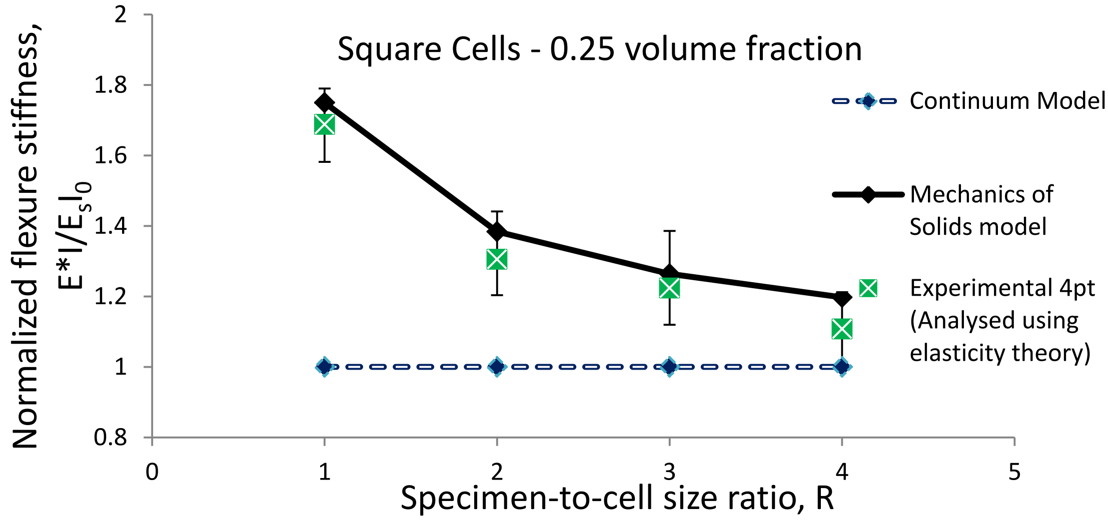

FIGURE 3-26: NORMALIZED FLEXURE STIFFNESS VERSUS SPECIMEN-TO-CELL SIZE RATIO: SQUARE-CELLED HONEYCOMBS, TWENTY FIVE VOLUME PERCENTAGE CONTINUUM MODEL PREDICTIONS, MECHANICS OF SOLIDS MODEL AND EXPERIMENTAL DATA TESTED IN 4PT BENDING AND ANALYZED USING ELASTICITY THEORY

Figure 3-25 and Figure 3-26 show the results of the four-point testing for the square-celled, 0.25 volume fraction sample set, first evaluated using the mechanics of solids model and then using the elasticity analysis. Both analysis methods resulted in a measured flexure that closely agrees with the predictions of the mechanics of solids model. The elasticity analysis of the experimental four-point data showed normalized flexure stiffness slightly less the mechanics of solid predictions, but again both analysis methods yield good agreement with the mechanics of solids model predictions. Finally in Figure 3-27 we present all of the predictions and experimental data for the square sample set with twenty-five volume percent.

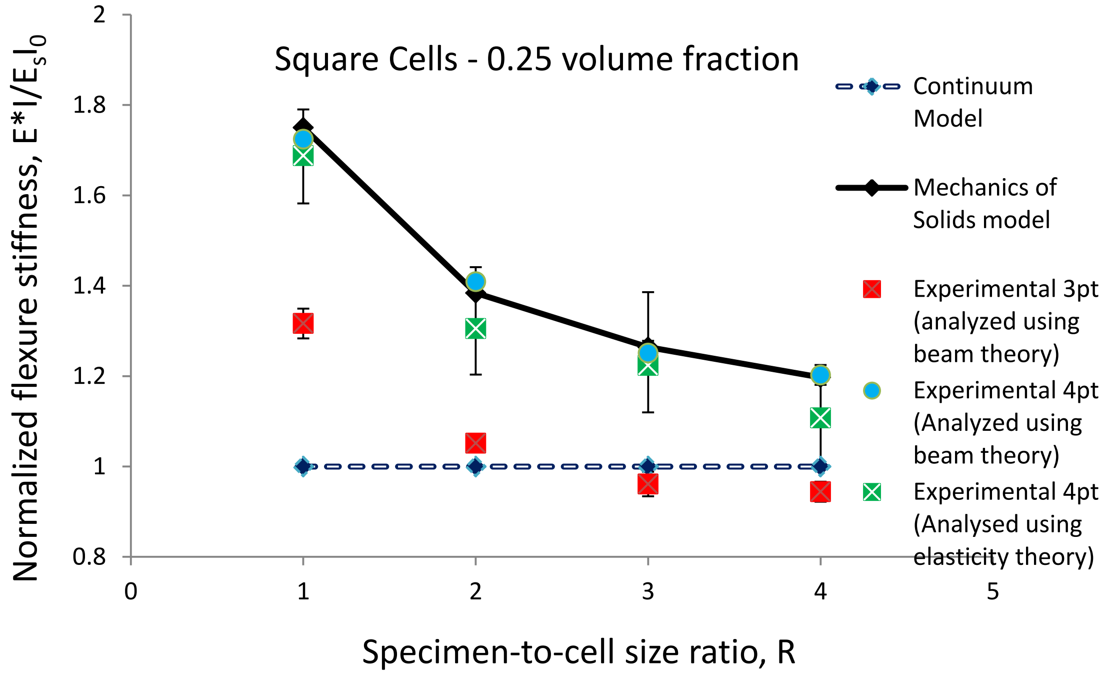

FIGURE 3-27 NORMALIZED FLEXURE STIFFNESS VERSES SPECIMEN-TO-CELL SIZE RATIO: SQUARE-CELLED HONEYCOMBS, TWENTYFIVE VOLUME PERCENTAGE ALL EXPERIMENTAL DATA AND MODEL PREDICTIONS

THREE-POINT AND FOUR-POINT BENDING RESULTS FOR HEXAGONAL-CELLED HONEYCOMBS: THIN WALLED SAMPLES

We next present the results from testing of the thin walled samples with a hexagonal cell structure, keeping the cell size constant and increasing the specimen size to vary the specimen-to-cell size ratio. We present in Figure 3-28 and Figure 3-29 the predictions of the continuum models and the mechanics of solids model. The pattern in the data is similar to what we observed in the corresponding figures for the square-celled sample sets. The continuum model predicts no size effect and the mechanics of solids model predicts an increase in stiffness for small specimen-to-cell size ratios with that effect decreasing with increasing *R*. In Figure 3-30 we see the results of the three-point testing for the thinner walled hexagonal specimen set. Again we report the

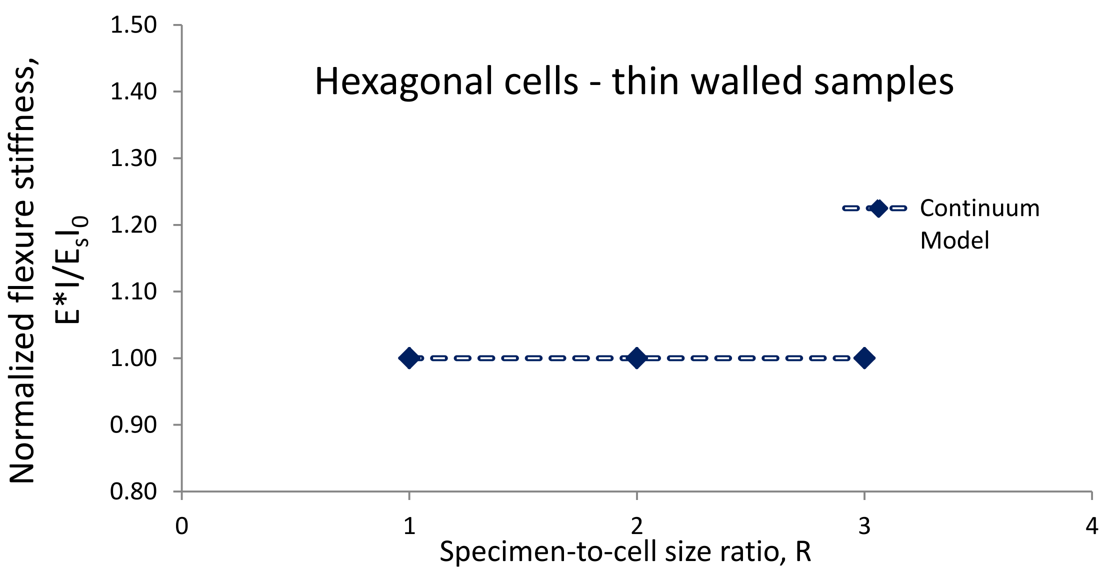

FIGURE 3-28: NORMALIZED FLEXURE STIFFNESS VERSUS SPECIMEN-TO-CELL SIZE RATIO: HEXAGONAL-CELLED HONEYCOMBS, THIN WALLED SAMPLES, CONTINUUM MODEL PREDICTIONS

measured normalized flexure stiffness for the three point data analyzed using Equation 3.1. We see the measured flexure stiffness is significantly lower than that predicted by the mechanics of solids model. The trend in the measured flexure stiffness appears to be similar to that predicted by the mechanics of solids model, just offset to lower values of stiffness. Comparing the three-point experimental data to the continuum prediction for the *R*=1 case, the measured value of the experimentally measured flexure stiffness is

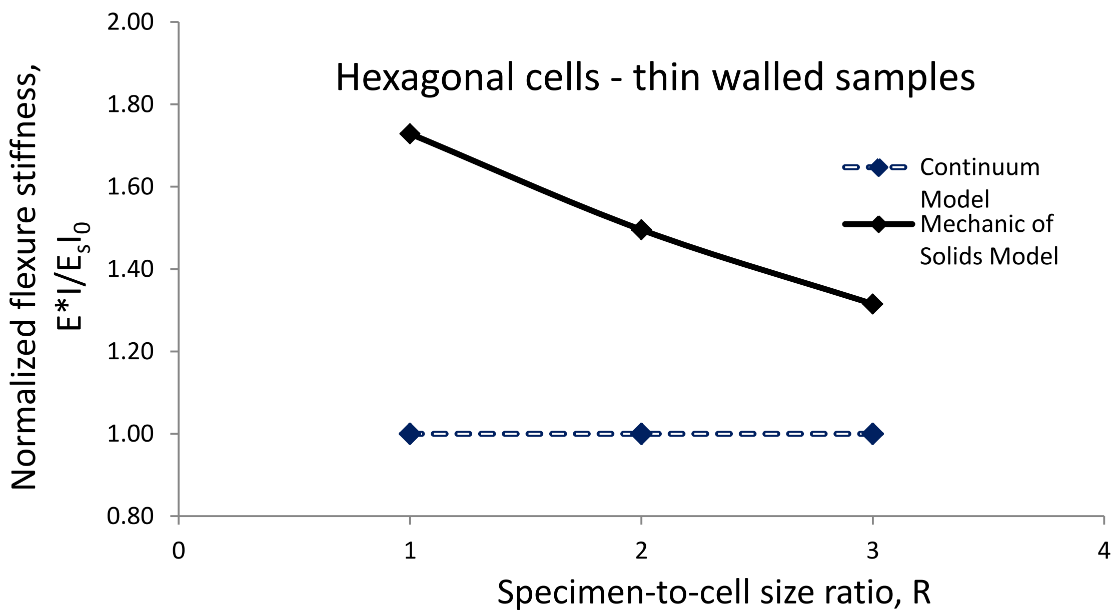

FIGURE 3-29: NORMALIZED FLEXURE STIFFNESS VERSUS SPECIMEN-TO-CELL SIZE RATIO: HEXAGONAL-CELLED HONEYCOMBS, THIN WALLED SAMPLES, CONTINUUM MODEL AND MECHANICS OF SOLIDS PREDICTIONS

slightly higher. For *R*=2 and above the measured flexure stiffness decreases and drops below the continuum model predictions.

In Figure 3-31 we present the results of the experimental four-point data analyzed using beam theory. Here we see a different result from that found for the square-celled specimens. The measured normalized flexure stiffness is less than the

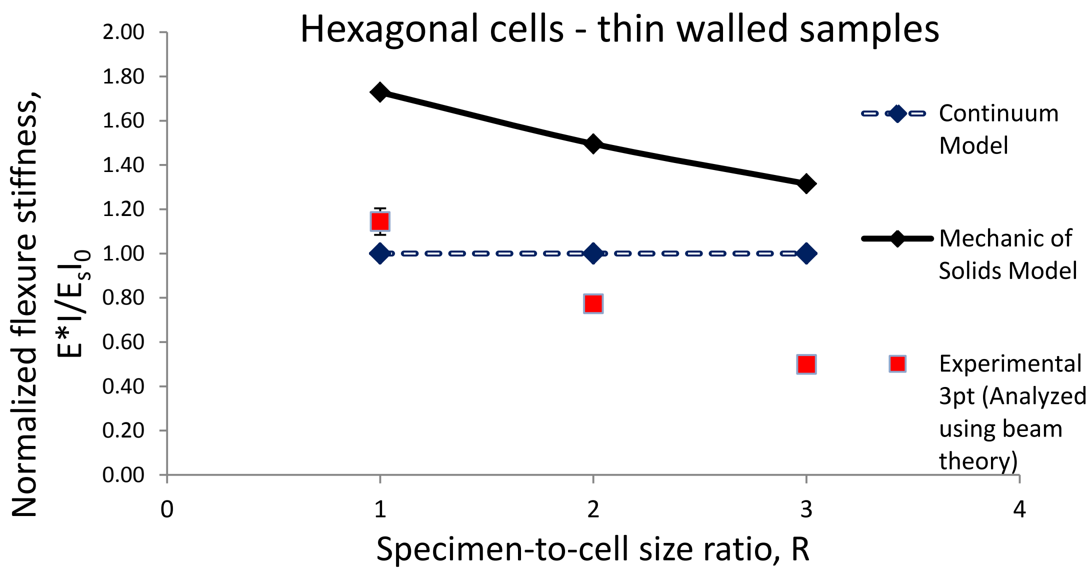

FIGURE 3-30: NORMALIZED FLEXURE STIFFNESS VERSUS SPECIMEN-TO-CELL SIZE RATIO: HEXAGONAL-CELLED HONEYCOMBS, THIN WALLED SAMPLES, CONTINUUM MODEL PREDICTIONS, MECHANICS OF SOLIDS PREDICTIONS AND EXPERIMENTAL 3PT BEAM MEASUREMENTS ANALYZED USING BEAM THEORY

predictions of the mechanics of solids model, again with a general trend similar to the mechanics of solids model yet offset in a similar manner to what we observed in the three-point bending of the square-celled samples. There is no clear relationship between the four point data using the beam analysis and the continuum predictions.

In Figure 3-32 we present the same four-point data set but now analyzed using the elasticity approach. Valid elasticity calculations were obtained only for R=1 specimen-to-cell ratio hexagonal sample. The data from the hexagonal samples with specimen-to-cell size ratios above one had excessive localized deformation so no valid analysis was possible. However the data for the R=1 specimen-to-cell size ratio did yield a result that matched the mechanics of solids model. Finally in Figure 3-33 we present all the predicted and experimental data for the thin walled regular hexagonal sample set

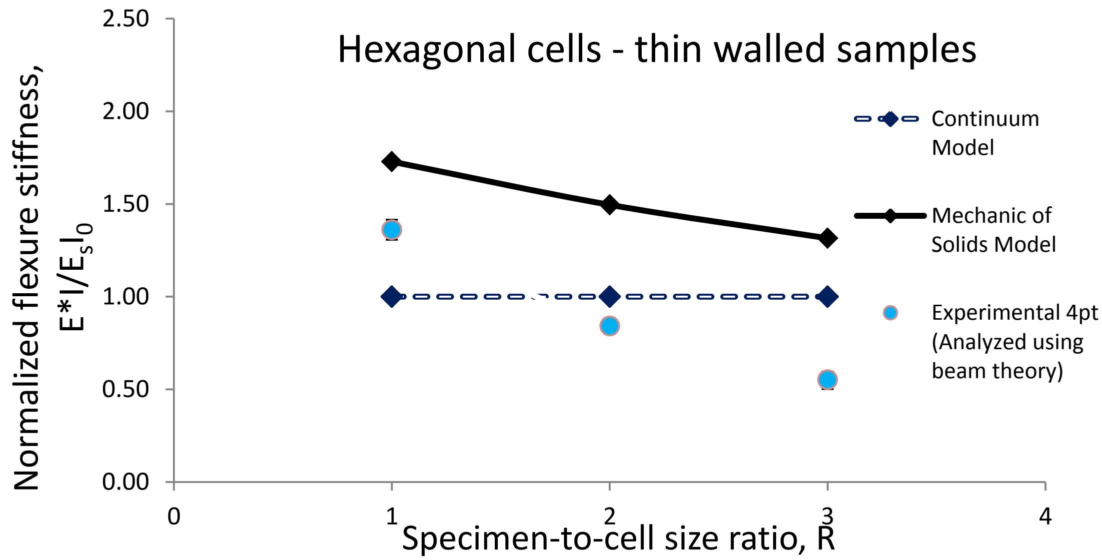

FIGURE 3-31: NORMALIZED FLEXURE STIFFNESS VERSUS SPECIMEN-TO-CELL SIZE RATIO: HEXAGONAL-CELLED HONEYCOMBS, THIN WALLED SAMPLES, CONTINUUM MODEL PREDICTIONS, MECHANICS OF SOLIDS PREDICTIONS AND EXPERIMENTAL 4PT BEAM MEASUREMENTS ANALYZED USING BEAM THEORY

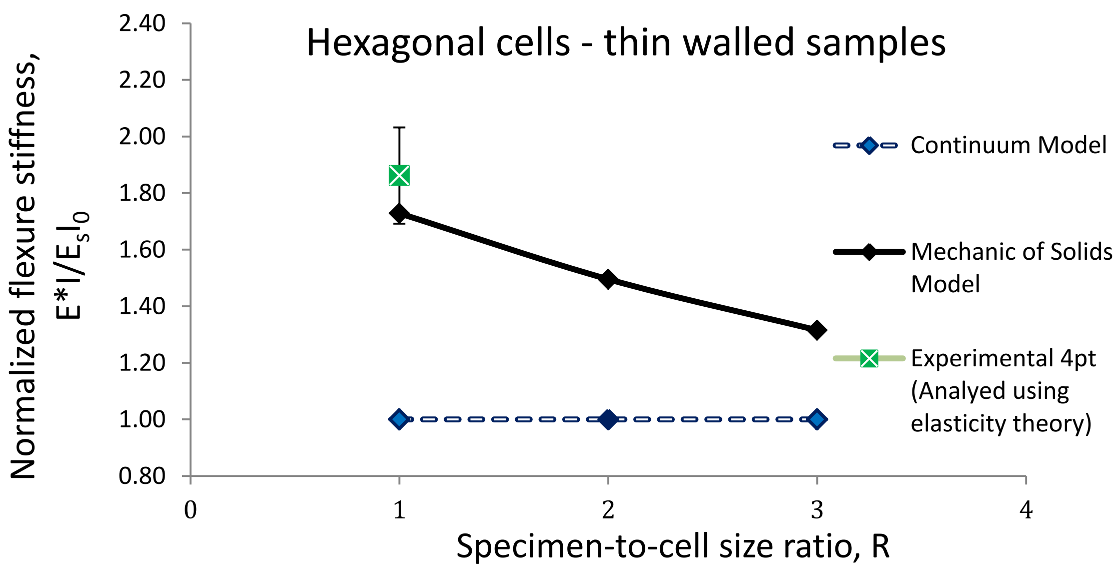

FIGURE 3-32: NORMALIZED FLEXURE STIFFNESS VERSUS SPECIMEN-TO-CELL SIZE RATIO: HEXAGONAL-CELLED HONEYCOMBS, THIN WALLED SAMPLES, CONTINUUM MODEL PREDICTIONS, MECHANICS OF SOLIDS PREDICTIONS AND EXPERIMENTAL 4PT BEAM MEASUREMENTS ANALYZED USING ELASTICITY THEORY

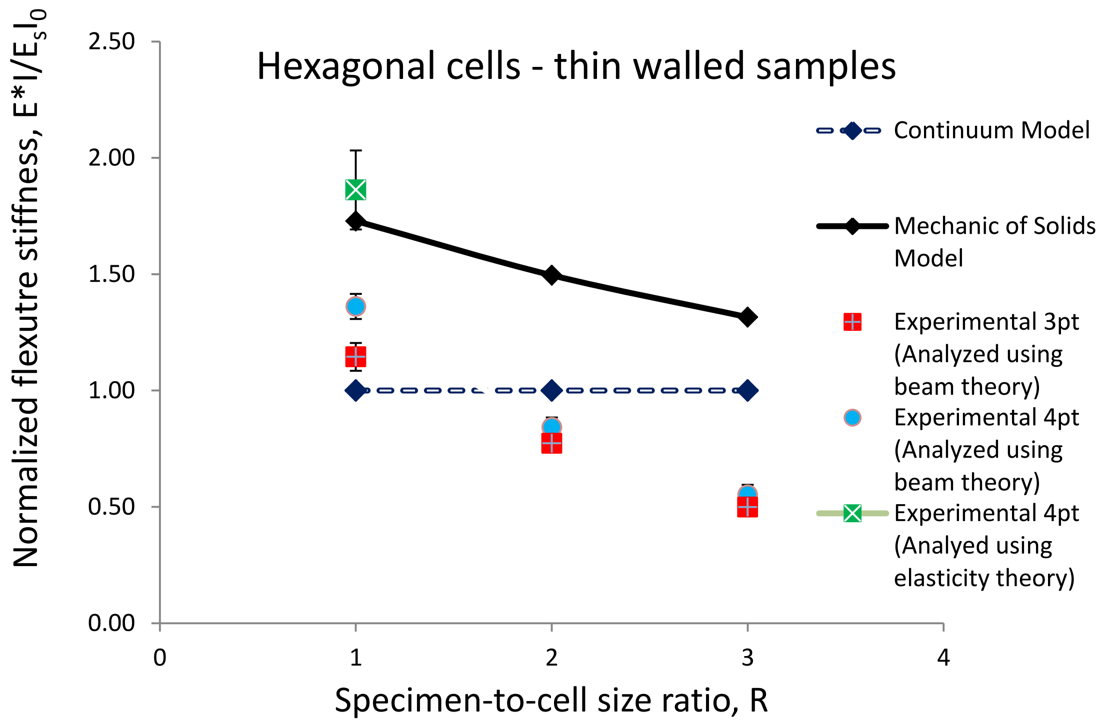

FIGURE 3-33 NORMALIZED FLEXURE STIFFNESS VERSUS SPECIMEN-TO-CELL SIZE RATIO: HEXAGONAL-CELLED HONEYCOMBS SQUARE-CELLED HONEYCOMBS, THIN WALLED SAMPLES, ALL EXPERIMENTAL DATA AND MODEL PREDICTIONS

THREE-POINT AND FOUR-POINT BENDING RESULTS FOR HEXAGONAL-CELLED HONEYCOMBS: THICK WALLED SAMPLES

Finally, we present the results from testing of the thick walled hexagonal samples. We present in Figure 3-34 and Figure 3-35 the predictions of the continuum models and the mechanics of solids model. The pattern in the data we see here is similar to what we observed in the preceding sample sets. The continuum model predicts no size effect and the mechanics of solids again shows increased flexural stiffness.

In Figure 3-36 we see the results of the three-point testing for the thicker walled hexagonal specimen set. Comparing the three-point data to the continuum model predictions, there is poor agreement. From the measured flexure stiffness for the

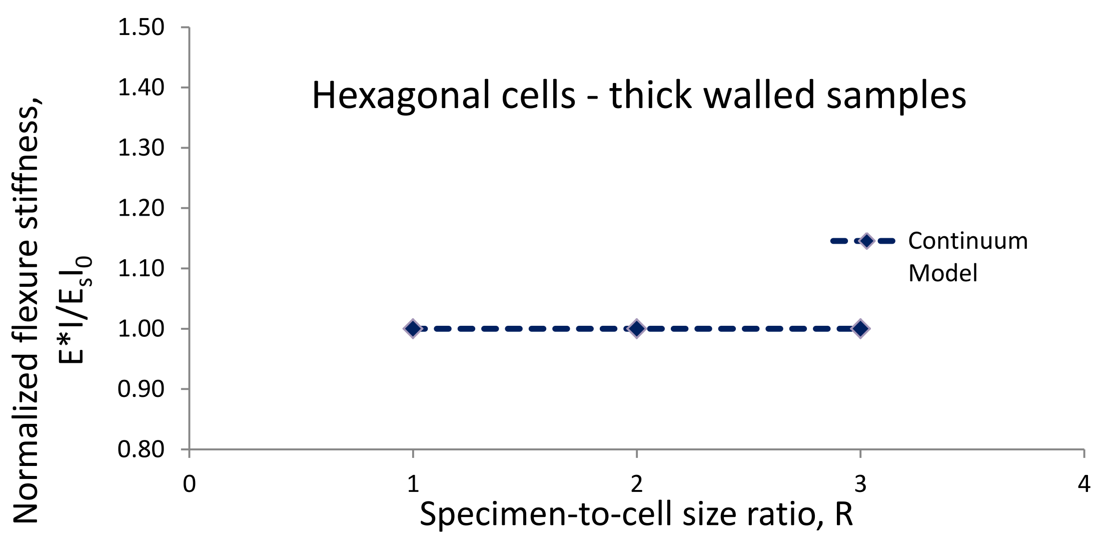

FIGURE 3-34: NORMALIZED FLEXURE STIFFNESS VERSUS SPECIMEN-TO-CELL SIZE RATIO: HEXAGONAL-CELLED HONEYCOMBS, THICK WALLED SAMPLES, CONTINUUM MODEL PREDICTIONS

three-point data analyzed using Equation 3.1, we see the measured flexure stiffness is lower than that predicted by the mechanics of solids model. The trend in the measured flexure stiffness is similar but offset relative to the slope of the mechanics of solids model predictions.

In Figure 3-37 we present the results of the experimental four-point data analyzed using beam theory. Here we again observe a different result for the regular hexagonal honeycombs than we saw for the square-celled honeycombs. The measured flexure stiffness of the regular hexagonal-celled honeycombs is less than the predictions of the mechanics of solids model, again with a general trend similar to the trend of the mechanics of solids model yet offset in similar manner to what we observed in the three-point bending of the square celled samples. There is again poor agreement

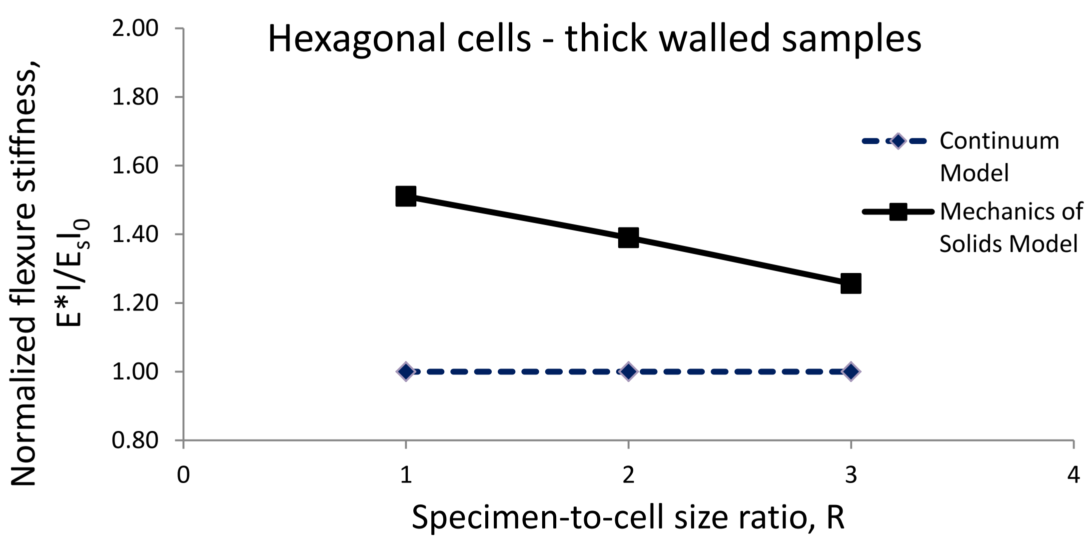

FIGURE 3-35: NORMALIZED FLEXURE STIFFNESS VERSUS SPECIMEN-TO-CELL SIZE RATIO: HEXAGONAL-CELLED HONEYCOMBS, THICK WALLED SAMPLES, CONTINUUM MODEL AND MECHANICS OF SOLIDS PREDICTIONS

between the experimental data measured in four-point loading and the continuum predictions.

In Figure 3-38 we show the same four-point data set but analyzed using the elasticity approach and the crosshead displacement and the center-point displacements. As was the case for the thin walled hexagonal samples, valid calculations were obtained only for the *R*=1 specimen.. The other samples with specimen-to-cell size ratios above one had excessive localized deformation so no valid analysis was possible. However the data for the *R*=1 specimen-to-cell size ratio did yield a result that matched the mechanics of solids model within the calculated error. Finally in Figure 3-39 we present all the model predictions and experimental data for the thick walled regular hexagonal sample set.

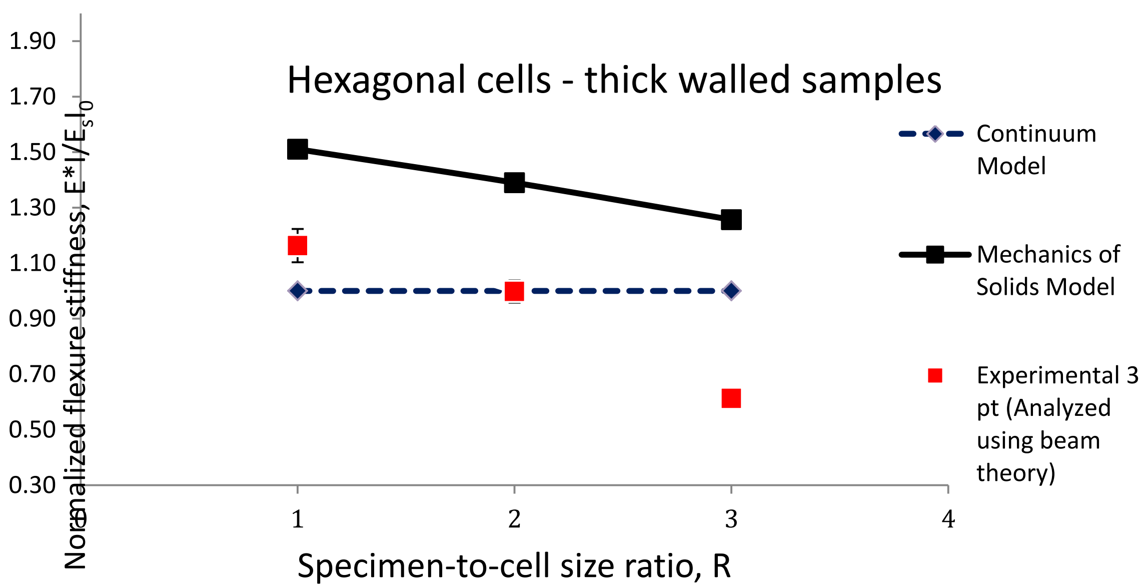

FIGURE 3-36: NORMALIZED FLEXURE STIFFNESS VERSUS SPECIMEN-TO-CELL SIZE RATIO: HEXAGONAL-CELLED HONEYCOMBS, THICK WALLED SAMPLES, CONTINUUM MODEL PREDICTIONS, MECHANICS OF SOLIDS PREDICTIONS AND EXPERIMENTAL 3PT BEAM MEASUREMENTS ANALYZED USING BEAM THEORY

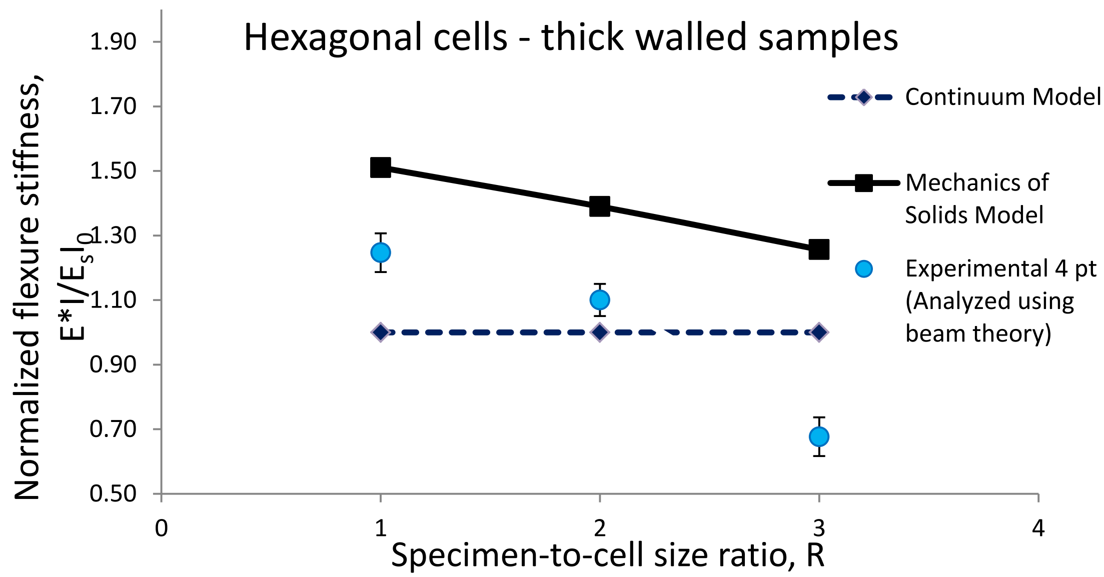

FIGURE 3-37: NORMALIZED FLEXURE STIFFNESS VERSUS SPECIMEN-TO-CELL SIZE RATIO: HEXAGONAL-CELLED HONEYCOMBS, THICK WALLED SAMPLES, CONTINUUM MODEL PREDICTIONS, MECHANICS OF SOLIDS PREDICTIONS AND EXPERIMENTAL 4PT BEAM MEASUREMENTS ANALYZED USING BEAM THEORY

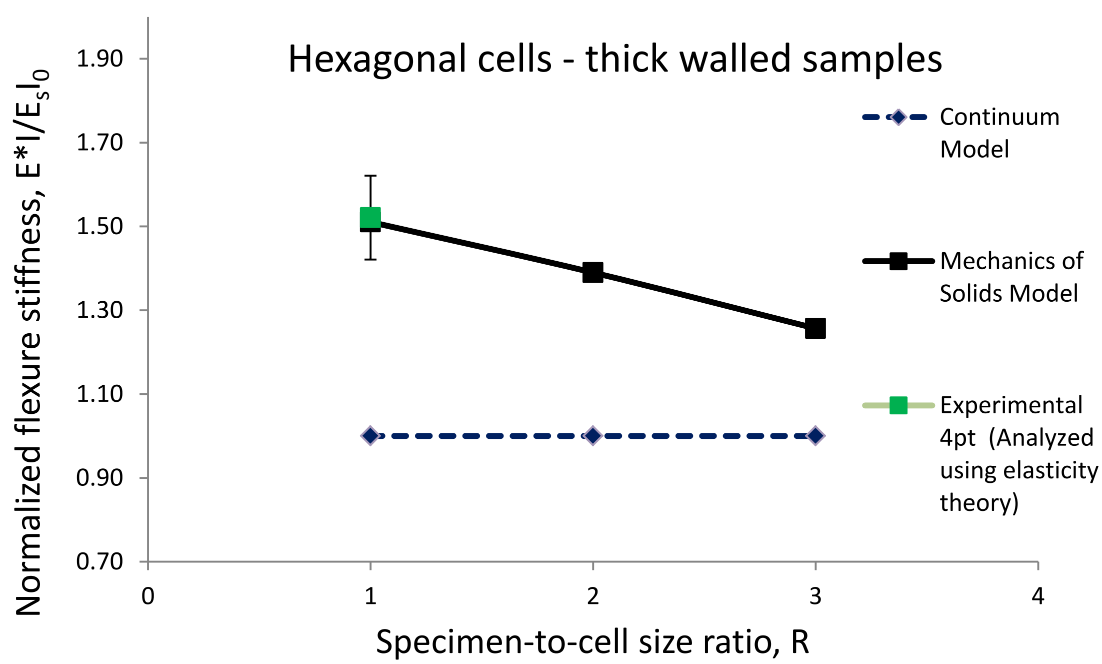

FIGURE3-38: NORMALIZED FLEXURE STIFFNESS VERSUS SPECIMEN-TO-CELL SIZE RATIO: HEXAGONAL-CELLED HONEYCOMBS, THIN WALLED SAMPLES, CONTINUUM MODEL PREDICTIONS, MECHANICS OF SOLIDS PREDICTIONS AND EXPERIMENTAL 4PT BEAM MEASUREMENTS ANALYZED USING ELASTICITY THEORY

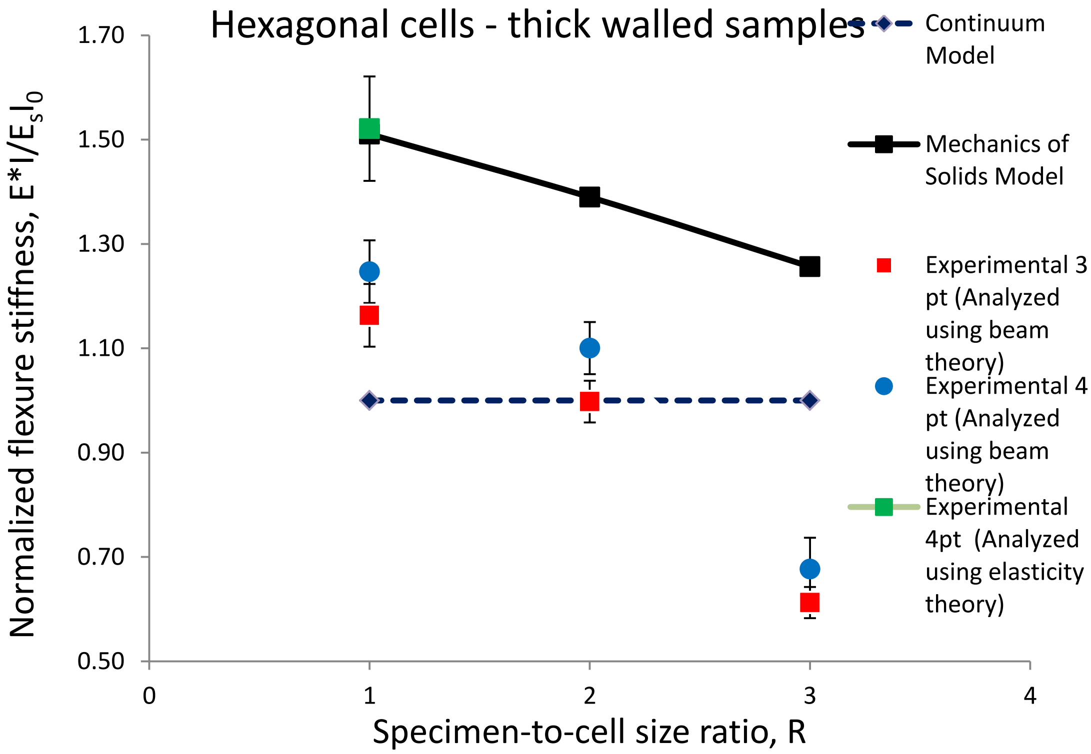

FIGURE 3-39 NORMALIZED FLEXURE STIFFNESS VERSUS SPECIMEN-TO-CELL SIZE RATIO HEXAGONAL-CELLED HONEYCOMBS, THICK WALLED SAMPLES, ALL EXPERIMENTAL DATA AND MODEL PREDICTIONS

Chapter 4: Discussion of experimental results

INTRODUCTION

The goal of this chapter is to determine under what conditions appropriate models can be used to predict the flexural response of honeycomb structures loaded in out-of-plane bending. We do this by further comparing the predictions of our models to our experimental results. Our predictions in Chapter Two showed that the continuum model and the mechanics of solids model converged for high *R* values. For example, as shown in Figure 2-8, for the square celled, single-walled, honeycombs, for *R* values greater than 20, the predictions agree within five percent or less. Thus for high values of *R*, we have shown both models are equally valid.

In the case of the samples sets tested in Chapter Three, the *R* values where less than five and none showed good agreement with the predictions of the continuum model. The mechanic of solids model predictions were shown to be are a much better fit to the experimental data than the continuum model. In the section that follows we proceed to examine under what conditions our testing methods agree with the mechanics of solids predictions and then, attempt to analyze and explain the cases where the testing does not agree with the predictions.

Specimen length-to-height ratio

The discussion of these results is complicated by the two different sample set geometries and the different construction rules that are required to build the sample sets. Recall that the square-celled sample set was designed with a constant specimen size and a varying cell size while the hexagonal-celled sample set was designed with a fixed cell size and with a varying specimen size. The practical implications of this is that the square-celled samples all have the same height while the height of the hexagonal-celled samples increases as the specimen-to-cell size ratio increases. Since both our testing methods, three-point and four-point, flexure were conducted with a fixed bending length, as shown in Figures 3.9 and 3.11, this resulted in length-to-height ratios that remained constant (7.5) for the square-celled honeycombs and increased with increasing specimen-to-cell size ratio for the hexagonal-celled honeycombs. The length-to-height ratio of hexagonal-celled samples was 10.5 for R=1, 9.8 for R=2 and 5.5 for R=3. For the samples with larger specimen-to-cell size ratios, R=4, 5 and 6, the length-to-height ratio of these samples was so low that the experimental data from testing these samples was not used because the slender beam assumption was violated. This difference in the sample sets and the nature of the results themselves dictate that we look at each of the three experimental methods in combination with the two sample architectures.

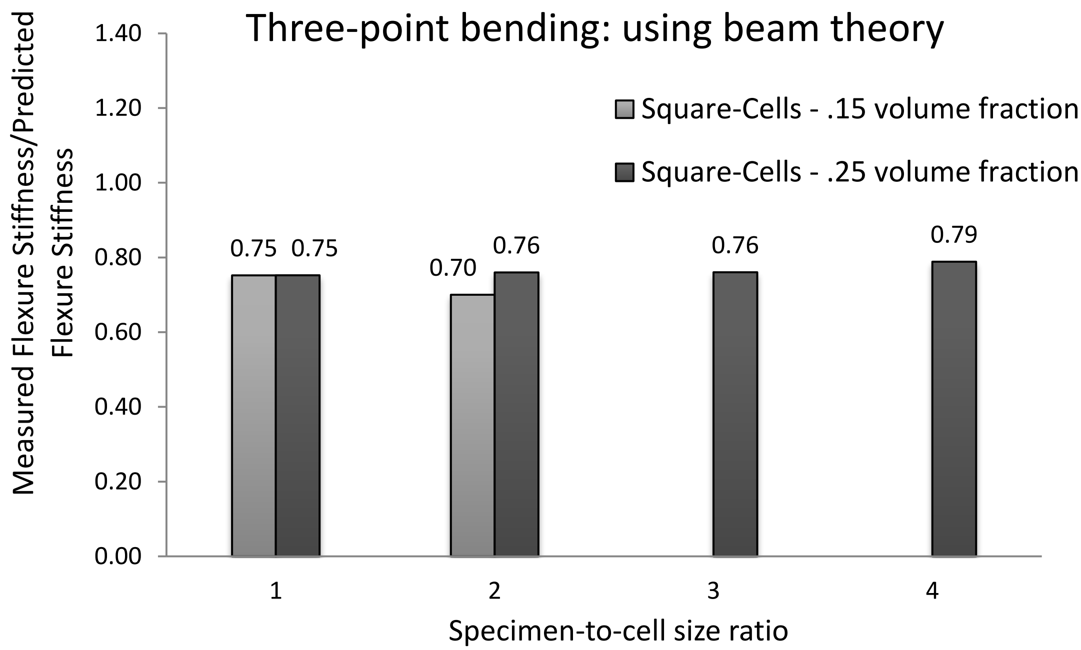

FIGURE 4-1 : THREE-POINT BENDING, SQUARE-CELLED SAMPLES, MEASURED FLEXURE STIFFNESS/PREDICTED FLEXURE STIFFNESS VERSUS SPECIMEN-TO-CELL SIZE RATIO

EXPERIMENTAL RESULTS COMPARED TO MECHANICS OF SOLIDS PREDICTIONS

Figures 4-1 and 4-2 show the ratio of the measured flexure stiffness to the predicted flexural stiffness based on a mechanics of solids model for the three-point bending of the square-celled and hexagonal-celled samples, respectively. In Figure 4-1 we see than the measured stiffnesses for all of the square-celled samples are about 75% or three-quarters of the predicted flexure stiffnesses. Figure 4-2 shows that the measured stiffnesses for the hexagonal-celled are also lower than the mechanics of solids predictions. However, for the hexagonal-celled specimens the ratio of measured-to-predicted stiffness decreases as the specimen-to-cell size ratio increases. The ratio of measured-to-predicted stiffness is also lower for the thin walled sample set compared to the thick walled set.

Figures 4-3 and 4-4 present the same results for the four-point bending data analyzed using beam theory, first for the square-cells and then in Figure 4-4 for the hexagonal-cells. Figure 4-3 shows generally good agreement between the predicted values and the experimentally obtained values for all values of the specimen-to-cell size ratios, while we see in Figure 4-4 the measured stiffness for the hexagonal-celled honeycombs is again below the predictions and decreases with increasing specimen-to-cell size ratio.

From these results we see that only the four-point bending of the square-celled

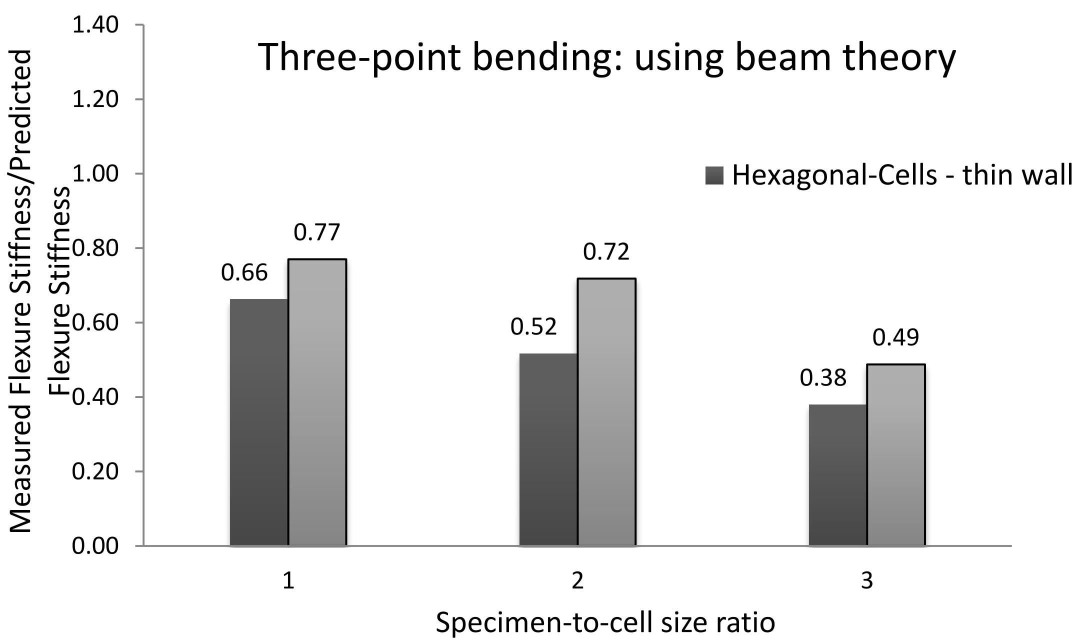

FIGURE 4-2: THREE-POINT BENDING, HEXAGONAL-CELLED SAMPLES, MEASURED FLEXURE STIFFNESS/PREDICTED FLEXURE STIFFNESS VERSUS SPECIMEN-TO-CELL SIZE RATIO

samples, with a height-to-length ratio of 7.5 resulted in a measured stiffness consistent with the mechanics of solids predictions. The measured stiffnesses of the hexagonal-celled samples, which have height-to-length ratios both above and below the value for the square-celled samples, were not consistent with the mechanics of solids predictions. This strongly suggests that the minimum length-to-height ratio needed to obtain agreement between the measurement and model is different for the square-celled samples and the hexagonal-celled samples, with the hexagonal-celled samples requiring a larger length-to-height ratios. Alternatively there could be additional effects that we have not accounted for which are more significant in the hexagonal-celled samples than in the square-celled samples.

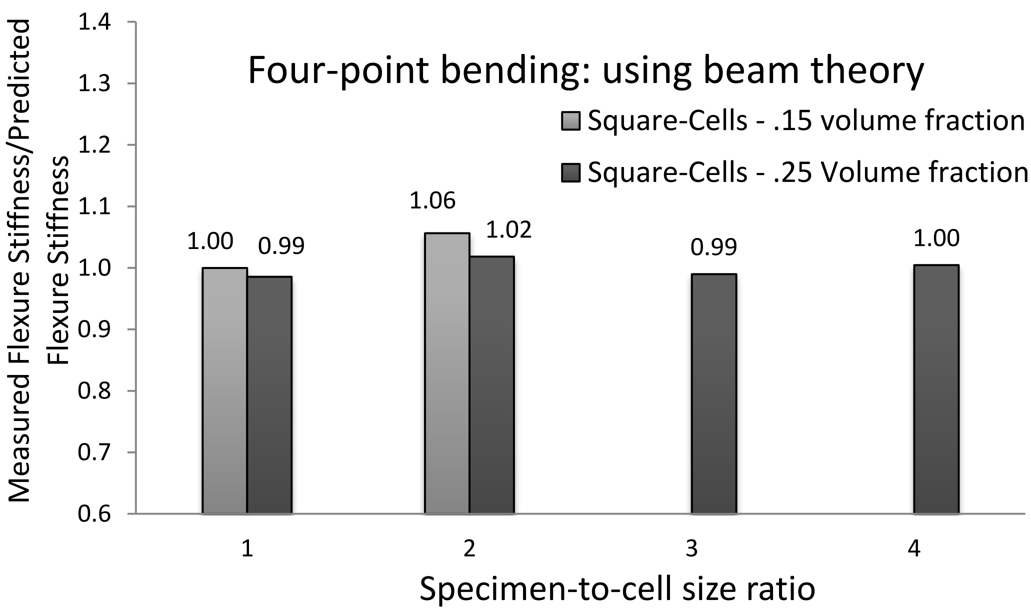

FIGURE 4-3- FOUR-POINT BENDING – EVALUATED USING BEAM THEORY, SQUARE-CELLED SAMPLES, MEASURED FLEXURE STIFFNESS/PREDICTED FLEXURE STIFFNESS VERSUS SPECIMEN-TO-CELL SIZE RATIO

We look to the results of the four-point bending tests that were analyzed using the elasticity analysis for more insight into this issue. When we examine the four-point elasticity data we go from relying on a single point to determine the displacement of the beam as it is being bent to using two points of measurement along the beam. It is the difference between these two points that are used to evaluate the flexure stiffness as explained in Chapter Three.

In Figure 4-5 we present the flexure stiffness, again normalized to the mechanics of solid predicted flexure stiffness, for the square-celled four-point data, and analyzed using the elasticity theory. We see here good agreement between the predictions and measured values, like we saw for the square-celled four-point bending data analyzed using conventional beam theory that utilizes only a single displacement point. In Figure 4-6 the normalized flexure stiffness for the hexagonal-celled four-point bending data analyzed using the elasticity solution is presented. Here we were only able to report a value for the sample with the specimen-to-cell size ratio of R=1. Samples with larger values of R did not yield a meaningful result. The reasons for this will be discussed in the section that follows.

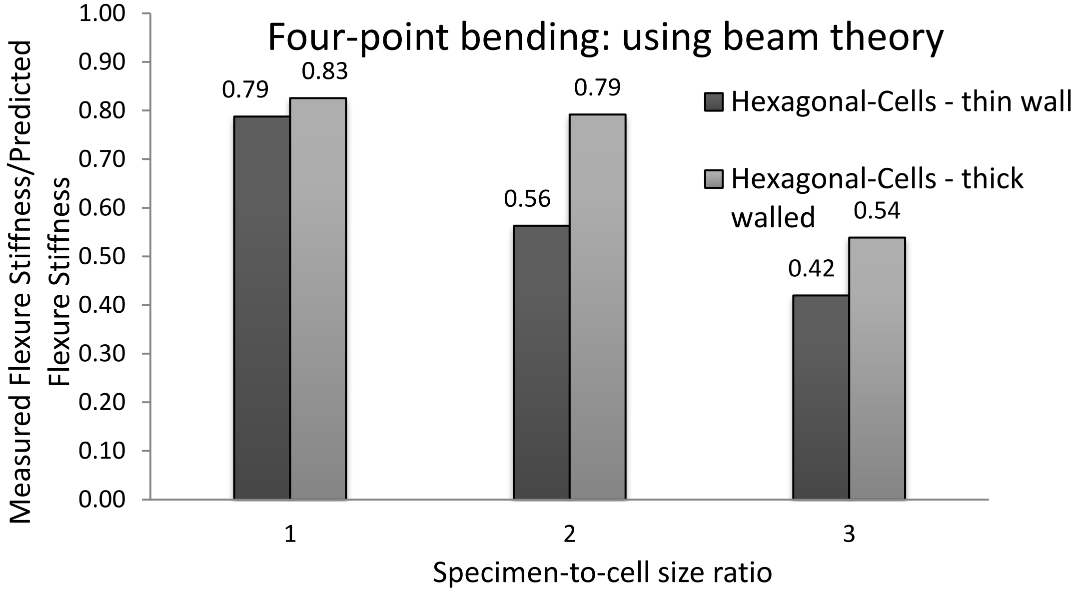

FIGURE 4-4: FOUR-POINT BENDING – EVALUATED USING BEAM THEORY, HEXAGONAL-CELLED SAMPLES, MEASURED FLEXURE STIFFNESS/PREDICTED FLEXURE STIFFNESS VERSUS SPECIMEN-TO-CELL SIZE RATIO

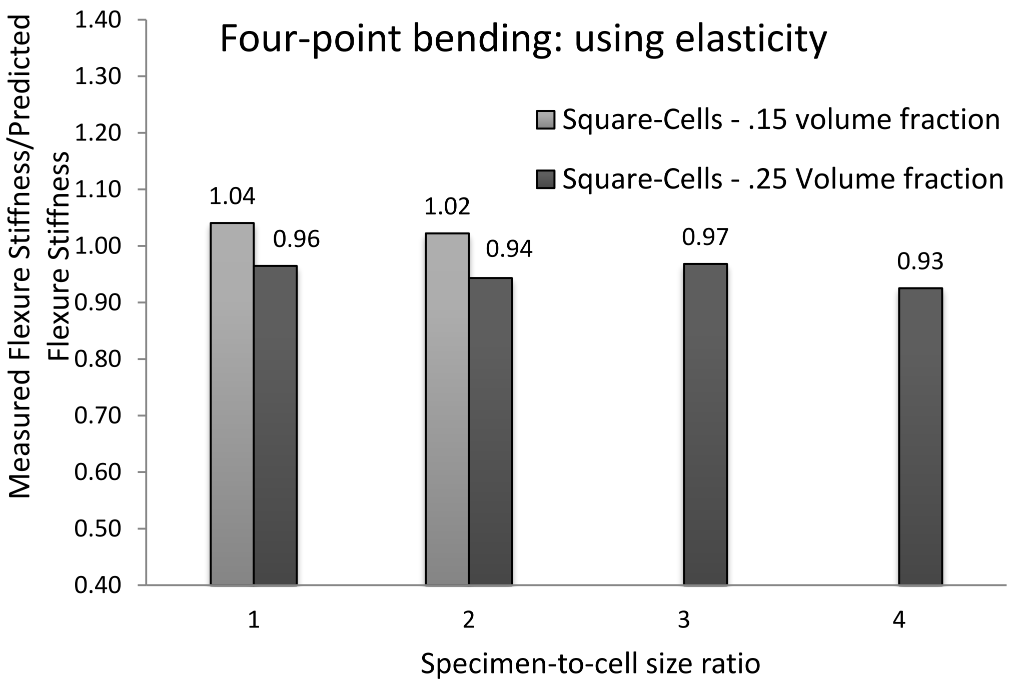

FIGURE 4-5 FOUR-POINT BENDING – EVALUATED USING ELASTICITY THEORY, SQUARED-CELLED SAMPLES, MEASURED FLEXURE STIFFNESS/ PREDICTED FLEXURE STIFFNESS VERSUS SPECIMEN-TO-CELL SIZE RATIO

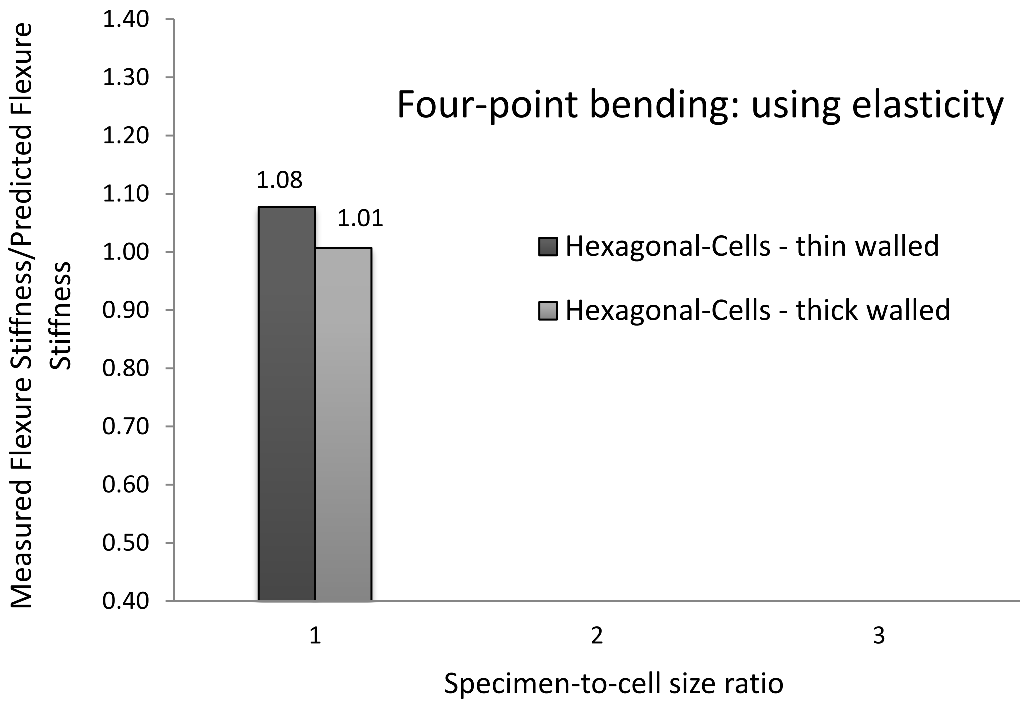

FIGURE 4-6 FOUR-POINT BENDING – EVALUATED USING ELASTICITY THEORY, HEXAGONAL-CELLED SAMPLES, MEASURED FLEXURE STIFFNESS/PREDICTED FLEXURE STIFFNESS VERSUS SPECIMEN-TO-CELL SIZE RATIO

ELASTIC BENDING AND CORRECTIONS FOR LOCALIZED ELASTIC/PLASTIC DEFORMATION

In Figure 4-7 we show the expected geometric relationship in four-point bending of the points U_b and U_a where U_a is measured by the displacement of roller and U_b is measured in the center of the beam using a deflectometer. In this figure the location of the bottom rollers would correspond with point where the upward acting forces labeled $P/2$ are shown. When the beam is in pure elastic bending as shown in Figure 4-7, we expect the displacement of U_b to be greater than for U_a.

Observations of the data showed two general patterns to the data taken during the four-point bending. Figure 4-8 shows representative raw load versus deflection data from testing of the square-celled samples. As shown in Figure 4-8, the data from the center-point measurement, U_b, is reasonably linear for all displacements, while the crosshead displacement data, U_a, is piece-wise linear with a first linear section at one slope and a second section at a significantly different slope. Figure 4-9 shows

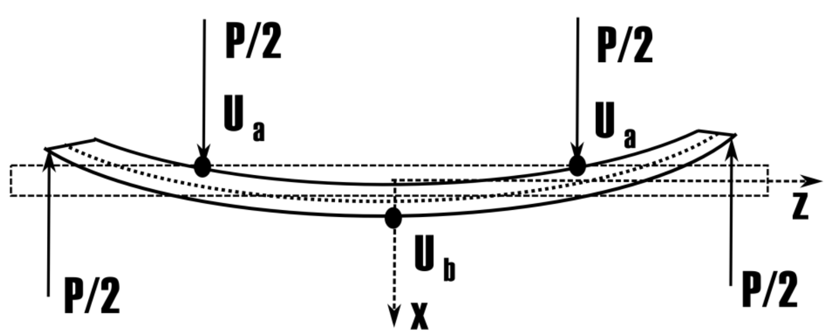

FIGURE 4-7 SCHEMATIC SHOWING THE LOCATION OF THE DISPLACEMENTS USED FOR THE ELASTICITY ANALYSIS

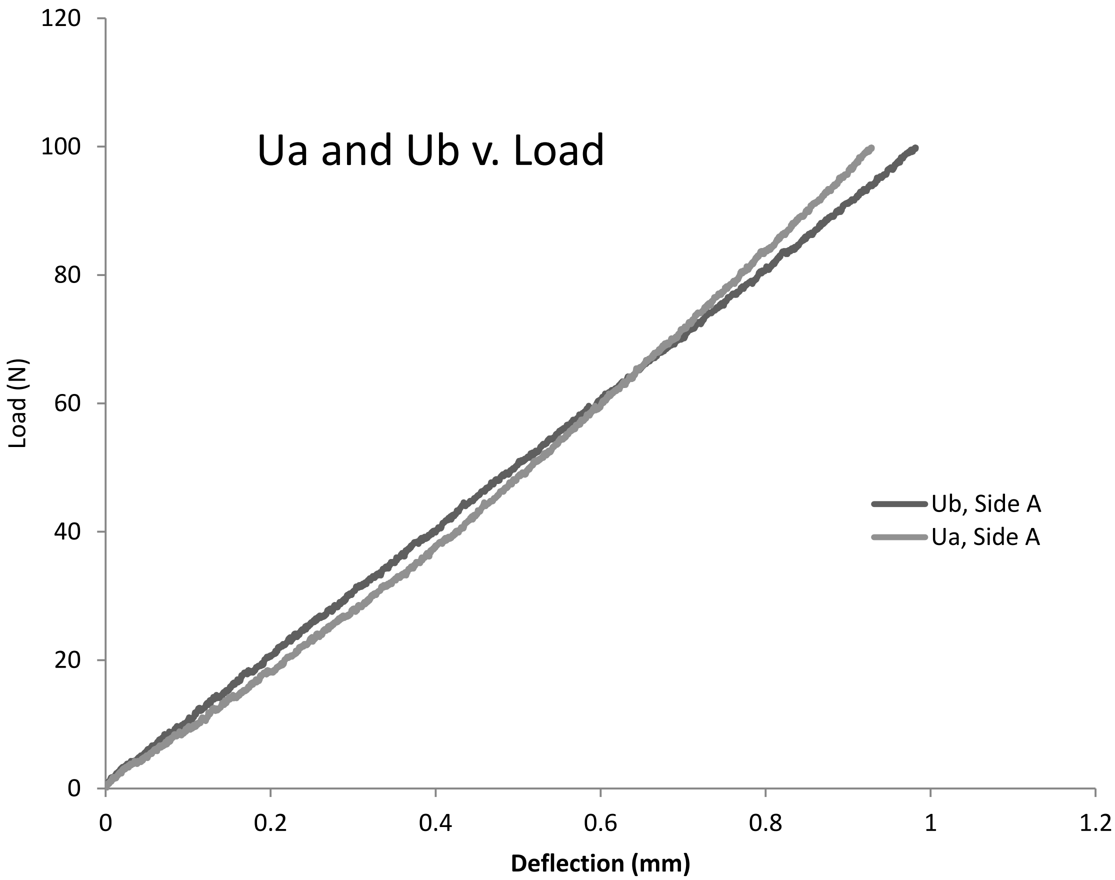

FIGURE 4-8: REPRESENTATIVE DATA FROM FOUR-POINT BENDING TESTS (SQUARE CELLED SAMPLES)

schematically the pattern seen in this data set and how it can be corrected to determine what values to use in the elasticity analysis. The conventional explanation for this behavior is that the roller is “settling-in” during the first section and after some period that “settling-in” is completed. This “settling-in” behavior is not observed in the deflectometer data. To account for this we can obtain a measure of the flexure stiffness, separate from the localized “settling-in,” by shifting the second part of the U_a linear-piece wise data to intersect the origin, as shown in Figure 4-9. Then U_a^* can be used in place of U_a in Equation 3.55 to solve for EI. This was the procedure used to

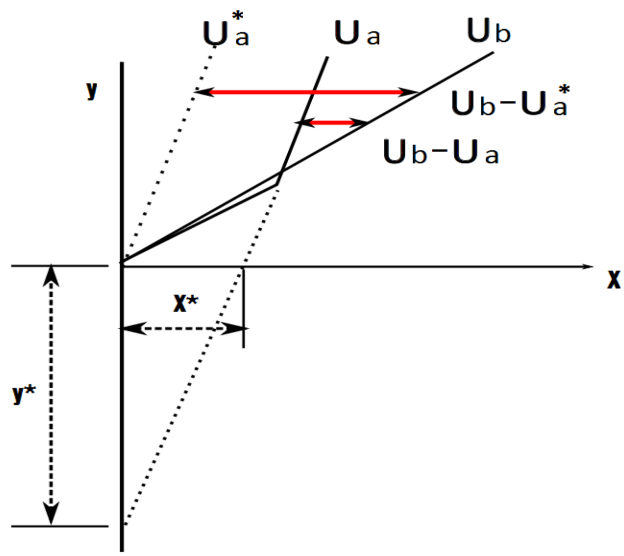

FIGURE 4-9 ONE PATTERN OF DATA SEEN FROM FOUR POINT TESTING

obtain the data shown in Figure 4-5 for all the squared-celled samples. When evaluated in this manner our measured flexure stiffness showed good agreement with the mechanics of solids model predictions.

A check calculation was done to determine if the observed settling behavior was of an expected magnitude. Using a compression model with the area of the total wall thickness used as the area we estimated a deflection of between 0.091 mm and 0.14 mm, for the sample in Figure 4-8, which compares well with experimental measured value of approximately 0.1 mm.

An example of the second observed pattern of the data, collected from the testing in the hexagonal-celled samples, is presented in Figure 4-10. While at first difficult to observe, close examination shows that both the data collected from the center-point deflectometer, U_b, and the cross-head position, U_b, show piece-wise linear behavior. Figure 4-11 shows schematically the piece-wise behavior observed for the hexagonal-celled samples and how the corrections can be implemented to determine the relevant parameters for the elasticity analysis. Since we are measuring U_b at a place where there is no roller contact this cannot be attributed to a "settling-in" phenomena. An additional explanation is the behavior results from a localized elastic/plastic deformation that is propagating from the point of contact of the roller, along the beam. Another possibility is that excessive deformation is elastic buckling from surface imperfections in the structure. Visual inspection of the samples during testing did not show any signs of large scale buckling. However this is not considered sufficient to eliminate elastic buckling since the deformations could be smaller than what would be visually detectable.

Again we can separate the localized deformation from what should be the larger elastic bending response, by shifting the second part of the piece-wise linear curves for both U_a and U_b to intersect the origin as shown in Figure 4-11. We then obtain a U_a^* and a U_b^*, whose difference can be used in Equation 3.55 to calculate flexure stiffness. While the analysis suggested in Figure 4-11 offers some insight in the evaluating the results of the four-point bending of the hexagonal-celled samples, it is important to note that a solution for the flexure stiffness using the elasticity analysis was only obtained for the samples with a specimen-to-cell size ratio of one. For the samples with the higher specimen-to-cell size ratios either one or both of the measured curves, never reached the second stage, were the effects of localized elastic/plastic deformation were no longer dominant. For the hexagonal-celled samples with larger specimen-to-cell size ratios, the deformation is dominated by this localized deformation. This effect is also accentuated by the design choices made when designing the hexagonal-celled samples. When designing the sample set no open cells were allowed. This resulted in samples where the aspect ratio of the sample, increased quicker that the contact area between the roller and the sample

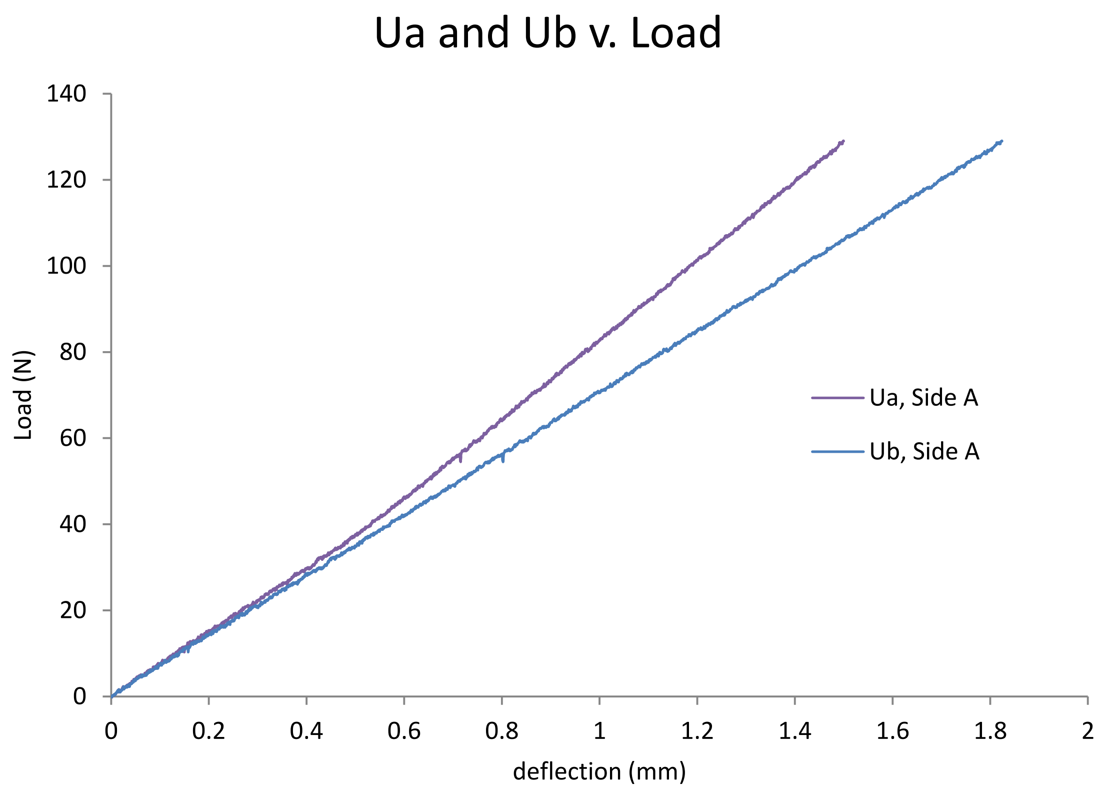

FIGURE 4-10 REPRESENTATIVE DATA FROM FOUR POINT BENDING TESTS (HEXAGONAL-CELLED SAMPLES)

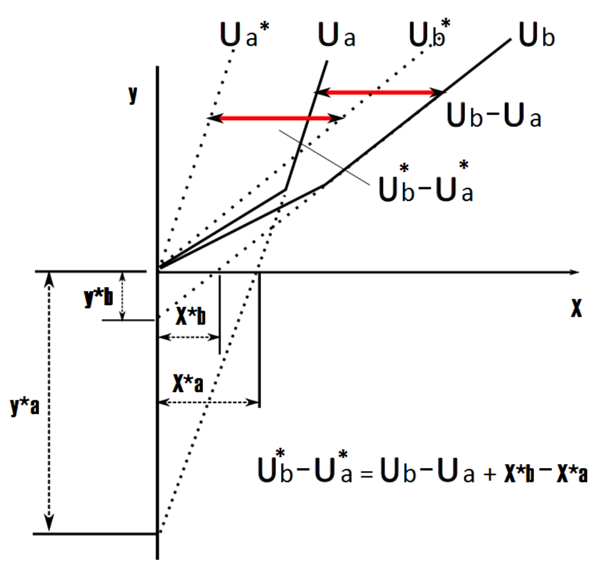

FIGURE 4-11 ONE PATTERN OF DATA SEEN FROM FOUR POINT TESTING

ADDITIONAL DISCUSSION

Recalling that volume fraction is the main parameter used in the continuum model, we saw that varying the volume fraction resulted in similar changes in stiffness in both the model and the samples for both the square-celled and hexagonal-celled samples. In our sample set the thinner walled structures, had the lower volume fraction and were predicted to have a greater variation from the continuum model stiffness than thicker-walled set. We observed this predicted trend in our experiments, along with an additional effect which showed that the lower volume fraction, the greater the effect of localized elastic/plastic deformation.

The length-to-height ratio of the sample is an important geometric parameter utilized in three-point and four-point bending to determine the validity of a given measurement. Slender beam theory gives us a rule of thumb that to ignore shear deformations we need a length-to-height ratio above some value, usually given as between 5-10. Our samples length-to-height ratios ranged between 5.5 and 10.5. For both geometries, we concluded that for three-point testing this range of ratios was too low to yield accurate stiffness for honeycomb structures. For conventional four-point testing we have different results based on cell geometry. Flexure stiffnesses for the square-celled samples were correct while values for the hexagonal-celled samples were not. This is an interesting and somewhat unexpected result and would suggest that a higher length-to-height ratio is needed for hexagonal-celled honeycombs.

Finally some comments regarding the influence of design constraints on the flexure stiffness are warranted. When using a small specimen-to-cell size ratio, one can have an architecture that is either limited to closed-celled elements or alternatively one that allows unconnected elements. These are often referred to as “dangling” or non-load-bearing elements. While this work was limited to using closed-celled elements, limiting the design to closed-celled architecture combined with the geometric considerations also created limits to the way that the resulting hexagonal samples could be loaded. This is one likely component of the difference in increased susceptibility to localized elastic deformation that we observed in the hexagonal-celled samples. From this we conclude that for use in non-sandwich low *R* applications the square-celled honeycomb is easier to implement in practical application because they exhibit fewer constraints on geometry while allowing only closed celled honeycombs.

Chapter 5: Conclusions and future work

Conclusions

Mechanics of solids predicts a positive size-effect relative to continuum model predictions in the flexure stiffness of a honeycombed beam loaded in out-of-plane bending. We present a method of determining the magnitude of that effect for several different methods of constructing or assembling square-celled and hexagonal-celled materials, using both single-walled and doubled-walled construction methods. The predictions are made by deriving a structure-dependent equation for the variation of the second moment of inertia and comparing this to the second moment of inertia to a solid beam with equivalent cross-sectional area. The magnitude of the predicted size-effect is maximum at specimen-to-cell size ratio of 1 and at low volume fractions of solids where it is upto 200% of the continuum value. It drops off quickly as *R*, the specimen-to-cell size ratio, increases, and converges with the continuum model for *R* values greater than about 20. The predicted size effect is of the same order for both square-celled and hexagonal-celled materials and is greater for single-walled construction than for double-walled. For all cases the predicted effect decreases smoothly as the volume fraction of solid increases.

Building test samples using Selective Laser Sintering (SLS) proved to be a successful method of creating honeycomb test samples with variable geometries and specimen-to-cell size ratios, and we conclude that additive manufacturing methods and SLS in particular are well suited for further investigation of the elastic response of honeycombs.

Obtaining meaningful elastic moduli from mechanical testing of honeycombs materials with small specimen-to-cell size and length-to-height ratios is difficult. Our results show that data is easy to obtain but difficult to interpret. The results from standard three-point flexure tests, at the length-to-height ratios tested, (L/h = 5.5 to 10.5) did not agree with predictions for either square or hexagonal-celled samples. Four-point bending gave mixed results; valid results were obtained for the square-celled geometries but not for the hexagonal-celled geometries.

The derivation of a closed form solution using an elasticity model for the response of the four-point bending configuration was a key tool in this work. By recording displacement data at two points it allowed us to separate the elastic bending from the non-bending deformation. We postulated that the source of the non-bending deformation was localized, elastic/plastic deformation that occurs between the loading rollers and the specimen's surface. We believe that the localized deformation is significant in the honeycomb materials we tested.

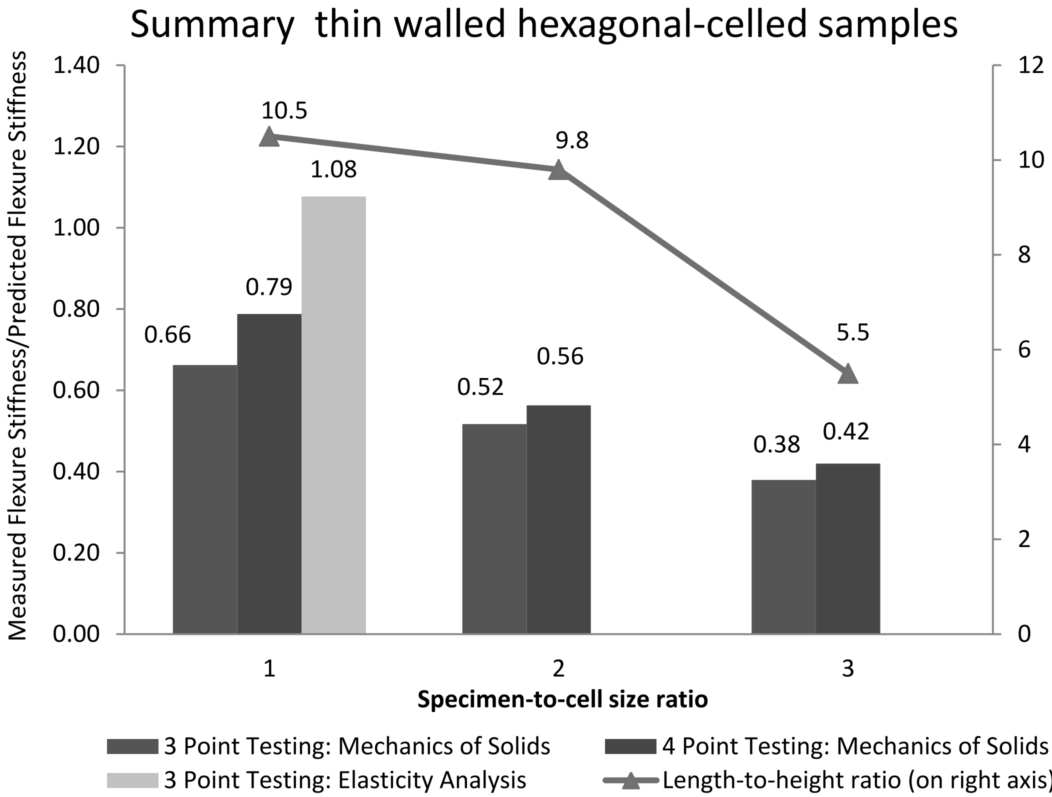

FIGURE 5-1: SUMMARY OF THIN WALLED HEXAGONAL-CELLED SAMPLES

Figures 5-1 to 5-4 summarize our test results. Figure 5-1 is a summary of the results for the thin walled hexagonal-celled samples. The left axis shows the measured flexure stiffness versus the predicted stiffness for the three testing and analysis methods used. On the right axis of the graph we show the length-to-height ratio of the tested samples. Only for the four-point testing, evaluated using elastic analysis, did the measured stiffness match the predicted stiffness. Figure 5-2 is a similar summary for the thick walled hexagonal-celled honeycombs, with the same axis and the same general result showing the four-point elasticity method matching with predicted results. Figures

5-3 and 5-4 show the same data for the square-celled honeycombs. Here we see that both methods of evaluating the four-point test data yielded valid results.

The validity of the test data can be determined from the examination of the sample data. If the load versus crosshead displacement curve is piece-wise linear than, the modulus can likely be determined. Two methodologies were presented for determining flexural stiffness depending on whether or not the deflectometer data is linear or not. If the load versus crosshead displacement is linear, then examination of the deflectometer data can determine whether valid data can be obtained.

Future Work

One area of follow-up work suggested by this project is to better understand the difference in geometry-based response to the localized deformation between the square-celled and the hexagonal-celled honeycombs. This is a difficult problem to approach from a modeling standpoint. One approach would be to construct a 3D finite element model; however preliminary work has highlighted the difficulty in this approach. The required model would need to model both surface contact and bending as three dimensional solids, at very different scales, leading to extremely large models, with the associated difficulties in the development of converging boundary conditions.

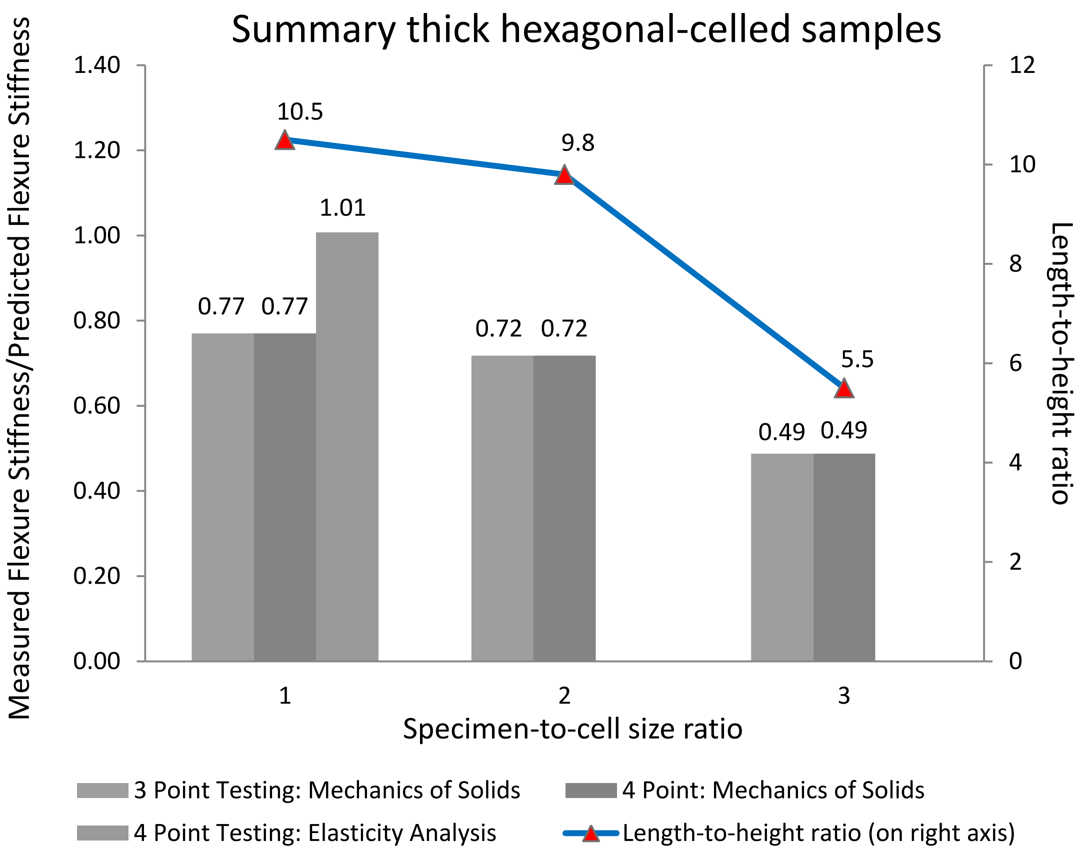

FIGURE 5-2: SUMMARY OF THICK WALLED HEXAGONAL-CELLED SAMPLES

An additional area for follow up work would be to determine experimentally the length-to-height ratio at which three-point bending yields meaningful results for out-of-plane bending stiffness of honeycomb beams. This could require the design and building of a new sample set that can span a greater range of length-to-height ratios and modifications of three-point and four-point testing fixturing.

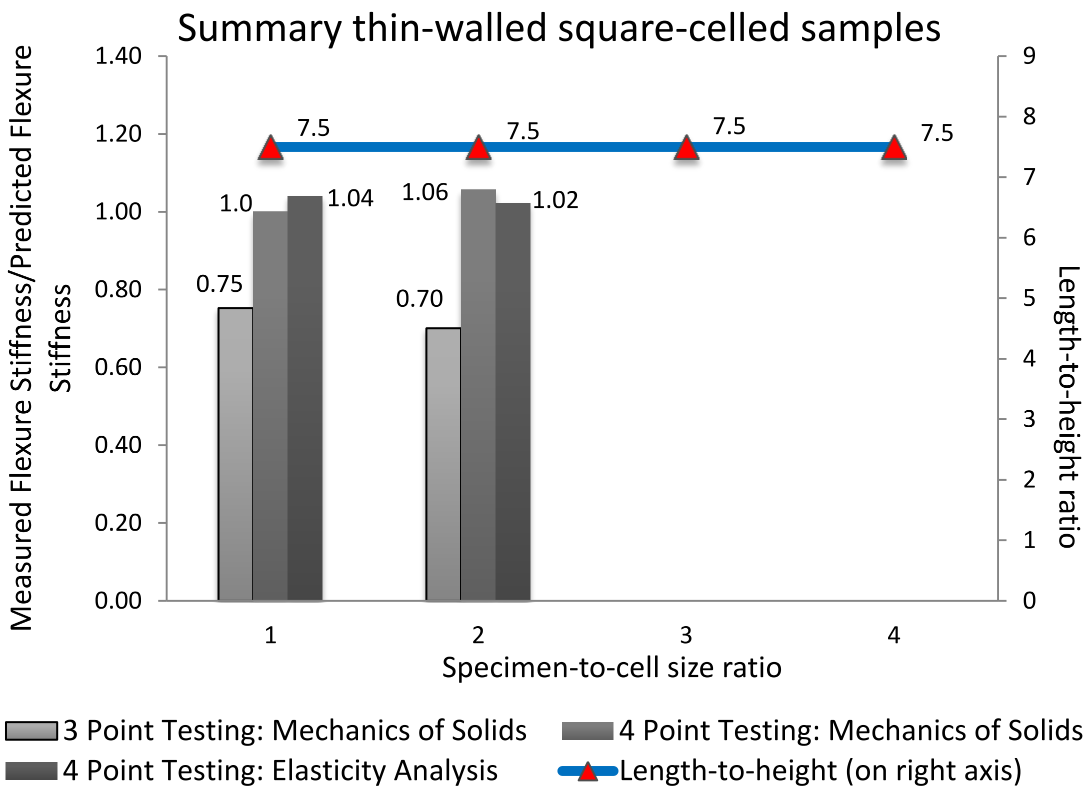

FIGURE 5-3: SUMMARY OF THIN-WALLED SQUARE-CELLED SAMPLES

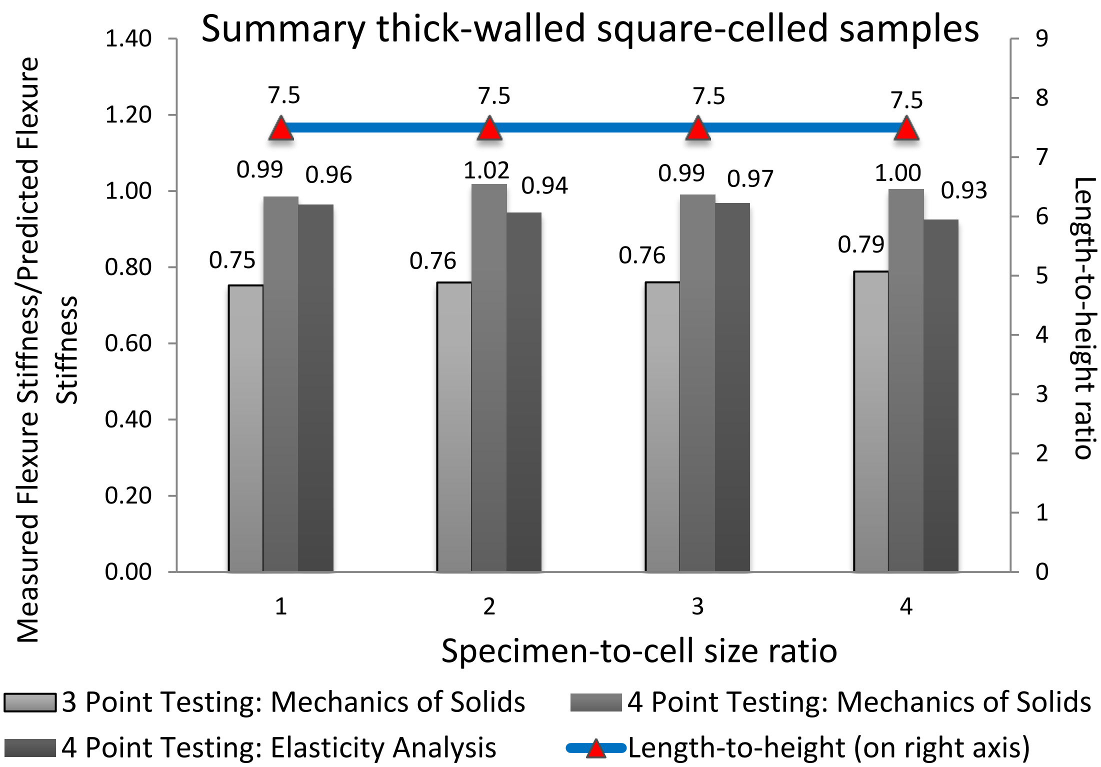

FIGURE5-4: SUMMARY OF THICK WALLED SQUARE-CELLED SAMPLES

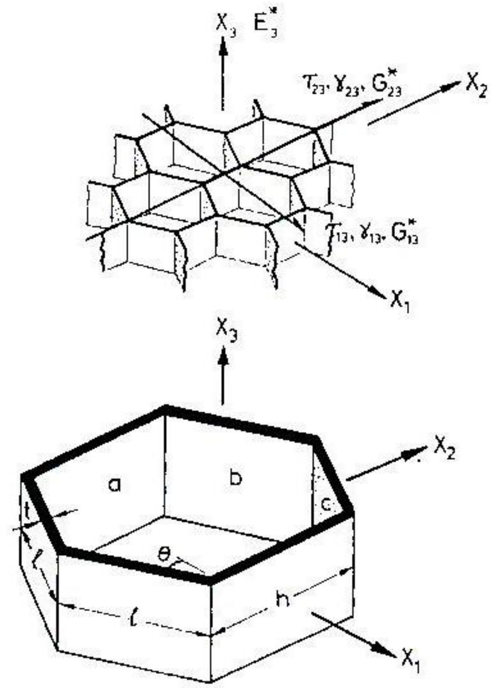

Figure taken from Gibson and Ashby

Appendix A: Elastic Response of Honeycomb Materials

This work is specifically directed at elastic response of honeycomb structures. This can be further examined by separating in-plane and out-of-plane properties. In plane elastic properties are defined by five constants E_1 , E_2, G_{12}, v_{12} and v_{21} where E_1 and v_{12} are respectively the Young's modulus and Poisson's ratio in the direction x_1, while E_2 and v_{21} are the Young's modulus and Poisson's ratio for transverse or x_2 direction. G_{12} is the in plane shear modulus. Continuum treatment for in-plane loading of an irregular honeycomb structure assumes thin walls and that the elastic deformation is the result of pure bending of the honeycomb walls. The following relationships for

E_1 and E_2 as function of the modulus of the solid material are developed by Gibson and Ashby 1988 ,

$$\frac{E_1^*}{E_s} = \left(\frac{t}{l}\right)^3 \frac{\cos\theta}{\left({}^{h}/_{l} + \sin\theta\right)\sin^2\theta}$$

$$\frac{E_2^*}{E_s} = \left(\frac{t}{l}\right)^3 \frac{(h/l + \sin\theta)}{\cos^3\theta}$$

For regular honeycombs with uniform thickness *h=l* and *ϑ*=30 these relationships reduce to the same expression

$$\frac{E_1^*}{E_s} = \frac{E_2^*}{E_s} = \frac{4}{\sqrt{3}}\left(\frac{t}{l}\right)^3$$

Several comments must made about these results, first is regarding the thin wall assumption, by assuming thin walls shear and axial deformation has been ignored. An additional term is proposed by Gibson and Ashby to account for this, giving

$$\frac{E_1^*}{E_s} = \left(\frac{t}{l}\right)^3 \frac{\cos\theta}{\left({}^{h}/_{l} + \sin\theta\right)\sin^2\theta} \frac{1}{1 + \ (2.4 + 1.5v_s + \cot^2\theta)(t/l)^2}$$

and

$$\frac{E_2^*}{E_s} = \left(\frac{t}{l}\right)^3 \frac{(h/l + \sin\theta)}{\cos^3\theta} \frac{1}{1 + \ \left(2.4 + 1.5v_s + \tan^2\theta + \frac{2(h/l)}{\cos^2\theta}\right)(t/l)^2}$$

For completeness we present similarly developed expressions for , G_{12}, v_{12} and v_{21}

$$\frac{G_{12}{}^{*}}{E_s} = \left(\frac{t}{l}\right)^3 \frac{(h/l + \sin\theta)}{(h/l)^2(2h/l + 1)\cos\theta}$$

$$v_{12} = \frac{\cos^2\theta}{(h/l + \sin\theta)\sin\theta}$$

$$v_{21} = \frac{(h/l + \sin\theta)\sin\theta}{\cos^2\theta}$$

And with the regular hexagonal structure these reduce to

$$\frac{G_{12}{}^{*}}{E_s} = \frac{1}{\sqrt{3}}\left(\frac{t}{l}\right)^3$$

$$v_{12} = v_{12} = 1$$

We now turn our attention to out-of-plane elastic response , which is the primary focus of this work. Five additional moduli are needed to describe the out-of-plane deformation response of honeycombs. These include two shear moduli G_{13} , and $G_{\ 23}$, two Poisson's ratios v_{31} and v_{32}, and an additional Young's modulus E_3 . Again drawing on the classical continuum mechanics theory as we see that the

$$v_{31}^{*} = v_{32}^{*} = v_s$$

The shear moduli are significantly more complicated and while presented below are not significantly addressed in this work.

$$\frac{G_{13}^{*}}{G_s} \geq \frac{cos\,\theta}{(h/l + sin\,\theta)}\left(\frac{t}{l}\right)$$

$$\frac{G_{23}^*}{G_s} \geq \frac{h/l + \sin\theta}{(1 + 2h/l)\cos\theta}\left(\frac{t}{l}\right)$$

Finally we turn our attention to the continuum construction of the out-of-plane Young's modulus E_3.

$$\frac{E_3^*}{E_s} = \left\{\frac{h/l + 1}{2(h/l + \sin\theta)\cos\theta}\right\}\frac{t}{l} = \frac{\rho^*}{\rho_s}$$

This is modulus will be focus of much of the work that follows and is used for both out-of-plane bending and out-of-plane compression and tension.

Summarizing the elastic response of a regular honeycomb we find the following compliance matrix

$$\begin{pmatrix} \varepsilon_1 \\ \varepsilon_2 \\ \varepsilon_3 \\ \gamma_1 \\ \gamma_2 \\ \gamma_3 \end{pmatrix} = \varepsilon_i = S_{ij}\sigma_j = \begin{bmatrix} \frac{1}{E_1} & -\frac{\text{v}_{12}}{E_1} & -\frac{\text{v}_{31}}{E_3} & 0 & 0 & 0 \\ -\frac{\text{v}_{12}}{E_1} & \frac{1}{E_1} & -\frac{\text{v}_{31}}{E_3} & 0 & 0 & 0 \\ -\frac{\text{v}_{13}}{E_1} & -\frac{\text{v}_{13}}{E_1} & \frac{1}{E_3} & 0 & 0 & 0 \\ 0 & 0 & 0 & \frac{1}{G_{31}} & 0 & 0 \\ 0 & 0 & 0 & 0 & \frac{1}{G_{31}} & 0 \\ 0 & 0 & 0 & 0 & 0 & \frac{1}{G_{12}} \end{bmatrix} \begin{pmatrix} \sigma_1 \\ \sigma_2 \\ \sigma_3 \\ \sigma_{23} \\ \sigma_{31} \\ \sigma_{12} \end{pmatrix}$$

Where

$$\text{v}_{ij} = -\varepsilon_j/\varepsilon_i$$

And in-plane isotropy means that

$$G_{12} = \frac{E_1}{2(1 + \text{v}_{12})}$$

And from the matrix

$$\frac{\text{v}_{31}}{E_3} = \frac{\text{v}_{13}}{E_1}$$

Reducing the number of independent elastic constants for regular honeycomb to five E_1, v_{12}, E_3, v_{31} and G_{13}

Appendix B: DuraForm PA Plastic; 3DSystem; Technical Data Sheet

SINTERING

DuraForm® PA Plastic

For use with all selective laser sintering (SLS®) systems

Technical Data

General Properties

Measurement	Condition	Metric	U.S.
Specific Gravity	ASTM D792	1.00 g/cm³	1.00 g/cm³
Moisture Absorption - 24 hours	ASTM D570	0.07%	0.07%

Mechanical Properties

Measurement	Condition	Metric	U.S.
Tensile Strength, Yield	ASTM D638	N/A*	N/A*
Tensile Strength, Ultimate	ASTM D638	43 MPa	6237 psi
Tensile Modulus	ASTM D638	1586 MPa	230 ksi
Elongation at Yield	ASTM D638	N/A*	N/A*
Elongation at Break	ASTM D638	14%	14%
Flexural Strength, Yield	ASTM D790	N/A*	N/A*
Flexural Strength, Ultimate	ASTM D790	48 MPa	6962 psi
Flexural Modulus	ASTM D790	1387 MPa	201 ksi
Hardness, Shore D	ASTM D2240	73	73
Impact Strength (notched Izod, 23°C)	ASTM D256	32 J/m	0.6 ft-lb/in
Impact Strength (unnotched Izod, 23°C)	ASTM D256	336 J/m	6.3 ft-lb/in
Gardner Impact	ASTM D5420	2.7 J	2.0 ft-lb

Thermal Properties

Measurement	Condition	Metric	U.S.
Heat Deflection Temperature (HDT)	ASTM D648 @0.45 MPa @1.82 MPa	 180 °C 95 °C	 356 °F 203 °F
Coefficient of Thermal Expansion	ASTM E831 @0 - 50 °C @85 - 145 °C	 82.6 µm/m-°C 179.2 µm/m-°C	 45.9 µin/in-°F 99.6 µin/in-°F
Specific Heat Capacity	ASTM E1269	1.64 J/g-°C	0.392 BTU/lb-°F
Thermal Conductivity	ASTM E1225	0.70 W/m-K	4.86 BTU-in/hr-ft²-°F
Flammability	UL 94	HB	HB

Electrical Properties

Measurement	Condition	Metric	U.S.
Volume Resistivity	ASTM D257	5.9×10^{13} ohm-cm	5.9×10^{13} ohm-cm
Surface Resistivity	ASTM D257	7.0×10^{13} ohm	7.0×10^{13} ohm
Dissipation Factor, 1 KHz	ASTM D150	0.044	0.044
Dielectric Constant, 1 KHz	ASTM D150	2.73	2.73
Dielectric Strength	ASTM D149	17.3 kV/mm	439 kV/in

*N/A = Data not applicable for this test condition

Data was generated by building parts under typical default parameters. DuraForm PA Plastic was processed on a base-level HiQ™ SLS System at 13 watts laser power, 5 m/sec [200 inches/sec] scan speed, and a powder layer thickness of 0.1 mm [0.004 inches].

3D Systems Corporation
333 Three D Systems Circle
Rock Hill, SC 29730 U.S.A.

Tel: +1 803.326.4080
Toll-free: 800.889.2964
Fax: +1 803.324.8810

moreinfo@3dsystems.com
www.3dsystems.com
NASDAQ: TDSC

PN 70715 Issue Date - April 10

Appendix C: PA250, Advanced Laser Materials, LLC: Technical Data Sheet

PA 250

Highly Recyclable Nylon 12 Laser Sintering Material

Technical Data Sheet

POWDER PROPERTIES	TEST METHOD	ALM PA 250
Bulk Density	ASTM D1895	0.50 grams/CC
Average Particle Size (D50)	Laser Diffraction	40 microns
Particle Size Range (D10-D90)	Laser Diffraction	30 to 50 microns
Sintered Part Density	ASTM D792	1.01 grams/CC
THERMAL PROPERTIES	**TEST METHOD**	**ALM PA 250**
Melting Point	ASTM D3418	181 Deg C
Melt Flow Rate (3min, 5.0kg, 235C)	ASTM D1238	40 grams/10min
MECHANICAL PROPERTIES	**TEST METHOD**	**ALM PA 250**
Heat Deflection Temp @ 0.45 MPa	ASTM D648	179 Deg C
Heat Deflection Temp @ 1.82 MPa	ASTM D648	86 Deg C
Ultimate Tensile Strength (XY)	ASTM D638	46 MPa / 6,700 psi
Ultimate Tensile Strength (Z)	ASTM D638	36 MPa / 5,200 psi
Tensile Modulus (XY)	ASTM D638	1,740 MPa / 490 kpsi
Tensile Modulus (Z)	ASTM D638	2,137 MPa / 256 psi
Elongation at Break (XY)	ASTM D638	16%
Elongation at Break (Z)	ASTM D638	4%
Surface Finish	ISO 4287	9 microns
Volume Resistivity	ASTM D257	3.1 x 10^14 ohm-cm

Actual part properties may vary slightly from those listed above based on processing parameters, operating conditions, and material usage. The above properties were based on virgin ALM PA 250 using nominal operating parameters on a 2500+ platform. Advanced Laser Materials, LLC makes no warranties of materials for any particular application, nor does it make a warranty of any type, expressed or implied, including, but not limited to, the warranties of merchantability for a particular purpose.

alm

Advanced Laser Materials, LLC • Tel: 254-773-3080 • Fax: 254-773-3084
3115 Lucius McCelvey, Temple, TX 76504 • www.alm-llc.com

ALM PA 250 Data Sheet: 09.28.2011

Bibliography

Anderson, W. B., and R.S. Lakes. "Size effects due to Cosserat elasticity and surface damage in closed-cell polymethacrylimide foam." *Journal of Materials Science*, 1994: 6413-6419.

Andrews, E.W., and L.J. Gibson. "The influence of cracks, notches and holes on thetensile strength of cellular solids." *Acta Materialia* 49 (2001): 2975-2979.

Andrews, E.W., G. Gioux, P. Onck, and L.J. Gibson. "Size effects in ductile cellular solids. Part II: experimental results." *International Journal of Mechanical Sciences*, 2001: 701-713.

Banhart, J. "Manufacture characterisation and application of cellular metal and metal foams." *Progress in Material Science* 46, no. 6 (2001): 559-632.

Beaman, Joseph. *Solid FreeForm Fabrication.* Austin: Kluwer, 1997.

Bianchi, G., G.S. Aglietti, and G. Richardson. "Development of efficient and cost-effective spacecraft structures based on honeycomb panel assemblies." *Areospace Conference, 2010 IEEE*, March 2010: 1-10.

Brezny, R, and D.J. Green. "Charaterization of edge effects in cellular material." *Journal of Material Science*, 1990: 4571-4578.

Crumm, Aaron T., and John W. Halloran. "Fabrication of Microconfigured Mutilcomponent Ceramic." *Journal of the American Ceamic Society* 81, no. 4 (1998): 1053-57.

Crump. Appartus and method for creating three-dimensional objects. USA Patent 5121329. October 30, 1989.

D6272, ASTM. "Standard test method for flexural propertied of unreinforced and reinforced plastics and electrical insulating materials by four point bending." n.d.

D790, ASTM. "Standard test method for fleusral properties of unreinforced and reinforced plastics and electrical insulating material." n.d.

Dai, Gaoming, and Weihpng Zhang. "Cell size effect analysis of the effective Young's modulus of sandwich core." (Computational Materials Science) 2009, no. 46 (2009): 744-748.

Deckard. Method and apparatus for producing parts by selective sintering. US Patent 4863538. October 17, 1986.

EconHP Holding GmbH. *History of sandwich construction and honeycombs.* October 1, 2011. www.econhp.de/history.htm (accessed October 1, 2011).

Fleck, N. A., and J. W. Hutchinson. "A phenomenological theory for strain gradient effects in plasticity." *Journal of Mechanics and Physics of Solids* 41 (1993): 1825-1857.

Fleck, N.A, and J.W. Hutchinson. *Strain gradient plalsticity.* Vol. 33, in *Advances in Applied Mechanics*, by A. Aref and E. van der Glessen, 295-361. Cambridge, England: Academic Press, 1997.

Fleck, N.A., G.M. Muller, M.F. Ashby, and J.W Hutchinson. "Strain gradient plasticity: Theory and experiment." *Acta Metallurgica et Materialia* 42, no. 2 (1994): 475-487.

Gibson, Lorna J., and Michael F. Ashby. *Cellular solids: Structures and Properties.* Cambridge: Cambidge University Press, 1997.

Gruppi, Gianpiero, and Enrico Tronconi. "Honeycomb supports with high thermal conductivity for gas/solid chemical processes." *Catalysis Today* 105 (2005): 297-304.

Idiart, M.I., V.S. Deshpande, N.A. Fleck, and J.R. Willis. "Size effects in the bending of thin foils." *International Journal of Engineering Science*, no. 47 (2009): 1251-1264.

Labuhn, D. *Assessment of Potential use of Cellular Materials for Space Applications.* European Space Agency, 2005.

Lakes, Roderic S. "Size effect and micromechanics of a porous solid." *Journal of Materials Science* 18 (1983): 2572-2580.

Marcus, Harris L., and David L. Bourell. "Solid freeform fabrication finds new applications." *Advanced Materials & Processes* 144, no. 9 (1993): 28-35.

Mora, Rafael, and Anthony Waas. "Mesurement of the Cosserat constant of circular-cell polycarbonate honeycomb." *Philosophical Magazine A* (Taylor and Francis Ltd.) 80, no. 7 (2000): 1699-1713.

Onck, Patrick, E.W. Andrews, and L.J. Gibson. "Size effects in ductile cellular solids. Part I: Modeling." *International Journal of Mechanical Sciences*, 2001: 681-699.

Rosochowski, A., Matuszak, A. "Rapid tooling: the state of the art." *Journal of Materials Processing Technology*, 2000: 191-198.

Simancik, F. "Introduction: The strange world of cellular metals." In *Handbook of Cellular Metals: Production, Processing, Applications*, edited by H.P. Degischer and B. Kriszt. Wiley-VCH Verlag GmbH & Co. KGaA, 2002.

Tekoglu, Cihan, and Patrick Onck. "Size effects in the mechanical behavior of cellular materials." *Journal of Material Science*, 2005: 5911-5917.

Tekoglu, Cihan, and Patrick Onck. "Size effects in two-dimensional Voronoi foams: A comparison between generalized continua and discrete models." (Journal of the Mechanics and Physics of Solids) 56 (2008): 3541-3564.

Van Hoy, Charles, Andrew Barda, Michelle Griffith, and John W. Halloran. "Microfabrication of Ceramics by Co-extrusion." *The Journal of the American Ceramics Society* 81, no. 1 (1998): 152-58.

Wadley, H., Fleck N.A., Evans, A. "Fabrication and structural performance of periodic cellular metal sandwich structures." *Composites Science and Technology*, 2003: 2331-2343.

Zhu, H.X. "Size-dependent elastic properties of micro- and nao-honeycombs." *Journal of the Mechanics and Physics of Solids*, 2010: 696-709.